Some mathematical models arising in nano- and bio-technology

Yue Chan
University of Wollongong

Some mathematical models arising in nano- and bio-technology

A thesis submitted in (partial) fulfillment of the
requirements for the award of the degree

Doctor of Philosophy

from

UNIVERSITY OF WOLLONGONG

by

Yue Chan

Master of Mathematics
University of Wollongong

Bachelor of Science
University of Melbourne

Nanomechanics Group
School of Mathematics and Applied Statistics

2009

I, Yue Chan, declare that this thesis, submitted in fulfillment of the requirements for the award of Doctor of Philosophy, in the School of Mathematics and Applied Statistics, University of Wollongong. This thesis is wholly my own work unless otherwise referenced or acknowledged below. The document has not been submitted for qualifications at any other University or Institution.

Yue Chan

Oct, 2009

Acknowledgements

I gratefully acknowledge the people who provided enormous assistance in preparing of this thesis. First of all, I would like to express my deep gratitude to my supervisors, Dr Ngamta Thamwattana and Professor Jim Hill, without their advice and assistance, this thesis would have never been completed. I would also like to thank my previous supervisor Dr Grant Cox as well as all the current and the former members at the Nanomechanics Group. Last but not least, I must thank my mom for her support and encouragement; without her, it would have been impossible for me to come to study in Australia. This thesis is dedicated to all of these people.

Abstract

In this thesis, three mechanical models arising from nanoscale and biological systems are investigated, namely the dynamics of various nanostructures, the axial buckling of carbon nanotubes and nanopeapods, and the worm-like chain model for stretched semi-flexible molecules and the utilization of such a model for investigating molecular stretching in the connective tissue extracellular matrix.

In nanomechanics, we investigate the motion of both a carbon atom inside a carbon nanotube and a C_{60} fullerene inside a carbon nanotube. We assume a continuous model for which the atoms are assumed to be smeared across the surface of the molecule, so that the pairwise molecular energy can be approximated by performing surface integrals. The spiral path of the atom is found to be stable, but the spiral path of the C_{60} fullerene is shown to only exist for a few pico seconds. Next, we investigate the motion of a nano tippe top spinning on the interior of a single-walled carbon nanotube in the presence of a variable magnetic field. Unlike the classical tippe top, the nanoscale tippe top does not flip over since the gravitational effect is insignificant at the nanoscale. After the precession, if we apply an opposite retarding magnetic force at the contact point, then the molecule will return to its original standing up position. We next investigate some nanoscale orbiting systems, and in particular, we study an atom and a C_{60} fullerene orbiting around a single infinitely long carbon nanotube and a C_{60} fullerene orbiting around a C_{1500} fullerene. We find that the circular orbiting frequencies of the proposed nano systems are in the gigahertz range and the classification of their orbiting paths are determined numerically.

For the axial buckling of carbon nanotubes and nanopeapods, we investigate the buckling behavior of doubly clamped multi-walled carbon nanotubes and nanopeapods as nano-electromechanical systems. We incorporate the bending curvature of the tube into the elastic energy and determine the nanotube's maximum displacement for all bending regimes. We find that while the approximate solution (without curvature) underestimates the maximum displacement of the buckled carbon nanotube in the weak bending regime, our numerical solution provides an entirely different prediction in comparison to the approximate solution in the strong bending regime. Furthermore, we derive an instability condition for multi-walled carbon nanotubes and nanopeapods under an axial load by taking into account the van der Waals forces between molecules. We observe that the critical force derived from the axial buckling stability criterion decreases as a result of the molecular interactions between adjacent layers of the nanotubes and the molecular interactions between the embedded fullerenes and the inner carbon nanotube.

The worm-like chain model arises as a model for stretched semi-flexible molecules and for its applications to molecular stretching in the extracellular matrix, we adopt a variational principle to examine the model and then we utilize the model to describe anionic glycosaminoglycan between collagens. The worm-like chain model has been proposed assuming that each monomer resists the bending force. We determine a force-extension formula for the worm-like chain model analytically, and find that our formula suggests new terms such as the free energy and the cut-off force for a molecule. In addition, we predict two possible phase changes for a stretched molecule, and show theoretically that a molecule must undergo two phase changes when they are stretched beyond their total contour lengths. Furthermore, we adopt the worm-like chain model to describe the mechanical properties of a collagen pair in the connective tissue extracellular matrix. We find that the growth of fibrils is intimately related to the maximum length of the anionic glycosaminoglycan and the relative displacement of two adjacent fibrils.

Contents

List of Figures

List of Tables

Chapter 1

Introduction

In this introduction, we firstly discuss the nature of mathematical modeling, followed by a general overview of carbon nanotubes and fullerenes and an introduction into the technological applications of both molecules. We then turn our attention to biotechnology and discuss the importance of structural polymers in maintaining the shape modulus of animal tissues. Finally, an outline of the thesis structure is provided.

1.0.1 Mathematical modeling

Most mathematical modeling builds on universal physical laws, such as the conservation of mass, momentum and energy, and hence reflects the beauty and order of nature by means of formulae and numbers. Applied mathematical modeling describes real-world problems constrained by particular assumptions. It may be applied to a vast number of physical systems, over widely different length scales from the analysis of galactic structures to life-sized structures such as water waves, and down to the micro and submicroscopic scales for molecular structures. The merit of mathematical modeling is that one may derive reasonable predictions subject to prescribed assumptions, and often such predictions may reduce the production costs by avoiding implementing some expensive experimental investigations. Mathematical modeling may be roughly divided into the following three steps:

1. Quantification of the scientific or the technological problem,

2. Formulation as a mathematical model,

3. Solving the established mathematical equations,

4. Empirical verification of the numerical solutions.

We note that all these steps are equally important in advancing our knowledge. The third step, which may involve numerous methodologies such as Fourier analysis, perturbation theory, asymptotic expansions, potential theory, numerical methods, molecular dynamics simulation, probabilistic theory etc, may often require knowledge from a skilled mathematician.

Nanotechnology is the study of technology at the nanoscale, which is a newly emerging field intertwining all the traditional sciences of physics, chemistry, biology, engineering and mathematics. Biotechnology involves applications that utilize biological systems, living organisms, or derivatives thereof, to make or modify products or processes for specific usage; and investigates the sustainability and analysis of biological systems. Mathematical modeling is a powerful tool which allows us to quantify certain scientific phenomenon and then carry out a deductive reasoning to gain new insights. It acts as a predictive tool which may indicate optimal research outcomes and directions in rapidly developing areas. The motivation for the models developed in this thesis is provided by the three specific areas for both the nano and biotechnologies:

1. Mechanics of fullerenes and carbon nanotubes nano structures,

2. Axial buckling of carbon nanotubes and nanopeapods and applications,

3. The worm-like chain model for stretched semi-flexible molecules and the mathematical modeling of molecular stretching in the extracellular matrix.

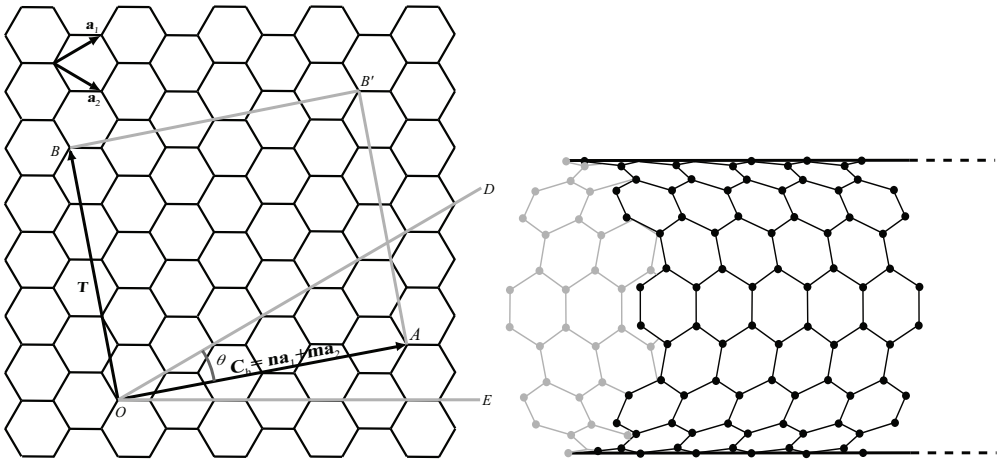

Figure 1.1: Chirality in graphene sheet. Each pair of integers (n, m) represents a possible nanotube structure. Thus, the chirality can be expressed as $\mathbf{C} = n\mathbf{a_1} + m\mathbf{a_2}$, where $\mathbf{a_1}$ and $\mathbf{a_2}$ are the unit cell base vectors. While $m = 0$ represents for all zig-zag tubes, $n = m$ represents for all armchair tubes. All the other combinations of n and m are chiral type (left) and carbon nanotube (right).

1.0.2 Carbon nanotubes

The scientific realization of carbon nanotubes (CNTs) was first initiated by Iijima [66], who published a paper with the title "Helical microtubules of graphitic carbon" in the journal Nature. Carbon nanotubes (see Fig. 1.1 for details) are allotropes of carbon atoms having novel and superior physical properties [100] such as very high mechanical strength [131, 133], low weight, and the ability to be either metallic or semi-conducting depending on their geometric configurations [111, 174]. Their unique chemical properties [108] also make them potentially useful in many nanotechnology and material science applications.

The chemical bonding of a pure carbon nanotube is composed entirely of sp^2 bonds, as predicted by quantum mechanics. This bonding structure is equivalent to a graphene sheet, a single layer of graphite, and provides carbon nanotubes with their superior mechanical strength since the sp^2 bonds are even stronger than the sp^3 bonds found in diamond. Mechanically, carbon nanotubes possess the largest known axial Young's modulus, which arises due to the strong sp^2 bonding between carbon atoms. Under high pressure carbon nanotubes can merge together by exchanging some sp^2 bonds for sp^3 bonds, giving rise to the possibility of producing strong

one-dimensional cables through high-pressure nanotube linking, and they can be elastically reversible after large twisting, kinking and bending deformations.

Owing to the non-polar nature of their molecular bonds, carbon nanotubes are insoluble and therefore very stable in water. However, they can be covalently fuctionalized, i.e. they respond very well to some strong acids and chemical oxidizers to carry out some particular tasks. Since they have a very large surface area to volume ratio, they provide ideal candidates for gas filtration, sensing and energy storage. Furthermore, their electrical properties differ depending on the chirality (n,m) of the nanotube (see Fig. 1.1 for details). As mentioned in [100], one third of carbon nanotubes are metallic and the rest are semi-conductors.

1.0.3 Fullerenes

Jones [71] suggested in the New Scientist, under the name of Daedalus, the possibility of a cage-like hollow all-carbon molecules. However, it was not until two decades later, that Kroto [84] experimentally discovered C_{60} and C_{70} fullerenes by mass spectrometry (an illustration for C_{60} is shown in Fig. 1.2). The C_{60} molecule possesses I_h symmetry, and has a spherical shape. Euler's theorem for regular polyhedra states that $F + V = E + 2$, where F, V and E denote the numbers of faces, vertices and edges respectively [100]. After some simple manipulation of this equation, one can show that the smallest possible fullerene is C_{20}. However, the formation of the C_{20} molecule is not energetically favorable owing to the high curvature of the carbon bonding between atoms of the C_{20} fullerene, and also the isolated pentagon rule, which states that two adjacent pentagons will not be energetically favorable [83, 136]. By considering both Euler's theorem and the isolated pentagon rule, we may conclude that C_{60} is the smallest possible stable fullerene. As discussed by Goldberg [48], Yoshida and Osawa [176] and Dresselhaus et al. [37], an icosahedral fullerene consists of twenty equilateral triangles, each specified by a pair of integers (n, m) such that the total number of carbon atoms N in the fullerenes C_N is given by

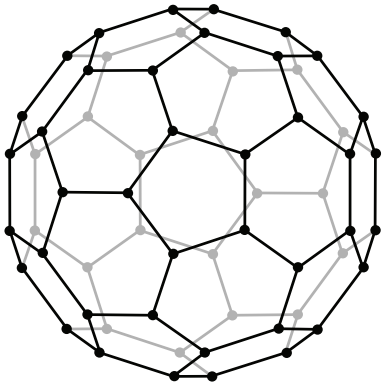

Figure 1.2: C_{60} fullerene.

$$N = 20(n^2 + nm + m^2), \tag{1.1}$$

and the diameter of the icosahedron is given by the expression

$$D = \frac{5\sqrt{3}d_{cc}}{\pi}(n^2 + nm + m^2)^{1/2}, \tag{1.2}$$

where d_{cc} is the bond length between two carbon atoms. In general, a fullerene C_N belongs to either I- or I_h-symmetry. In particular, I_h-symmetry can be divided into two main types, namely type 1 when $n = m$ and type 2 when $n = 0$ or $m = 0$, which have an ellipsoidal shape. C_{60} has $(n, m) = (1, 1)$, and belongs to type 1 I_h-symmetry. The first five fullerenes of type 1 I_h-symmetry are C_{60}, C_{240}, C_{540}, C_{960} and C_{1500}.

1.0.4 Nano-electromechanical systems

Carbon nanotubes are ideal candidates for nano-electromechanical systems, and have opened up a vast area of potential novel applications [24]. For example, carbon nanotubes have been implemented as nanotube-based pressure and mass sensors [150, 107], nanotweezers [76, 1], switches in random access memory devices [129], and actuators [10]. Moreover, recent research reveals that carbon nanotubes can also be utilized as nano-electromechanical switches [34, 78, 23], resonating charge shuttles [39], single electron spin detectors [130] and gigahertz oscillators [179, 90, 27, 28]. The main advantages for such nano devices over their micro counterparts are that

they are not only ultra fast and highly sensitive but they have a very low power consumption [138, 60]. System biology explores the basic structures of living organisms by modeling the inter and intra cellular processes [79], and may utilize nano sensors to provide data for quantitative modeling verification. Nano-electromechanical systems can also be utilized in the detection of quantum mechanical states of motion [138, 104].

Further electronic system miniaturization will create a high demand for the down-scaling of sensor functions [61]. The small diameter of the nanotube enables probes to measure an area of approximately to 1 nm $\times$ 1 nm, for which a deflection can be measured, and which cannot be reached by most conventional methods [60, 166]. Recent research has been undertaken on the doubly clamped nanotube as a nano-electromechanical system. Stampfer et al. [151] investigate a nano-electromechanical sensing device, which is based on a suspended single-walled carbon nanotube to measure small deflections at the nanoscale. These authors discuss both the fabrication process and the measurement methodology of such nano devices, and the corresponding piezoresisitive gauge factors can attain up to 2900, which is much greater than the values for existing conventional strain gauges. Charge-induced buckling in a single-walled carbon nanotube has also been experimentally manipulated. Furthermore, Sazonova et al. [135] report on the guitar-string-like oscillation models of doubly clamped nanotube oscillators, and show experimentally that the resonance frequency of such systems can be tuned and therefore can be utilized to transduce very small forces. Theoretical studies on the suspended nanotube oscillators are also widely investigated in various papers [169, 47, 117].

1.0.5 Gigahertz oscillators

One of the many applications of carbon nanotubes that has attracted much attention is the idea that they can be utilized as components in a nanoscale gigahertz oscillator [179]. Both experimental [31] and theoretical studies, including molecular dynamics simulation [94] and mathematical modeling [120, 27, 28], have shown that the sliding

of an inner shell inside an outer shell of a multi-walled carbon nanotube can generate oscillatory frequencies in the gigahertz range. However, a successful experimental realization for such nanoscale oscillators has yet to be reported. The concept of nanoscale oscillators is based upon the experiments of Cumings and Zettl [31] on multi-walled carbon nanotubes, who remove the cap from one end of the outer shell and attach a moveable nanomanipulator to the core in a high-resolution transmission electron microscope. By pulling the core out and pushing it back into the outer shell, they report an ultra-low sliding frictional force ($\sim 10^{-14}\text{N}\text{Å}^{-2}$), which is also confirmed by Yu et al. [177]. Further, Cumings and Zettl [31] observe that the extruded core, after release, quickly and fully retracts inside the outer shell due to the restoring force resulting from the van der Waals interaction acting on the extruded core. These experimental results led to the molecular dynamics studies of Zheng and Jiang [179] who show that the oscillating of the inner shell between the open ends of the outer shell of a multi-walled carbon nanotube generates a frequency in the gigahertz range. Molecular dynamics simulation undertaken by Legoas et al. [90], Rivera et al. [125, 126] and others also confirm such gigahertz frequency phenomena. From a mathematical modelling perspective, Baowan and Hill [7] investigate the force distribution for a double-walled carbon nanotube oscillator by utilizing the continuous approach for the Lennard-Jones potential together with Newton's second law, assuming a frictionless environment. They obtain an analytical expression for the interaction force and their model also predicts gigahertz oscillatory behavior for double-walled carbon nanotube oscillators.

Zheng and Jiang [179] suggest that the oscillatory frequency increases as the inner oscillating tube becomes shorter. This result leads to the molecular dynamics study of Liu et al. [94] on the oscillation of a C_{60} fullerene inside a single-walled carbon nanotube. While Liu et al. [94] focus on the oscillation frequency, the study of Qian et al. [120] concerns the suction and the repulsion of a C_{60} molecule in the vicinity of the tube's open end and the velocity of the molecule after being sucked into the nanotube. Based on the molecular dynamics simulation of both Liu et

al. [94] and Qian et al. [120], Cox et al. [27, 28] develop a mathematical model employing fundamental mechanical principles and classical applied mathematical techniques to determine the acceptance condition and the suction energies of the C_{60} fullerene upon entering a nanotube. They determine the minimum radius of a carbon nanotube for which the C_{60} fullerene will be accepted from rest and the maximum total energy once the C_{60} molecule is sucked inside the nanotube by the van der Waals forces. In addition, Cox et al. [27, 28] show that the gigahertz oscillatory behavior arises from the two peak-like forces operating at the nanotube's open ends. The analytical model of Cox et al. [27, 28] may be extended to more complicated gigahertz oscillators, including nanotube bundle oscillators for which the oscillating molecule inside the bundle is either a single nanotube or a C_{60} fullerene [30, 29].

Other types of nanoscale oscillators are also possible. Hilder and Hill [63, 62] find that gigahertz frequencies can also be obtained from a sector of a nanotorus orbiting inside a carbon nanotorus, and also for an atom or a C_{60} fullerene orbiting inside a nanotorus. In this thesis, we investigate further orbiting phenomenon at the nanoscale. In particular, we consider an atom and a C_{60} fullerene orbiting about the outside of a carbon nanotube and also a C_{60} fullerene orbiting around a C_{1500} molecule.

1.0.6 Connective tissue extracellular matrix

Structural polymers help to maintain an animal's body shape when experiencing large external tractions. Perhaps the most important structural polymer is collagen, which exists in the connective tissue extracellular matrix (CTs), for example, skin, cartilage and bone. CTs are bridged and bonded by anionic glycosaminoglycan GAGs, such as parallel rows of decoran, which are the only molecules in CTs apart from protein fibres that can be visualized by an electron microscope [141, 140, 153]. A pair of segments on neighboring collagen fibrils, which are linked by GAGs chains, is termed a shape module, and must deform reversibly to protect the general structure of the organism against various external stresses [55]. These GAGs transmit

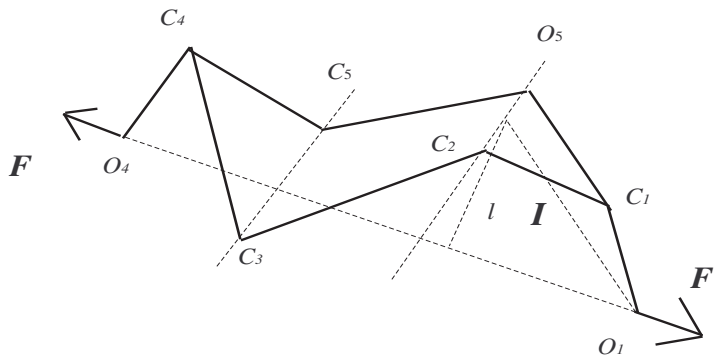

Figure 1.3: ${}^4C_1$ chair configuration. ${}^1C_4$ chair configuration can be viewed by flipping vertices C_1 and C_4 upside down (all the notations C_i and O_i we adopt here, are just for the sake of clarification). In addition, $\boldsymbol{F}$ and $\boldsymbol{I}$ denote applied force and lever respectively.

forces from the local area of molecules to global fibrils by converting compression into disseminated tensile stress [139]. The collagen and the elastin fibril behave mainly like a Hookean spring in the low stress limit, but the elasticity of GAGs' molecules is still under intensive investigation [21].

GAGs can go through conformational transitions, which are defined by the sudden elongation of bio-molecules due to the change in their atomic allocations without an increase in external forces. GAGs, e.g. pectinate, have two distinct chair structures, namely ${}^4C_1$ and ${}^1C_4$ [9] (see Fig. 1.3 for details), separated by an energy barrier of approximately 11 kcal/mol [73]. Moreover, there exists a boat conformation ${}^{1,4}B$ (see Fig. 1.4 for details) with an energy level of approximately $5-8$ kcal/mol above the most stable ${}^4C_1$ chair energy [35]. In the low energy configuration, nature prefers the ${}^4C_1$ chair state over other possible states because it possesses the minimum energy configuration. However, under an external stress, these polysaccharides can undergo two conformational transitions reversibly beyond some critical stresses [99]. For example, amylose undergoes its first conformational transition when the applied force is around 200 pN and its second transition when the applied force is around 500 pN. However, some polysaccharides like pigskin DS only go through one transition, while other polysaccharides like poly-anionic HA, neutral methyl cellulose and poly-cationic chitosan undergo no transitions at all. The reason for these conformational transitions is closely linked to the total number of axial or equatorial linkages exist-

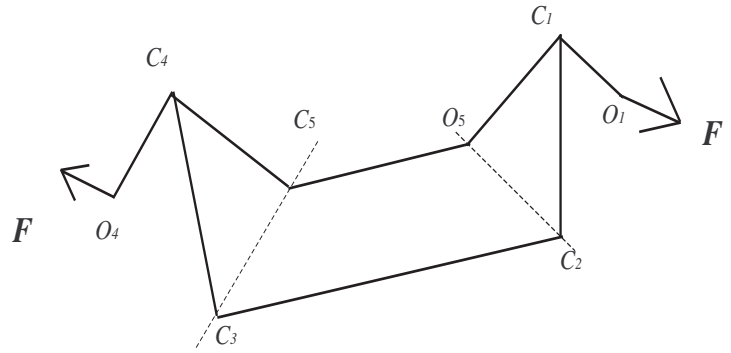

Figure 1.4: $^{1,4}B$ boat configuration.

ing in each pyranose ring (monosaccharide). It is evident that the glycosidic linkages I, which are indicated in Fig. 1.3 may act as levers to generate a sufficient torque to undertake the work done, which is necessary to perform ring conformational transitions. Hence only glycosidic linkages with axial linkages can generate enough torque to flip the levers beyond a given critical stress while equatorial linkages can not. For a more extensive treatment of the conformational transitions, see Marszalek et al. [99] for details. This phenomena provides a crucial step for a molecule to transform from the entropic region into the Hookean regime. Although the above interpretation of the kinking conformational changes is largely accepted by most researchers, there exists alternative interpretations to explain these conformational transitions [85].

1.0.7 Thesis structure

This thesis is presented in six parts. Chapter 1 comprises the introduction and background. Chapter 2 examines the mechanics of three proposed nanostructures, namely the gigahertz oscillators, the nano tippe top and the nanoscale orbiting systems. Chapter 3 develops various continuum mechanical models for the axial buckling of carbon nanotubes and nanopeapods and their applications in nano-electromechanical systems. Chapter 4 investigates the worm-like chain model for stretched semi-flexible molecules by utilizing a variational principle and discusses applications to structural polymers. Chapter 5 contains the conclusion of the thesis

and finally Chapter 6 comprises the Appendices[1].

[1]Due to the diverse areas discussed in this thesis, all symbols are consistent throughout each section but may vary across different sections. In addition, at the end of each chapter, there is a list of symbols for that chapter, which a different list for each of the sections in the chapter. These lists comprise the page number where the symbol is first defined.

Chapter 2

Nanomechanics

In this Chapter, we investigate the mechanics of three distinct nanoscale systems, namely the spiral motion of a C_{60} fullerene inside a carbon nanotube, the spinning motion of a C_{60} fullerene which is joined by a small carbon segment, subsequently referred to as a nano tippe top which is precessing on a graphene sheet or the interior of a nanotube, and certain nanoscale two body problems which resemble planetary motion of the solar system. Both the continuous approximation and the dynamics of rigid bodies are employed to formulate for these problems.

2.1 Spiral motion of carbon atoms and C_{60} fullerenes inside single-walled carbon nanotubes

In this section, we investigate the scenario in which an atom or a C_{60} fullerene is oscillating in the axial direction of a carbon nanotube and it is also spiraling inside the nanotube about its axis. Such spiral motion is particularly prominent if the van der Waals forces arising between the nanotube wall and the molecules confine the defining path of the atom or the C_{60} fullerene. Although at present this oscillatory motion has yet to be experimentally confirmed, we can mathematically model such motions by adopting the continuous approach to approximate the van der Waals interactions and then utilizing Newton's second law to determine the equations of

motion of the atom or the C_{60} molecule inside the nanotube. Our model differs from other theoretical studies mentioned above since the spiral motion is predicted solely from a mechanical perspective without taking into account either the symmetries of the C_{60} fullerene or the helical structure of the nanotubes. Although we do not directly take into account any thermal effects into the derivation of the equations of motion of the atom or the fullerene, we may identify the root mean square velocity of the atom or the fullerene through classical kinetic theory, which can be related to the temperature of the system. Such a root mean square velocity can then be utilized to calculate the centrifugal forces experienced by the atom or the fullerene, which counteract the repulsive van der Waal forces between the nanotube and the atom or the fullerene, giving rise to a path of the atom or the fullerene at a preferred radius while oscillating axially inside the nanotube. We first examine how a single carbon atom behaves inside a nanotube and then we extend this case to the behavior of a C_{60} fullerene inside a nanotube taking into account a frictional effect.

In the following sub-section, we briefly state the interaction energy between two molecules upon adopting the continuous approach. In sub-section 2.1.2, we assume cylindrical symmetry of the nanotube and determine the mutual forces acting on a single carbon atom inside a single-walled carbon nanotube. As a result, we can determine the trajectory of the atom by requiring that the net force, which comprises both the van der Waals forces and the centrifugal forces due to the atomic circular motion, to vanish at the equilibrium configuration. In sub-section 2.1.3, we discuss the frictional force at the nanoscale. In sub-section 2.1.4, we incorporate the frictional form derived in sub-section 2.1.3 to investigate the motion of a C_{60} fullerene inside a nanotube. Some conclusions and possible future research directions are given in the final sub-section.

2.1.1 Potential energy between molecules

The total non-bonded pairwise molecular interactions is conventionally obtained by summing all of the interaction energies between each atomic pair E, namely

$$E = \sum_i \sum_j \Phi\left(\rho_{ij}\right), \tag{2.1}$$

where $\Phi(\rho_{ij})$ denotes the potential function between atoms i and j separated by a distance ρ_{ij}. Upon adopting the continuous approach, which assumes that the carbon atoms are uniformly distributed over the surfaces of the C_{60} fullerene and the nanotube, we can approximate Eq. (2.1) by the double surface integral

$$E = n_t n_f \int_{\Sigma_t} \int_{\Sigma_f} \Phi(\rho) dS_f dS_t, \tag{2.2}$$

where n_t, n_f, ρ, dS_f and dS_t denote the mean atomic surface density of the nanotube, the mean atomic surface density of the C_{60} molecule, the distance between two typical surface elements, and the surface elements of the C_{60} molecule and the nanotube, respectively. The value of the constants utilized in this thesis are given in Table 2.1. In particular, the potential function adopted here is the classical Lennard-Jones potential,

$$\Phi = -\frac{A}{\rho^6} + \frac{B}{\rho^{12}}, \tag{2.3}$$

where A and B denote the attractive and the repulsive constants respectively. From Eq. (2.2), the non-bonded molecular potential energy between two molecules can be written as

$$E = n_t n_f \int_{\Sigma_t} \int_{\Sigma_f} \left(-\frac{A}{\rho^6} + \frac{B}{\rho^{12}}\right) dS_f dS_t. \tag{2.4}$$

We note that for the case of a carbon atom oscillating inside a nanotube, only a single surface integral over the nanotube is necessary.

Radius of (6,6)	$a = 4.071$ Å
Radius of (10,10)	$a = 6.766$ Å
Radius of (16,16)	$a = 10.860$ Å
Radius of C_{60}	$b = b_1 = 3.55$ Å
Radius of C_{1500}	$b_2 = 17.5225$ Å
Carbon-carbon bond length	$\sigma = 1.421$ Å
Mean surface density of a single layer graphene	$n_t = 0.3812$ Å^{-2}
Mean surface density of C_{60}	$n_f = n_1 = 0.3789$ Å^{-2}
Mean surface density of C_{1500}	$n_2 = 0.3789$ Å^{-2}
Mass of a single carbon atom	$m_a = 1.993 \times 10^{-26}$ kg
Mass of a single C_{60} fullerene	$m = m_1 = 1.196 \times 10^{-24}$ kg
Mass of a single C_{1500} fullerene	$m_2 = 2.990 \times 10^{-23}$ kg
Attractive constant	$A = 17.4$ eV$\times$ Å^6
Repulsive constant	$B = 29 \times 10^3$ eV$\times$Å^{12}

Table 2.1: Numerical values of constants utilized in Section 2.1 and Section 2.3.

2.1.2 Oscillatory motion of carbon atom inside a single-walled carbon nanotube

In this sub-section, we examine the dynamics of a single carbon atom oscillating inside a single-walled carbon nanotube. Although the case of an isolated single carbon atom does not generally exist, the mathematics involved in calculating the molecular potential energy between the atom and the nanotube and the corresponding residual molecular force are relatively simple and they can be conceptually extended to the study of more complicated molecular structures, such as the molecular interactions between a C_{60} fullerene and a nanotube. Since the atomic distance between the carbon atom and the nanotube is sufficiently large, even though the carbon atom has four valance electrons, these electrons will not tend to form chemical bonding with the wall of the nanotube. As a result, the friction between the carbon atom and the single-walled carbon nanotube can be neglected in this case [31].

Following the work of Cox et al. [27] (here, we develop a more realistic mathematical model by incorporating both the thermal and frictional effects into the existing gigahertz oscillatory model developed by Cox et al. [27, 28] to investigate both the stable and unstable spiral motions instead of a pure linear motion of the

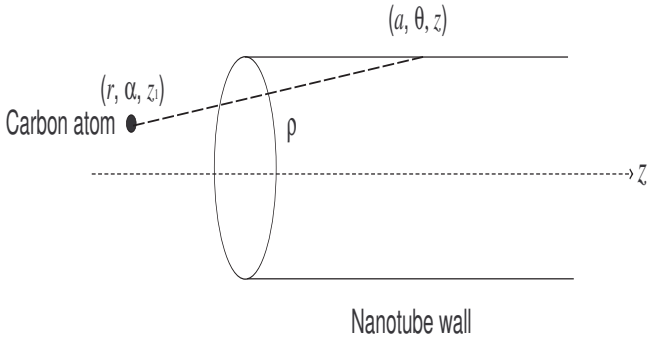

Figure 2.1: Atom-nanotube system.

carbon atom and the C_{60} fullerene inside carbon nanotubes of various radii), upon utilizing a cylindrical coordinate system, we can parametrize the position of the atom and an arbitrary point on the wall of the nanotube by (r, α, z_1) and (a, θ, z) respectively, where a denotes the radius of the nanotube (see Fig. 2.1). We can then determine the distance ρ between the atom and an arbitrary atom on the wall of the nanotube in terms of the prescribed parametrization, which is given by

$$\rho = \left[a^2 + r^2 - 2ar\cos(\theta - \alpha) + (z - z_1)^2\right]^{1/2}. \tag{2.5}$$

The molecular potential energy between the atom and the nanotube can be found by utilizing Eq. (2.4) to become

$$E = an_t \int_{-\pi}^{\pi} \int_{-\infty}^{\infty} \left(\frac{-A}{\rho^6} + \frac{B}{\rho^{12}}\right) dz d\theta. \tag{2.6}$$

Upon making the following substitution $\lambda = [a^2 + r^2 - 2ar\cos(\theta - \alpha)]^{1/2}$, we obtain $\rho = [\lambda^2 + (z - z_1)^2]^{1/2}$. We further substitute $z - z_1 = \lambda \tan\psi$, leading Eq. (2.6) to

$$E = an_t \int_{-\pi}^{\pi} \int_{-\pi/2}^{\pi/2} \left(\frac{-A\cos^4\psi}{\lambda^5} + \frac{B\cos^{10}\psi}{\lambda^{11}}\right) d\psi d\theta. \tag{2.7}$$

Upon utilizing the established result from [69], for positive integers m we have

$$\int_{-\pi/2}^{\pi/2} \cos^{2m}\psi d\psi = \frac{(2m-1)!!\pi}{(2m)!!}, \tag{2.8}$$

where !! denotes a double factorial operator, which is defined by $(2m)!! = 2 \cdot 4 \cdot 6 \cdot \ldots \cdot 2(m-1) \cdot 2m$ and $(2m-1)!! = 1 \cdot 3 \cdot 5 \cdot \ldots \cdot (2m-3) \cdot (2m-1)$. As a result, E becomes

$$E = \frac{3\pi a n_t}{8} \int_{-\pi}^{\pi} \left(-\frac{A}{\lambda^5} + \frac{21B}{32\lambda^{11}} \right) d\theta = \frac{3\pi a n_t}{8} \left[-AI_5 + \frac{21B}{32} I_{11} \right], \tag{2.9}$$

where the integral I_n are defined as

$$I_n = \int_{-\pi}^{\pi} \frac{1}{\lambda^n} d\theta = \int_{-\pi}^{\pi} \frac{1}{\left[a^2 + r^2 - 2ar\cos(\theta - \alpha)\right]^{n/2}} d\theta.$$

In the Appendix A of Cox et al. [27], these integrals have been evaluated in terms of the generalized hypergeometric function, thus

$$E = \frac{3\pi a n_t}{8} \left[-\frac{2A\pi}{N^{5/2}} F\left(\frac{5}{2}, \frac{1}{2}; 1; -\frac{M}{N}\right) + \frac{21B\pi}{16N^{11/2}} F\left(\frac{11}{2}, \frac{1}{2}; 1; -\frac{M}{N}\right) \right], \tag{2.10}$$

where F denotes the hypergeometric function, $N = (a-r)^2$ and $M = 2ar$. From Eq. (2.10), we can obtain the atomic force acting on the atom in the r, the θ and the z directions by $\boldsymbol{F}_{vdW} = -\nabla E$, where ∇ denotes the usual gradient operator. To relate this van der Waals forces with the other mechanical forces such as the centrifugal forces arising from the atomic circular motion, we derive the full expression for the atomic forces by utilizing the cylindrical symmetry of the nanotube and the resulting force components are as follows:

$$F_r = -\frac{\partial E}{\partial r}, \qquad F_\theta = -\frac{1}{r}\frac{\partial E}{\partial \theta}, \qquad F_z = -\frac{\partial E}{\partial z}. \tag{2.11}$$

We note that the distant interactions between molecules can be modeled by classical mechanics as long as energy exchange between molecules does not generally exist [95]. It is noteworthy from Eq. (2.10) that E only depends on r and therefore we have $F_\theta = F_z = 0$. Employing Newton's second law, the three mutual equations for the atomic forces can be shown to become

$$\begin{aligned} F_r &= -\frac{\partial E}{\partial r} = m\left[\ddot{r}(t) - r(t)\dot{\theta}(t)^2\right], \\ F_\theta &= m\left[2\dot{r}(t)\dot{\theta}(t) + r(t)\ddot{\theta}(t)\right] = F_z = m\ddot{z}(t) = 0, \end{aligned} \tag{2.12}$$

where m denotes the mass of a particle, and from which we can deduce that $z(t)$ adopts the form $z(t) = Ct + D$, where C and D denote arbitrary constants. Hence the translational velocity v_t in the z-direction is constant. This result has been separately confirmed by Cox et al. [27] who show that the atom oscillates linearly inside the nanotube in the axial direction. Since $F_\theta = 0$, we can then recast Eq. $(2.12)_2$ in terms of an integral upon utilizing $d/dt[r^2(d\theta/dt)] = 0$ to obtain

$$h = r(t)^2\frac{d\theta}{dt}, \tag{2.13}$$

where the constant h is referred to as the angular momentum of the atom. To obtain the radial acceleration, from Eq. $(2.12)_1$, we have

$$\frac{d^2r}{dt^2} = \frac{h^2}{r(t)^3} - \frac{1}{m}\frac{dE}{dr}. \tag{2.14}$$

If we assume that the atom stays at a preferred stable radius r_s, the acceleration of the atom at r_s has to vanish and we obtain

$$F_r = -\frac{mv^2}{r_s}, \tag{2.15}$$

where v denotes the circumferential velocity of the atom inside the nanotube and we note that F_r denotes the centripetal forces generated by the repulsive van der Waals forces, which must have the same magnitude but in the opposite direction to the centrifugal forces mv^2/r_s caused by the circular motion. The combination of the circular motion and the linear translational velocity in z-direction defines the spiral-like path of the atom.

Here, we first investigate a carbon atom inside a (6,6) and a (10,10) nanotube. We ignore the frictional force between the atom and the nanotube due to the ultra-low frictional effect at the nanoscale for the atom-nanotube system. The molecular potential energies E as a function of the radial distance r from the axis of the (6,6) and (10,10) nanotubes are described by Eq. (2.10) and are plotted in Fig. 2.2. The minimum energy configurations for the proposed systems are reported as -0.15 eV and -0.1 eV with the corresponding preferred radial distances r_0 of 0.48 Å and 3.25 Å respectively. We note that here the subscript "0" denotes the ideal system without taking the centrifugal forces into account for the circular motion of the carbon atom inside the nanotube. It is interesting to note that the interaction energy as a function of distance between the carbon atom and the (6,6) and (10,10) nanotubes shows some substantial differences because the carbon atom is confined by the large curvature induced by (6.6) nanotube, from which it restricts the carbon atom almost at the center of the (6,6) nanotube. These minimum energy configurations can be demonstrated by investigating the radial forces acting on the atom described by Eq. $(2.12)_1$. We plot the radial forces for the proposed systems in Fig. 2.3 and note that while the atomic force attracts the atom towards r_0 from the axis due to the attractive van der Waals forces, it is pushing away from the wall of the nanotube

due to the repulsive van der Waals forces. In particular, the radial force is zero when the atom is located at its preferred position r_0. We comment that the van der Waals forces acting on the atom at $r = 0$ is also zero but it is not stable due to the fact that a small perturbation from the axis, i.e. $r = \varepsilon$ where ε denotes a small non-zero quantity, will push the atom away from $r = 0$. If the atom is sucked into the nanotube in the axial direction, the dynamics is a purely linear oscillatory motion. That is, the atom will oscillate inside the nanotube at r_0 with a gigahertz frequency in the z-direction [27, 28]. However if the atom is sucked into the nanotube in the non-axial direction, for example due to thermal fluctuations, the resulting preferred radial position r_s will be bigger than r_0 owing to the induced centrifugal forces caused by thermal fluctuations acting on the atom. It is easy to observe that the carbon atom is always unstable when $r < r_0$ for both the axial and non-axial intrusions. For the latter case, the resultant path (r_s, α, z_1) hence forms a spiral-like motion, which can be determined by balancing the van der Waals forces $\boldsymbol{F}_{vdW} = -\nabla E$ with the centrifugal forces given by Eq. (2.15).

The circumferential velocity v, which keeps the atom at the preferred radial distance r_s is shown in Fig. 2.4. We note that for all proposed nanotubes, $v = 0$ when $r_s = r_0$, which corresponds to the case of the ideal system while for other nonzero values of v, r_s will differ by the amount of the centrifugal forces induced by thermal fluctuations. It is easy to observe that r_s possesses a positive relationship with the circumferential velocity v, which implies that the higher the circumferential velocity, the closer the atom will be to the wall of the nanotube. The physical circumferential velocity may be estimated by the kinetic theory assuming that the atom is sucked into the nanotube at room temperature $T = 300$ K. The root mean square velocity v_{rms} for an arbitrary direction of a non-interacting atom at room temperature can be calculated from $v_{rms} = \sqrt{k_B T/m_a} = 456\ \text{ms}^{-1}$, where m_a and k_B denote the mass of the single carbon atom and Boltzmann's constant respectively. Upon comparing the root mean square velocity with the circumferential velocity in Fig. 2.4, we find that on average, the atom has a stable spiral trajectory at $r_s = 0.6$ Å and $r_s = 3.32$ Å for

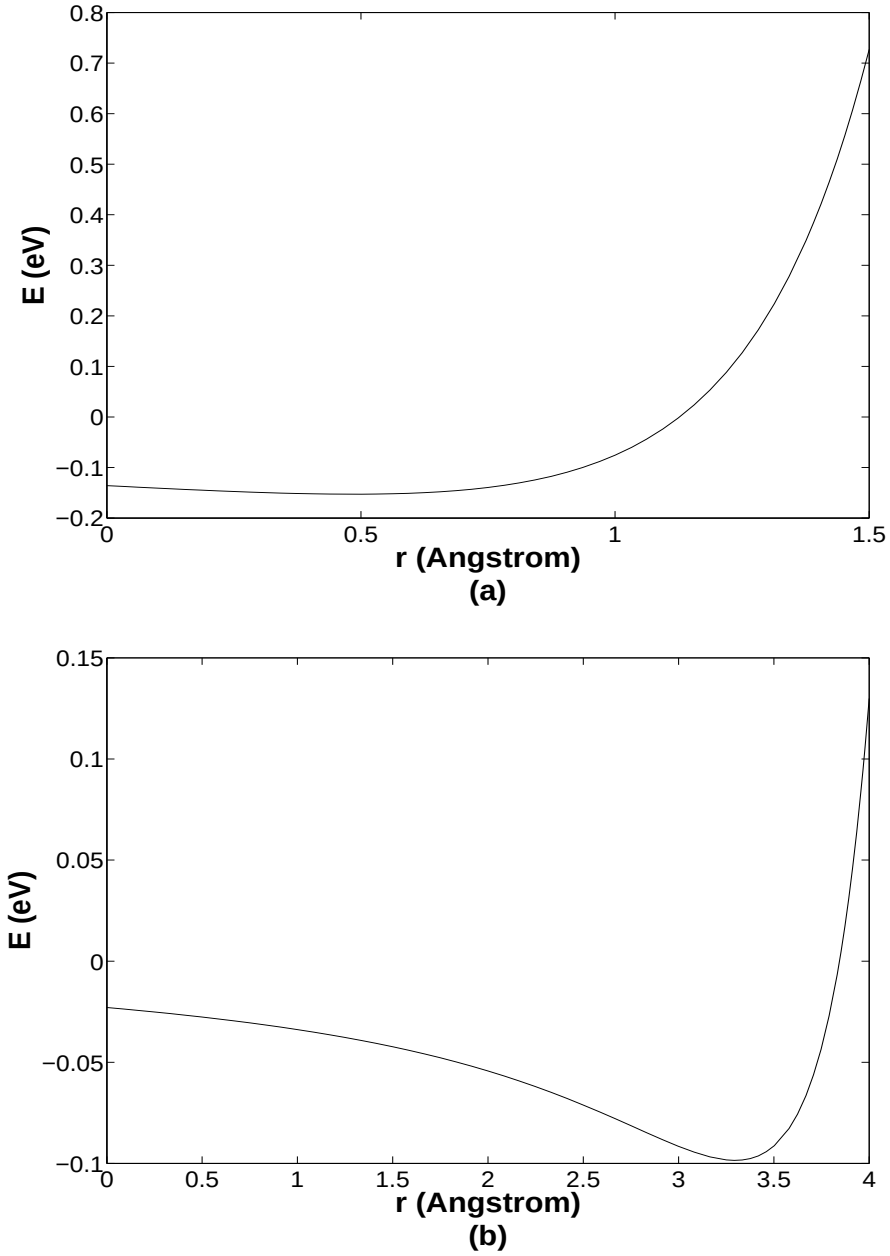

Figure 2.2: Interaction energy E of carbon atom at distance r from the axis of (a) (6,6) and (b) (10,10) carbon nanotube.

the (6,6) and (10,10) nanotubes respectively. Hence, we can conclude that the spiral path of the atom inside the (10,10) nanotube is more prominent than that of the (6,6) nanotube. This indicates that the nanotube curvature serves to strengthen the interactions between the atom and the wall of the nanotube to create the spiral-like path. However, if the curvature is very large, as in the case for the (6,6) nanotube, spiral motion will unlikely to be observed because the atom is forced to move to the axis of the (6,6) nanotube.

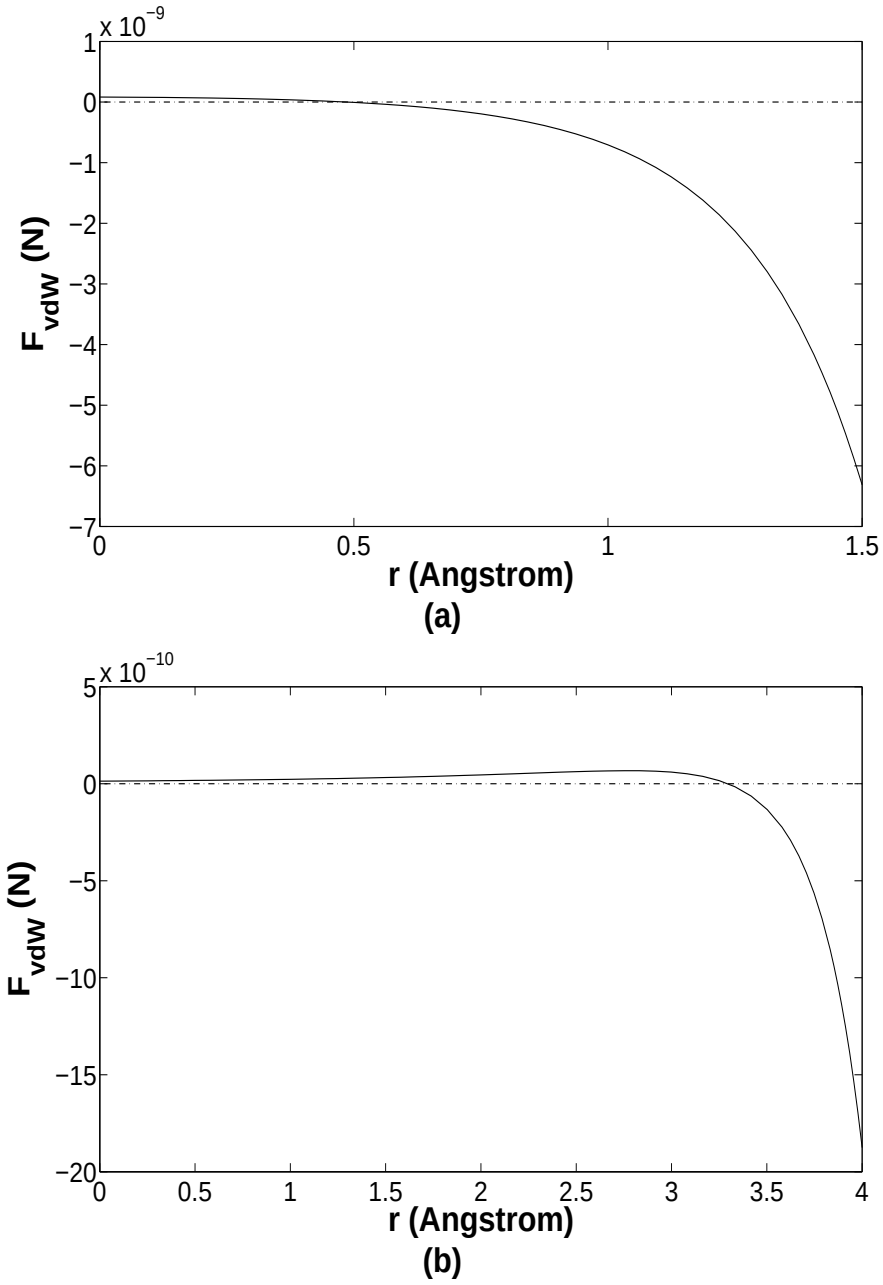

Figure 2.3: Atomic force F_{vdW} of carbon atom at distance r from the axis of (a) (6,6) and (b) (10,10) carbon nanotube.

These findings are compatible with the molecular dynamics simulation performed by Gan et al. [46], who show that the escaped carbon atoms inside a (10,10) nanotube, after introducing an electron beam cut on the (10,10) nanotube, follow a spiral trajectory at $T = 775$ K. From our model, we can calculate $v_{rms} = 732$ ms^{-1} at $T = 775$ K for the carbon atom, and hence we predict that the spiral motion occurs at $r_s = 3.38$ Å.

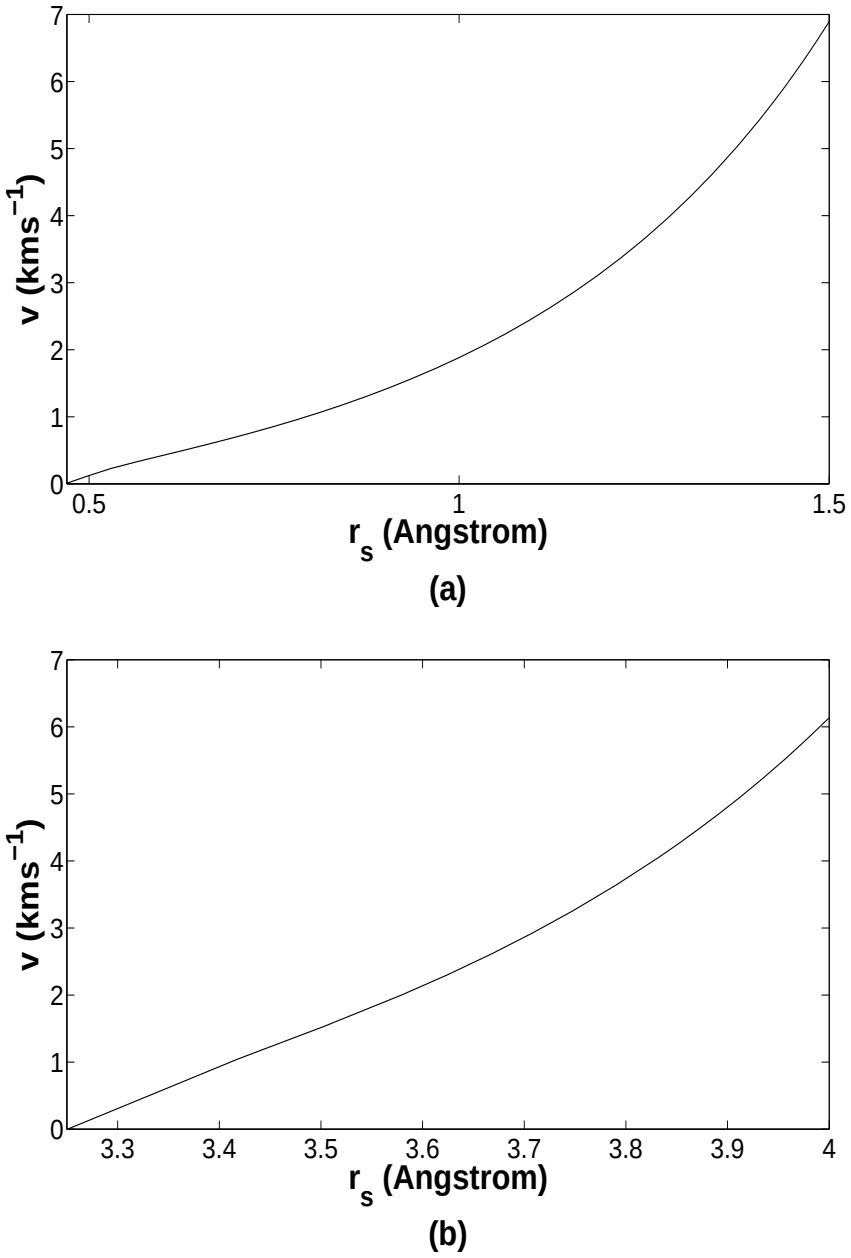

Figure 2.4: Circumferential velocity v of carbon atom at preferred radius r_s from the axis of (a) (6,6) and (b) (10,10) carbon nanotube.

2.1.3 Frictional force at nanoscale

The dynamics of a C_{60} fullerene is more complicated than that of a single atom since the C_{60} fullerene can admit both rotational and vibrational degrees of freedom which are not present for the carbon atom. Moreover, for the C_{60} the frictional effect may be far more significant than that for the atom, and therefore we incorporate a frictional force between the C_{60} fullerene and the nanotube into our model. There

are a number of experimental, molecular dynamics simulation and analytical studies [42, 58, 142, 144] aiming to determine the frictional force at the nanoscale. In terms of experimental investigations, these mainly involve the application of scanning tunneling microscopy [15] and atomic force microscopy [14] to find the force spectrum of the targeted molecules. In particular, experimental results suggest that the frictional force at the nanoscale is ultra-low [41, 80] leading to neglecting the frictional effect for the case of atom-nanotube oscillators, as in the previous sub-section. Furthermore, frictional force can be classified as either dissipative or non-dissipative, where the former case represents a non-reversible dynamical process due to the energy losses to the environment, usually in the form of heat or sound. The latter case has been adopted by Zheng and Jiang [179] where the non-dissipative frictional force resulting form the inter-atomic locking is assumed to cause a frictional effect on the double-walled nanotube gigahertz oscillator. Here, we examine the notion of a dissipative frictional force between the C_{60} molecule and the nanotube at the nanoscale. Since both the C_{60} fullerene [4, 165] and the carbon nanotube [119, 118, 102] possess dielectric properties, we can adopt a dynamical force arising from electromagnetic fluctuations [32] to determine such a frictional force. The simplest possible case that can be considered is the frictional force between a moving dielectric atom and a cylindrical surface [86]. The general atom-surface interactions U and the rate of energy dissipation W can be described by

$$U = -\frac{1}{2} < \mathbf{d} \cdot \mathbf{E_0} >, \qquad -\frac{dW}{dt} = \int < \mathbf{j} \cdot \mathbf{E_0} > dr = \mathbf{F_f} \cdot \mathbf{V}, \tag{2.16}$$

where $\mathbf{d}$, $\mathbf{j}$, $\mathbf{E_0}$, $\mathbf{F_f}$ and $\mathbf{V}$ denote the bulk dipole moment, the current density, the interacting electrical field, the frictional force and the horizontal velocity of the atom respectively. Assuming a cylindrical symmetry of the nanotube, Kyasov and Dedkov [86] find that the frictional force can be expressed as equation (18) given in Kyasov and Dedkov [86]. Although this equation incorporates the curvature of the cylindrical surface, it is extremely difficult to work with, at least for our current

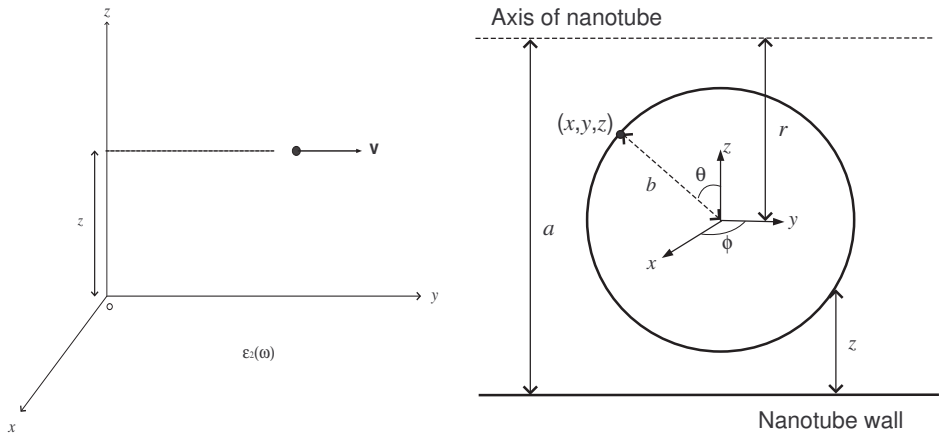

Figure 2.5: Schematic of electromagnetic interactions between a carbon atom and a graphite layer (left) and between a C_{60} and the graphite layer (right), moving parallel with (x,y) plane.

purposes, and therefore we adopt a simpler form of equation (18) as given in Kyasov and Dedkov [86] by assuming that the curvature of the cylindrical surface is zero, which is particularly valid provided that the van der Waals forces is a "short" range interactions and that the radius of the nanotube is sufficiently large. One may then find the following simple expression for the frictional force $F_f \sim V/z^5$, where z and V denote the perpendicular distance between the atom and the flat surface and the horizontal velocity respectively (See Fig. 2.5 for details). In order to determine the total frictional force F_f^{tot} between the C_{60} fullerene and the graphene sheet, we simply integrate the frictional force F_f over the entire surface of the C_{60} fullerene, namely

$$F_f^{tot} = -\left(\int_{\Sigma_f} \frac{c}{z^5} dS_f\right) V, \tag{2.17}$$

where c denotes a physical constant, which is both frequency and temperature dependent, $dS_f = b^2 \sin\theta d\theta d\phi$ and $z = a - r + b\cos\theta$, as indicated in Fig. 2.5. Note that a and b denote the radius of the nanotube and the C_{60} fullerene respectively. However, we do not determine the constant c from first principles due to the tedious expression of the frequency dependent atomic polarization and the dielectric func-

tion of the graphene sheet. We simply determine the value of c by fitting Eq. (2.17) with a molecular dynamics simulation result [52]. Upon integrating, we obtain

$$\begin{aligned} F_f^{tot} &= -\frac{\pi c b}{2}\left\{\frac{1}{(a-r-b)^4}-\frac{1}{(a-r+b)^4}\right\}V, \\ &= -4\pi b^2 c\left\{\frac{(a-r)\left[(a-r)^2+b^2\right]}{\left[(a-r)^2-b^2\right]^4}\right\}V = -\eta(r)V, \end{aligned} \tag{2.18}$$

where $\eta(r)$ denotes the usual frictional coefficient but which depends on the radius r. We note that this frictional coefficient is proportional to the area of the overlapping section b^2, which is consistent with the perspective of modern tribology. This total frictional force will be utilized to represent the energy dissipation between the C_{60} fullerene and the nanotube in the next sub-section. To proceed, we determine the coefficient c by matching Eq. (2.18) with the molecular dynamics simulation results given by Haibin et al. [52], who study the dynamical frictional force due to phonon excitation for the C_{60}@(10,10) nanopeapod oscillator. Upon substituting $F_f = 150$ pN, $a = 6.77$ Å, $b = 3.55$ Å, $r = 0$ Å (since Haibin et al. [52] assume the axially oscillatory motion of a C_{60} fullerene inside a (10,10) nanotube) and $v_t = V = 480\text{ms}^{-1}$ into Eq. (2.18), we obtain $c = 6.04 \times 10^{-42}$ kgm^{3}s^{-1} at $T = 300$ K. Fixing the temperature $T = 300$ K, we can plot the frictional force against the C_{60} velocity V in Fig. 2.6. Again this result agrees well with the result obtained by Haibin et al. [52], especially within the linear force regime.

2.1.4 Oscillatory motion of C_{60} fullerene inside a single-walled carbon nanotube

In this sub-section, we extend the model developed by Cox et al. [27] to investigate the dynamical behavior of a C_{60} fullerene inside a single-walled carbon nanotube by considering the frictional effect arising from the molecular interactions between molecules within a short range r to determine the unstable spiral motion of the C_{60} inside the nanotubes and its final oscillatory frequency. However, for the time

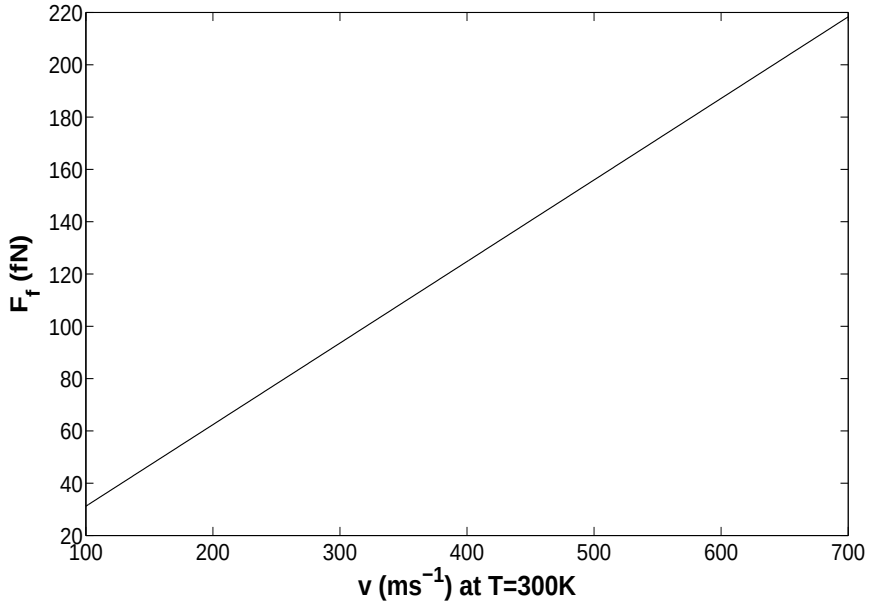

Figure 2.6: Frictional force against the translational velocity of C_{60} inside (10,10) with $T = 300$K and $r = 0$.

being we first ignore the frictional force and only consider the spiral motion of a C_{60} fullerene inside a single-walled carbon nanotube, in particular the (10,10) and (16,16) nanotubes. Later we incorporate the frictional force into our model to study a more realistic oscillatory phenomenon of such gigahertz oscillators. We parametrize the center of the fullerene by $(r,\ \alpha,\ Z)$ and an arbitrary point on the shell of the nanotube by $(a,\ \theta,\ z)$, where a denotes the radius of the nanotube. The distance from the center of the fullerene to a point on the wall of the nanotube is hence given by

$$\rho = \left[a^2 + r^2 - 2ar\cos(\theta - \alpha) + (z - Z)^2\right]^{1/2}. \tag{2.19}$$

The carbon atoms are assumed to be uniformly distributed over the surfaces of both the fullerene and the nanotube, so that we can then adopt a continuous approach to average out the molecular potential energy between the fullerene and the carbon nanotube by a double surface integral, i.e. Eq. (2.2). Following the Appendix A of Cox et al. [27], by performing the surface integral of the Lennard-Jones potential

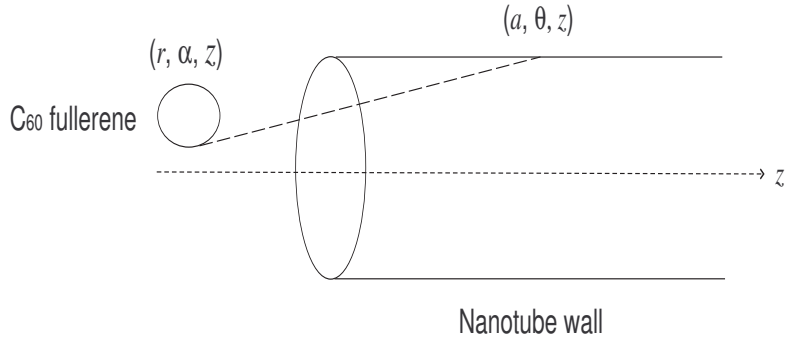

Figure 2.7: Fullerene-nanotube system.

over the surface of the fullerene, it can be shown that the molecular energy between an arbitrary point on the nanotube and the entire C_{60} molecule is given by

$$P = \frac{2n_f\pi b}{\rho}\left\{\frac{A}{4}\left[\frac{1}{(\rho+b)^4}-\frac{1}{(\rho-b)^4}\right]-\frac{B}{10}\left[\frac{1}{(\rho+b)^{10}}-\frac{1}{(\rho-b)^{10}}\right]\right\}, \quad (2.20)$$

where ρ denotes the distance between the center of the fullerene and an arbitrary point on the nanotube surface. Now, the molecular potential energy between the C_{60} fullerene and the nanotube can be determined by performing another surface integral of Eq. (2.20) over the cylindrical shell of the nanotube. That is

$$E = an_t\int_{-\pi}^{\pi}\int_{-\infty}^{\infty}Pdzd\theta. \quad (2.21)$$

Following [28], upon making $\lambda^2 = a^2+r^2-2ar\cos(\theta-\alpha)-b^2$ and $\ell = z-Z$, which result in $\rho^2 = \lambda^2+b^2+\ell^2$, we can rewrite Eq. (2.20) as

$$\begin{aligned} P &= 4\pi b^2 n_f\left\{\frac{B}{5}\left[\frac{5}{(\lambda^2+\ell^2)^6}+\frac{80b^2}{(\lambda^2+\ell^2)^7}+\frac{336b^4}{(\lambda^2+\ell^2)^8}+\frac{512b^6}{(\lambda^2+\ell^2)^9}+\frac{256b^8}{(\lambda^2+\ell^2)^{10}}\right]\right. \\ &- \left. A\left[\frac{1}{(\lambda^2+\ell^2)^3}+\frac{2b^2}{(\lambda^2+\ell^2)^4}\right]\right\}. \end{aligned} \quad (2.22)$$

Given that, E can be shown to be given by

$$E = 4\pi^2 ab^2 n_t n_f \Bigg\{ \frac{B}{5}\left(\frac{315}{256}I_{11} + \frac{1155b^2}{64}I_{13} + \frac{9009b^4}{128}I_{15} + \frac{6435b^6}{64}I_{17} + \frac{12155b^8}{256}I_{19}\right) - \frac{A}{8}\left(3I_5 + 5b^2 I_7\right)\Bigg\}, \tag{2.23}$$

where

$$I_n = \frac{2\pi}{\left[(a-r)^2 - b^2\right]^{n/2}} F\left(\frac{n}{2}, \frac{1}{2}; 1; -\frac{4ar}{(a-r)^2 - b^2}\right).$$

C_{60}@(10,10) and C_{60}@(16,16) are utilized as the only two examples in this subsection and the graph of E, which is derived from Eq. (2.23) with respect to the radial distance r from the axis of the (10,10) and (16,16) nanotubes are plotted in Fig. 2.8. The minimum energy configurations for the two proposed systems are reported as -3.2 eV and -1.2 eV with the corresponding preferred radius of $r_0 = 0$ Å and 4.28 Å respectively. We then utilize Eq. $(2.12)_1$ and plot the radial forces as a function of r for the C_{60} fullerene inside the (10,10) and (16,16) nanotubes in Fig. 2.9. Again we consider the circular motion of the C_{60} fullerene inside the nanotubes and the circumferential velocity of the C_{60} fullerene inside the (10,10) and (16,16) nanotubes are plotted in Fig. 2.10. Such circular motion can be induced from the thermal fluctuations and so that we calculate the root mean square velocity v_{rms} of the C_{60} fullerene at room temperature $T = 300$ K as $v_{rms} = \sqrt{k_B T/m} = 59$ ms^{-1}, where m denotes the mass of a C_{60} fullerene. If we make the comparison between the v_{rms} and the circumferential velocity given in Fig. 2.10. On average, we can determine the preferred radial position r_s for the (10,10) and (16,16) nanotubes as 0.08 Å and 4.3 Å respectively. We conclude that the spiral motion of the C_{60}@(16,16) is more prominent than the spiral motion of the C_{60}@(10,10).

Since the C_{60} fullerene moves closer to the tube wall as it is orbiting about the axis of the nanotube, we can no longer neglect the frictional effect. We note

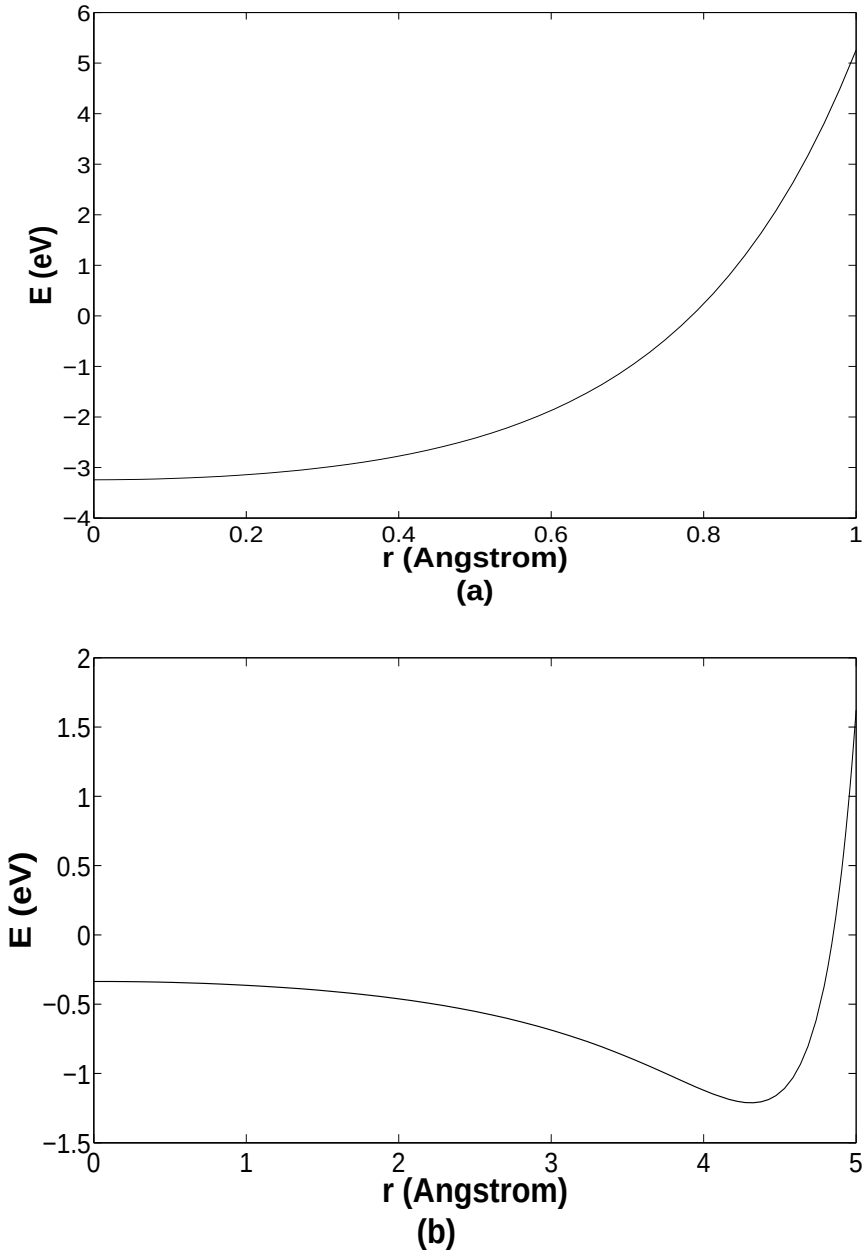

Figure 2.8: Interaction energy E of C_{60} at distance r from the axis of (a) (10,10) and (b) (16,16) carbon nanotube.

that Eq. (2.18) derived in the previous sub-section will be utilized to determine the frictional force in this sub-section. As a comparison with previous molecular dynamics simulation results, we simply choose the C_{60}@(10,10) as an example and the whole physical process is given as follows. Once the C_{60} fullerene is sucked into the (10,10) nanotube in the non-axial direction, the frictional force between molecules slows down the circumferential velocity of the C_{60} fullerene from $v = 59$ ms^{-1} to 0 ms^{-1} where we can determine the transitional time t^* from the spiral-

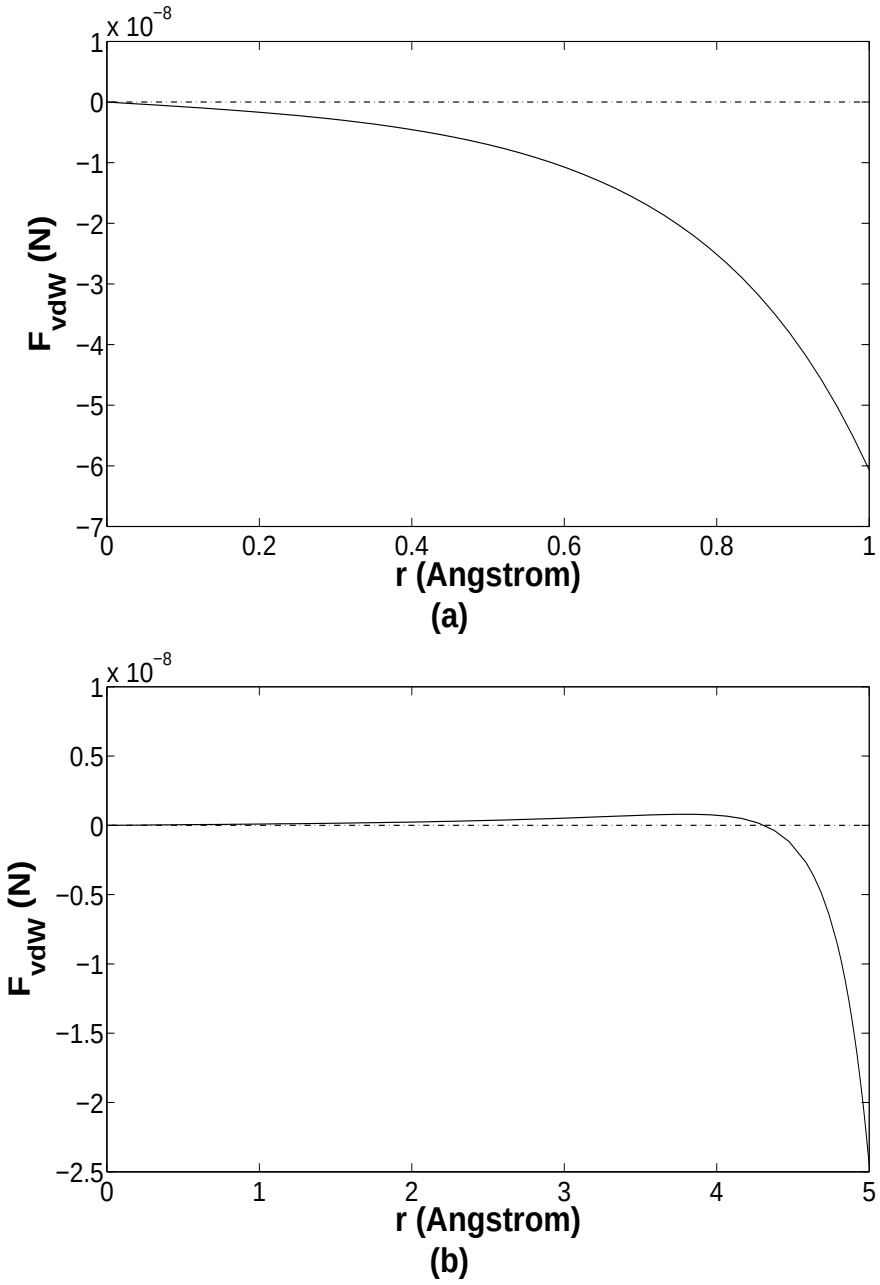

Figure 2.9: Molecular force F of C_{60} at distance r from the axis of (a) (10,10) and (b) (16,16) carbon nanotube.

like motion at r_s to the linear oscillatory motion at r_0. Given t^*, we can then determine the reduction in the translational velocity v_t of the C_{60} fullerene and therefore the resultant oscillatory frequency can eventually be achieved. We note that for simplicity, we assume no frictional effect once the C_{60} fullerene is oscillating linearly at r_0. For the case of the C_{60}@(10,10), since $r_0 < r_s = 0.08$ Å, we can approximate r_s and r_0 by zero, and Eq. (2.18) reduces to

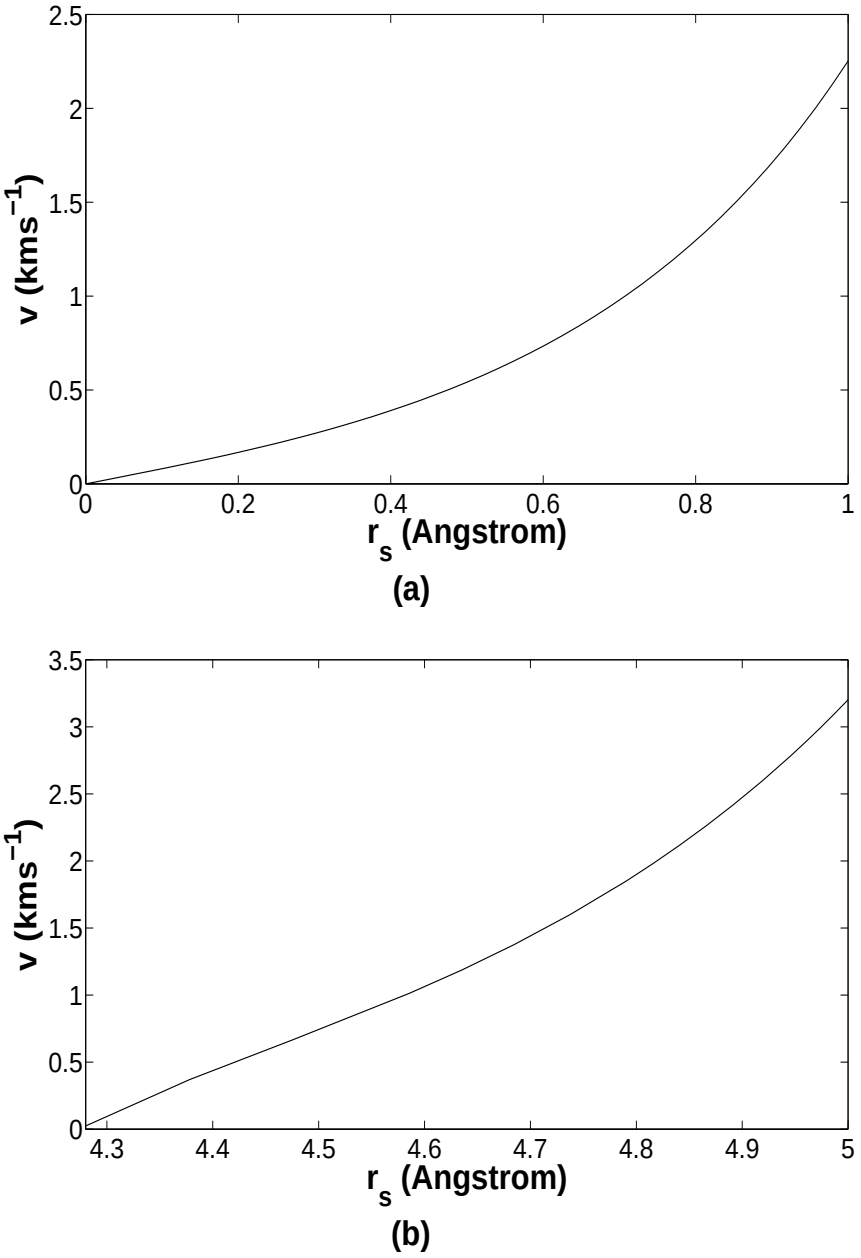

Figure 2.10: Circumferential velocity v of C_{60} at preferred radius r_s from the axis of (a) (10,10) and (b) (16,16) carbon nanotube.

$$F_f = -4\pi a b^2 c \left\{ \frac{a^2 + b^2}{(a^2 - b^2)^4} \right\} v, \tag{2.24}$$

where v denotes the initial circumferential velocity of the C_{60} fullerene. Upon utilizing $F_f = m(dv/dt)$, where m denotes the mass of an isolated C_{60} fullerene and that the final circumferential velocity is zero, we can approximate dv/dt by $-v/t^*$

provided that t^* is small, and Eq. (2.24) can be recast to become

$$t^* = \left(\frac{m}{4\pi ab^2c}\right)\left[\frac{(a^2-b^2)^4}{a^2+b^2}\right]. \tag{2.25}$$

If we substitute all the required parameters into Eq. (2.25), we obtain $t^* = 4$ ps, which confirms our assumption and gives excellent agreement with the molecular dynamics simulation results obtained by both Tuzun et al. [156] and Haibin et al. [52]. According to Tuzun et al. [156], the period of the C_{60}@(10,10) oscillator is given by 20 ps, which is equivalent to the oscillatory frequency of 50 GHz, and the initial translational velocity v_{t_i} of the C_{60} is also given by 480 ms^{-1}. Hence, we can calculate the length of the nanotube L as 10 nm. The equation of motion of the translational velocity v_t can be written as

$$\frac{dv_t}{dt} = -\frac{4\pi ab^2c}{m}\left[\frac{a^2+b^2}{(a^2-b^2)^4}\right]v_t = -\frac{1}{t^*}v_t. \tag{2.26}$$

Upon integrating Eq. (2.26) from $t = 0$ to t^* s and denoting the final translational velocity of the C_{60} fullerene by v_{t_f}, we may deduce

$$v_{t_f} = \exp(\ln v_{t_i} - 1), \tag{2.27}$$

from which we obtain $v_{t_f} = 177$ ms^{-1}. Hence the resultant oscillatory frequency can be calculated as 17 GHz, which is 33 GHz less than the ideal case where the C_{60} fullerene oscillates in the axial direction along the (10,10) nanotube. The dramatic reduction in the oscillatory frequency occurs as a consequence of energy losses due to the unstable spiral motion resulting from the sudden increase in r from the axial center. The case of the C_{60}@(16,16) can be examined in an analogous way. However, we can no longer assume that the equilibrium location is situated on the axis, which

gives rise to a more complicated mathematical derivation. Such a derivation can only be resolved by utilizing a numerical method to determine r_s first from Eq. (2.15) and then substituting $r_s = r$ into Eq. (2.24) and the rest of the arguments are equivalent to that for C_{60}@(10,10). Since currently no molecular dynamics simulation results exist for C_{60}@(16,16), we might also find it difficult to determine the frictional coefficient for such an oscillatory system.

2.1.5 Conclusion

In this section, we investigate the dynamics of a carbon atom or a C_{60} fullerene inside a carbon nanotube. We assume that the carbon atoms are uniformly distributed over the surface of the carbon nanotube so that the molecular potential energy can be approximated by the continuous approach, and from which we can derive the equations of motion utilizing Newton's second law. We also assume that the preferred radial position r_s of the carbon atom and the C_{60} fullerene is defined when the net radial force, which comprises both the van der Waals forces and centrifugal forces is zero. We determine the oscillatory motion of a carbon atom inside various nanotubes; and in particular spiral-like motion is found when the atom is oscillating inside sufficiently large nanotubes due to the thermal and curvature effects. Upon incorporating the frictional effect into the C_{60}-nanotube oscillators, we find that the spiral-like motion of the C_{60} fullerene oscillating inside the nanotube is induced but it is not stable, which allows us to determine the resultant oscillatory frequency of such oscillators. In future work, we aim to extend the study presented here to consider a collection of several atoms or molecules flowing inside the nanotube.

2.2 Magnetic field driven nano tippe top

The discovery of fullerenes [84] and carbon nanotubes [66] has led to numerous studies on their properties and their various potential applications in nano devices. In this section, we focus on the mechanics of a nanoscale tippe top comprising a C_{60}

fullerene which for example might be joined to a carbon nanotube and is spinning on a graphene sheet or inside a large single-walled carbon nanotube. We assume that the nano tippe top is at the equilibrium configuration either on the graphene sheet or inside the outer carbon nanotube and that the spinning occurs due to the application of an external magnetic field. We refer to this structure as a nano tippe top or simply as a nano top. We note that in the case of the top spinning inside a nanotube, that although the effect of the outer carbon nanotube is not directly incorporated into our calculations, we have in mind that the outer carbon nanotube acts as a barrier between the nano top and the external environment.

The flip over of the classical tippe top has attracted much attention due to its "apparent" violation of the principle of conservation of energy during the top's inversion (i.e. the rise in its center of mass results in the sudden increase in its potential energy but apparently no gain in other energies) as well as the lack of a complete mathematical description of this inversion phenomenon in the early discovery [18, 65, 113, 91, 38, 51, 16]. However, it is until Cohen [25] who provides a comprehensive analysis and a satisfactory numerical study on the tippe top showing the inversion of the top when the precession angle is π. In particular, he views the tippe top as an eccentric sphere, for which its center of mass is different from its geometric center, and he incorporates Coulomb friction into his model at the contact point to describe the tippe top's motion (reduction in rotational kinetic energy of the top due to the frictional effect to offset the increase in the potential energy of the top during the inversion). In our case, the nano tippe top (this eccentric sphere) can be manufactured either by creating the top with two different mass densities or by puncturing the sphere and inserting a stem. At the nanoscale, the latter method may be achieved by introducing a defect on the surface of a C_{60} fullerene and then joining to this defect a small segment of a carbon nanotube. We refer the reader to Nasibulin et al. [105] for the possible creation of such nano tippe tops.

Classically, the friction between the eccentric sphere and the relatively rough surface plays a vital role for the top's inversion. Assuming the conservation of the

total energy, the sudden gain in the potential energy during the inversion results from the loss in the top's rotational kinetic energy, which can also be observed from the reduction in the spinning of the inverted top. Furthermore, since gravity and the normal force act solely along the axis fixed in space and provide zero torque to the top, the friction, which acts offset from the space-fixed axis and against the rotational motion of the top, is therefore the only source providing an external torque to slow the spinning of the top down [18]. In addition, Ueda et al. [157] show theoretically that the top's initial spinning and the ratio of the top's two different principal moments of inertia at the center of mass play an important role to determine the top's inversion. For example, the flip over phenomenon can only occur when its initial spinning is above a certain threshold.

At the nanoscale, since frictional force is ultra-low [41, 80], our numerical results show that the friction itself is insufficient to make the nano tippe top precessing about the fixed-body axis. Therefore, we introduce a sufficiently large retarding magnetic force at the contact point to act analogously to the effect of friction. However, we find numerically that instead of flipping over, the nano top prefers to spin in a stable lying down configuration, which suggests that the effect of gravity is negligible at the nanoscale. In particular, the nano top behaves more like a hard-boiled egg spinning on a rough surface [103].

As mentioned above, to induce the spinning effect of a nano top we introduce a retarding magnetic force at the contact point between the C_{60} fullerene and the carbon nanotube's wall. We find from Wood et al. [170] who experimentally produce ferromagnetic fullerenes C_{60} that the magnetically strongest fullerenes are formed at 800 K with the magnetic moment per molecule of $0.38\mu_B$, where μ_B denotes the Bohr magneton constant. This result indicates that we can initiate the spinning of a fullerene in a preferred direction by applying an external magnetic field to the center of the fullerene and similarly at the contact point for generating the retarding magnetic force.

In the following sub-section, we briefly state vector equations which are utilized

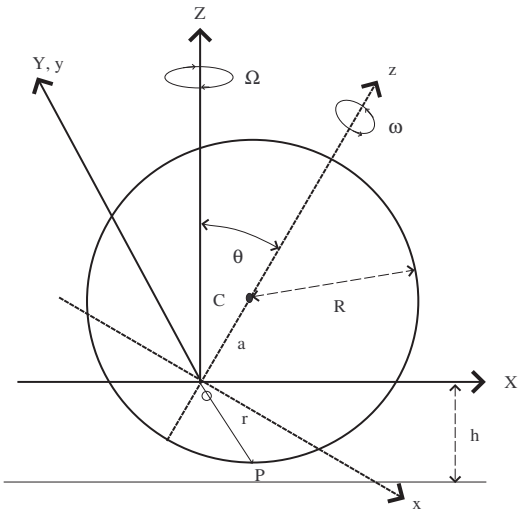

Figure 2.11: Schematic of nano tippe top.

to describe motion of a tippe top. We note that explicit forms of these equations are given in Appendix 6.1. In sub-section 2.2.2, we provide numerical results for a nano tippe top, which is driven by a constant magnetic force in both x- and y-directions. We verify our numerical schemes by examining the classical tippe top, as presented in Appendix 6.1. Conclusion of the section is given in sub-section 2.2.3. In Appendix 6.2, we utilize the basic equations as given in Appendix 6.1 to study the stability for certain configurations of a nano tippe top and in particular Appendix 6.3 considers the compatibility between our numerical results and asymptotic expansions when the nano top is in the lying position. Finally, while sub-section 2.2.2 considers $H_x = H_y = H$, in Appendix 6.4 we assume a magnetic force which is applied only in the y-direction and only for a finite time t_0.

2.2.1 Equations of motion

In this sub-section, we state the equations of motion for a nano tippe top, which is schematically illustrated in Fig. 2.11. Owing to the axial symmetry of the density of the nano top and its eccentric structure, we assume that the center of mass O is at a distance a away from its geometric center C. We denote coordinates (X, Y, Z) as the space-fixed frame of the top while $(x,\ y,\ z)$ as the body-fixed frame. We

adopt (ϕ, θ, ψ) as the usual Euler angles relative to the space-fixed frame so that $\Omega = \dot{\phi}$. In addition, we choose the axes OY and Oy such that they coincide for all time. Therefore, the space-fixed frame and the body-fixed frame are different only through the rotation of the nutation angle θ. Furthermore, we suppose that the spinning about the space-fixed frame is $\boldsymbol{\Omega}(t) = (0, 0, \Omega)$ and the spinning about the body-fixed frame as ω where Ω denotes angular frequency about the Z-axis, and the nano top is assumed to be initially spinning about the axis Oz with an angular frequency ω. The distance between the surface and the center of mass is $h(\theta) = R - a\cos\theta$ and the position vector OP is $\boldsymbol{r} = (a\sin\theta, 0, -h(\theta))$. From the above quantities, the total angular velocity $\boldsymbol{n}$ and the total angular momentum $\boldsymbol{L}$ of the nano tippe top's system in the body-fixed frame are given respectively by

$$\begin{aligned}
\boldsymbol{n} &= ((\omega - \Omega\cos\theta)\sin\theta, \dot{\theta}, \Omega\sin^2\theta + \omega\cos\theta), \\
\boldsymbol{L} &= ((C\omega - A\Omega\cos\theta)\sin\theta, A\dot{\theta}, A\Omega\sin^2\theta + C\omega\cos\theta),
\end{aligned} \tag{2.28}$$

where (A, A, C) denote the principal moments of inertia at the center of mass O. In addition, the translational velocity at the contact point P with respect to O can be written as $\boldsymbol{v}_{r_P} = \boldsymbol{n} \times \boldsymbol{r}$ and hence the sliding velocity at P is given by $\boldsymbol{v}_p = \dot{\boldsymbol{X}} + \boldsymbol{v}_{r_P}$, where $\dot{\boldsymbol{X}} = (u_x, u_y, u_z)$ denotes the velocity of the center of mass of the nano top. The equations of motion of the nano top can then be determined for the six degrees of freedom motion comprising three rotational equations derived from the Euler equations and three translational equations derived from Newton second law, namely

$$\begin{aligned}
\frac{\partial \boldsymbol{L}}{\partial t} + \boldsymbol{\Omega} \times \boldsymbol{L} &= \boldsymbol{r} \times (\boldsymbol{N} + \boldsymbol{F}), \\
m(\ddot{\boldsymbol{X}} + \boldsymbol{\Omega} \times \dot{\boldsymbol{X}}) &= \boldsymbol{N} + \boldsymbol{F} + \boldsymbol{W},
\end{aligned} \tag{2.29}$$

where m, $\boldsymbol{N}$, $\boldsymbol{F}$, $\boldsymbol{W}$ denote the mass, the normal force, the retarding force and the weight of the nano top, respectively. Explicit forms of these equations of motion

are given in Appendix A of Ueda et al. [157] and they are also briefly stated in the appendix of this thesis. Next, we determine a suitable form of the frictional force for the proposed nano tippe top system. Various theoretical [33, 32] and molecular dynamics studies [42, 142] suggest that under the low velocity limit, the frictional force between two molecules is linearly proportional to their relative velocity. In addition, Heo et al. [58] propose that the frictional force between a fullerene and a carbon nanotube is also proportional to the fullerene's normal reaction, namely $|\boldsymbol{F}_f| = \mu N$. Further, molecular dynamics simulation of Heo et al. [58] show that the frictional coefficients for various nanostructures, namely single-walled carbon nanotubes, nanopeapods and double walled carbon nanotubes, under a low pressure regime, are essentially the same, i.e. $\mu = 0.13$. Here, we also incorporate a retarding magnetic force to the model and we propose that the total retarding force of the nano top inside the carbon nanotube is given by

$$\boldsymbol{F} = -\boldsymbol{F}_f - \boldsymbol{H}(B) = -\frac{0.13N}{\mid \boldsymbol{v}_P \mid}\boldsymbol{v}_P - \boldsymbol{H}(B), \tag{2.30}$$

where $\boldsymbol{H}(B)$ denotes the retarding magnetic force acting at P and $\boldsymbol{v}_P$ is the velocity at the contact point P.

2.2.2 Numerical results and discussion

A fourth order Runge-Kutta method [20] is adopted here to numerically solve this system of six ordinary differential equations, namely Eq. (2.29) (the full algorithm of the fourth order Runge-Kutta method is shown step by step by Burden and Faires [20] on pp. 278-279. We can also utilize the prescribed command, e.g. ode45 built internally by Matlab numerical solver to implement such algorithm). Ueda et al. [157] show that in macro scale the top's inversion is strongly dependent on the ratio of two principal moments of inertia at the center of mass. Therefore, we check whether the inversion of the nano top is possible by running the numerical scheme with various values of $C/A \in (0, 1)$, but we find that this ratio does not affect our

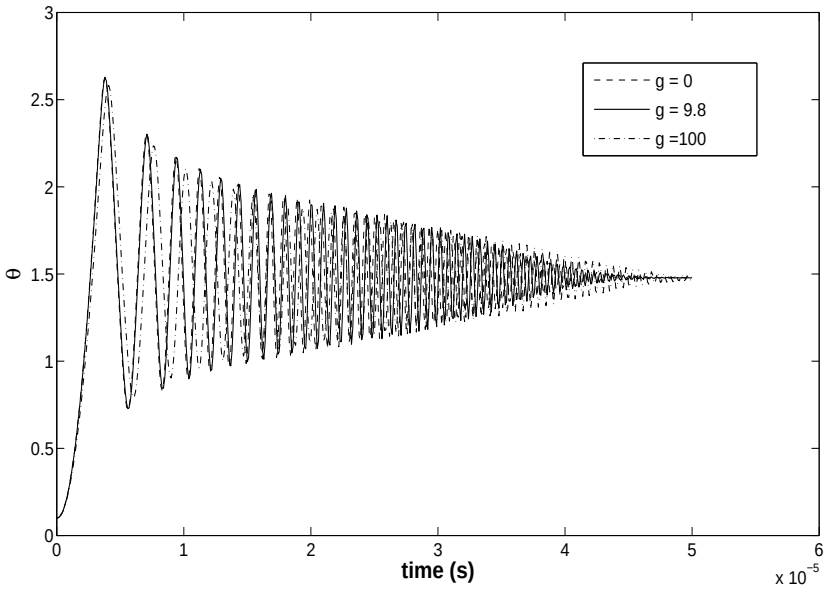

Figure 2.12: Nutation angle θ for $g = 0$, 9.8 and 100 ms^{-2} during precession.

numerical results. However, in all cases a sufficiently large initial spinning of the nano top is required. Therefore, we choose the following physical parameters for the numerical iteration: $R = 3.55$ Å, $a = 0.1R$, $m = 1.196 \times 10^{-24}$ kg, $A = (2/3)mR^2$, $C = 0.5A$ and $H_x = H_y = 0.1$ zN with the following initial conditions: $\theta = 0.1$, $\Omega = 0$, $\dot{\theta} = 0$, $\omega = 100$ and $\dot{\boldsymbol{X}} = (0, 0, 0)$. These initial conditions can be interpreted that we release the nano top with its initially spinning (100 Hz) about the z-axis, having 0.1 rad deflection from the Z-axis and zero sliding velocity at the contact point P. We utilize 500 grid points to carry out the numerical iteration and the numerical results obtained for θ, Ω and ω are illustrated in Figs. 2.12, 2.13 and 2.14, respectively.

Under the total retarding force, which comprises both the frictional and the magnetic forces at the point of contact P, Fig. 2.12 shows that the nano top precesses from its standing up configuration ($\theta = 0$) during the first 5 μs but asymptotically approaches the lying down configuration ($\theta = \pi/2$) after 50 μs with the decrease in its oscillating amplitude. During the precession, as shown in Fig. 2.13, the angular frequency Ω about the Z-axis increases dramatically in the first micro second indicating the sudden drop down of the nano top but oscillating around zero while the

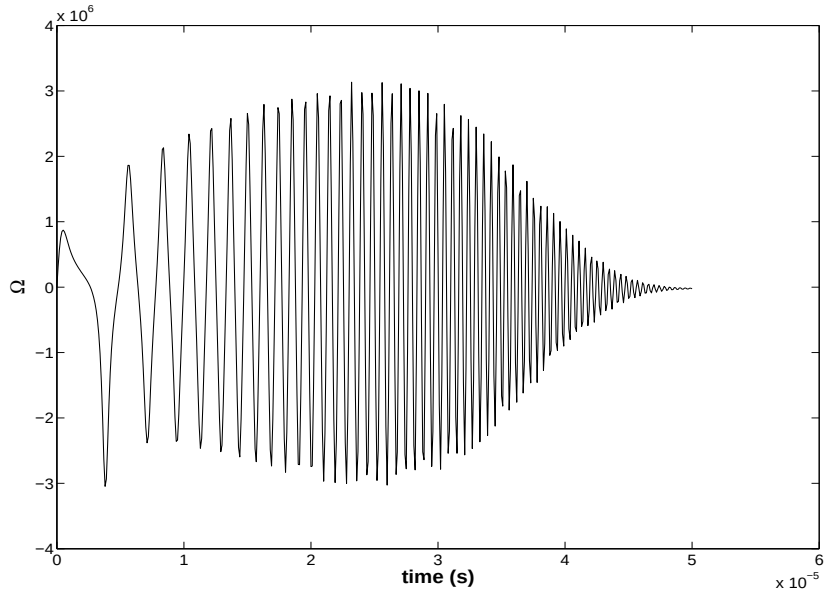

Figure 2.13: Angular frequency Ω about the Z-axis during precession.

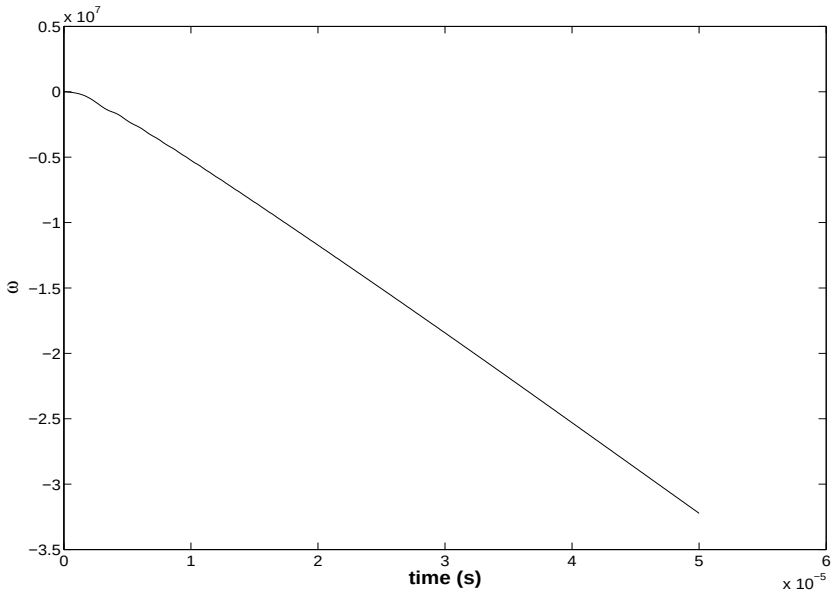

Figure 2.14: Angular frequency ω about the z-axis during precession.

nano top has laid down. On the other hand, from Fig. 2.14 the angular frequency ω about the z-axis also drops from its initial positive value to zero and then monotonically increases in magnitude to 30 MHz but in the opposite direction with respect to the direction of the initial spinning. This implies that the nano top reverses its spinning direction and gains its spinning speed due to the opposite motion and the energy gained from the retarding magnetic force respectively. We also note that

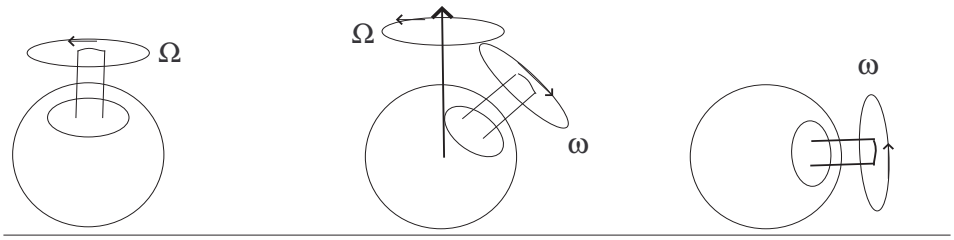

Figure 2.15: Precession of nano tippe top.

the center of mass of the nano top moves in the X, Y-directions only resulting in sliding friction but remains intact in the Z-direction (see Figs. 6.4 and 6.5). The whole precession process is illustrated in Fig. 2.15. Unlike the classical tippe top, we observe no flip over phenomenon in the nano top's precession. This no inversion phenomenon arises from the fact that the gravitational force is negligibly small at the nanoscale. As confirmed by Fig. 2.12, the precession is not effected by the gravitational force since the numerical results for $g = 0$ and 9.8 ms^{-2} almost coincide with each other, and the same behaviour is obtained for $g = 100$ ms^{-2}.

Once the nano top is spinning about the lying down axis, it is important to determine a possible way for which the nano top can retract to its initial standing up position. We find that the nano top will retract smoothly back to its standing up axis upon applying a magnetic force of the same magnitude but in the opposite direction to the previous retarding magnetic force and the numerical solution for θ is shown in Fig. 2.16.

Accordingly, by adjusting the magnetic field, we can manually control the nano top's switching between the standing up and the lying down states and hence it can be utilized as a nano-computing memory device. Moreover, the main advantages of utilizing the nano tops as a memory device are that it possesses a remarkably short relaxation time (≈ 50 μs) resulting in a higher computational speed, and it is small in size and hence provides a larger memory capacitance. Most importantly, it is simpler to control as compared with the electron-spin quantum memories. Finally, the integration of the self-assembled hybrid nanostructure known as nanopeapods and the ideas of nano tippe top developed here may lead to practical computing

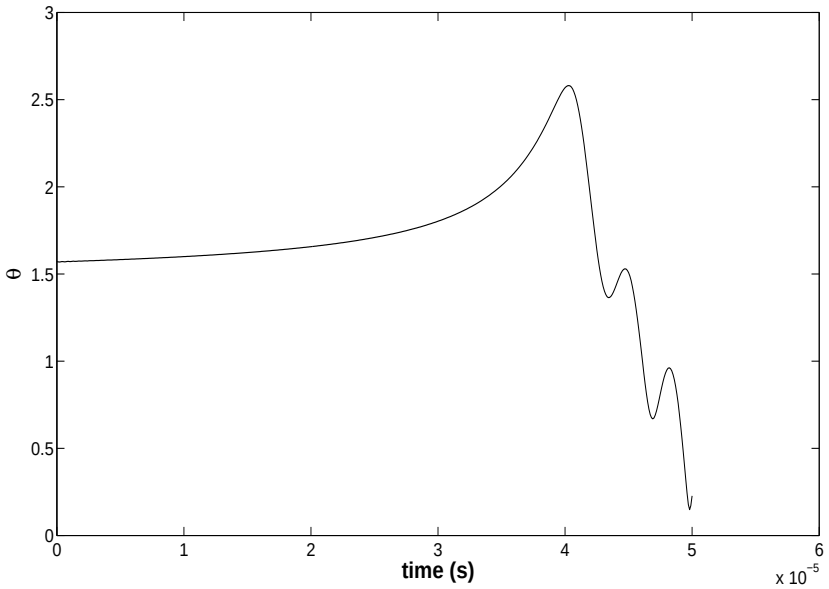

Figure 2.16: Nutation angle θ after applying the reversed retarding magnetic field at P.

memory devices, which currently require large numbers of bit handling.

2.2.3 Conclusion

A nano tippe top formed from a C_{60} fullerene and spinning either on a graphene sheet or inside a carbon nanotube is investigated as a possible candidate for a computing memory device. The equations of motion for such a nano top are described and we find that while the retarding magnetic force makes the nano top precess, it does not flip over as in the classical tippe top, but due to the fact that gravity is negligible at the nanoscale, it adopts a lying down position. In addition, while the nano top is in the lying down position, if we apply the magnetic force which is of the same magnitude but in the opposite direction to the previous retarding magnetic force, then the nano top will return to its standing up position. Hence, the standing up and lying down configurations of the nano top might be considered as two bit states, which gives rise to their potential utilization as a future memory device.

2.3 Mechanics of nanoscale orbiting systems

Here, we investigate orbiting phenomenon at the nanoscale. In particular, we consider an atom and a C_{60} fullerene orbiting around the outside a carbon nanotube and also a C_{60} fullerene orbiting around a C_{1500} molecule. The van der Waals interaction energy is modelled utilizing the 6-12 Lennard-Jones potential and a continuous approach, in which we assume a uniform distribution of carbon atoms on the surfaces of the carbon nanotube and the fullerene. We find that the interacting molecules move with respect to each other under the influence of their mutual central force. While their loci cannot be integrated in terms of well-known special functions, they can be determined numerically. Some analytical and perturbation solutions for special cases can be obtained if it is assumed that attractive forces dominate and that the total energy of both the atom and the fullerene are small, then one can obtain analytical results, which provide some insight into suitable forms of the loci. Finally, the circular radii of orbits are estimated by finding the minimum energy configuration of the effective potential energies, and a stability analysis is employed to ensure the stability of the circular radii, which is of practical importance in creating certain nanodevices. For all cases, the circular orbiting frequencies reach the gigahertz range. We comment that this thesis ignores any thermal fluctuations arising from the environment. If such effects are incorporated, the orbiting motion of these systems may be critically disrupted and the orbiting phenomenon might not be observed.

The section is structured as follows. In the following sub-section, we give the basic equations of motion for a two-body problem. In sub-sections 2.3.2 to 2.3.7, an atom–carbon nanotube system, a fullerene–carbon nanotube system and a fullerene–fullerene system are examined, respectively. For all cases, the classification of their loci, in terms of both numerical and analytical investigations is given, and their circular orbiting frequencies are provided.

2.3.1 Equations of motion

In this sub-section, a brief description of the equations of motion for a two-body problem is presented. A more detailed derivation and explanation can be found in many classical mechanics graduate textbooks, such as [49]. For a system of two objects, the connecting potential energy $V(\boldsymbol{r})$ depends only on the relative displacement between the two objects $\boldsymbol{r} = \boldsymbol{r_2} - \boldsymbol{r_1}$, where $\boldsymbol{r_1}$ and $\boldsymbol{r_2}$ denote the position vectors of the two masses M_1 and M_2 relative to their center of mass respectively (it is essential for a central force problem that the potential energy between two bodies depends only on $\boldsymbol{r}$). Thus, let $\boldsymbol{P}$ denote the position vector of the center of mass and the Lagrangian L for the two-body problem is defined by

$$L = T(\dot{\boldsymbol{P}}, \dot{\boldsymbol{r}}) - V(\boldsymbol{r}), \tag{2.31}$$

where T and V denote the kinetic and the potential energies respectively. The total kinetic energy T can be expressed as the sum of the kinetic energy owing to the motion of the center of mass and the kinetic energy owing to the motion about the center of mass. That is,

$$T = \frac{1}{2}M\dot{\boldsymbol{P}}^2 + \frac{1}{2}M_1\dot{\boldsymbol{r_1}}^2 + \frac{1}{2}M_2\dot{\boldsymbol{r_2}}^2, \tag{2.32}$$

where $M = M_1 + M_2$ is the total mass of the two-body system. The two position vectors can then be related to the relative displacement vector $\boldsymbol{r}$ by

$$\boldsymbol{r_1} = -\frac{M_2}{M_1 + M_2}\boldsymbol{r}, \qquad \boldsymbol{r_2} = \frac{M_1}{M_1 + M_2}\boldsymbol{r}, \tag{2.33}$$

which upon substituting Eq. (2.33) and Eq. (2.32) into Eq. (2.31), the Lagrangian can be rewritten as

$$L = \frac{1}{2}M\dot{\boldsymbol{P}}^{\boldsymbol{2}} + \frac{1}{2}\mu\dot{\boldsymbol{r}}^{\boldsymbol{2}} - V(\boldsymbol{r}), \tag{2.34}$$

where $\mu = M_1 M_2/(M_1+M_2)$ is called the reduced mass of the system. Therefore, the two-body problems can always be reduced to the reduced mass μ, moving about the center of mass of the system as is incorporated in Eq. (2.34). If we assume $V(\boldsymbol{r}) = V(r)$ and express the Lagrangian in terms of polar coordinates, then Eq. (2.34) becomes

$$L = \frac{1}{2}\mu(\dot{r}^2 + r^2\dot{\theta}^2) - V(r), \tag{2.35}$$

and the angular momentum of the system is obtained from L by $p = \partial L/\partial\dot{\theta} = \mu r^2\dot{\theta}$. Without any external torque, it is known that the angular momentum of the system is conserved, so that

$$h = \mu r^2\dot{\theta}, \tag{2.36}$$

where h denotes an arbitrary constant. Finally, the total energy E is given by

$$E = \frac{1}{2}\mu(\dot{r}^2 + r^2\dot{\theta}^2) + V(r) = \frac{1}{2}\mu\dot{r}^2 + \frac{h^2}{2\mu r^2} + V(r) = \frac{1}{2}\mu\dot{r}^2 + V_{eff}(r), \tag{2.37}$$

where $V_{eff}(r) = h^2/2\mu r^2 + V(r)$ denotes the effective potential energy, which comprises both the angular kinetic energy $h^2/2\mu r^2$ and the potential energy $V(r)$. A circular orbit of radius R can be computed by finding the minimum energy configuration of V_{eff}.

2.3.2 Atom–carbon nanotube system

In this sub-section, we investigate a single carbon atom orbiting around a thin infinitely long carbon nanotube, which is approximated by a line. Since the interactions between the molecules occur at a sufficiently large distance, it is reasonable to model the non-bonded intermolecular interactions by the van der Waals forces utilizing the 6-12 Lennard-Jones potential. We adopt the continuous approach and

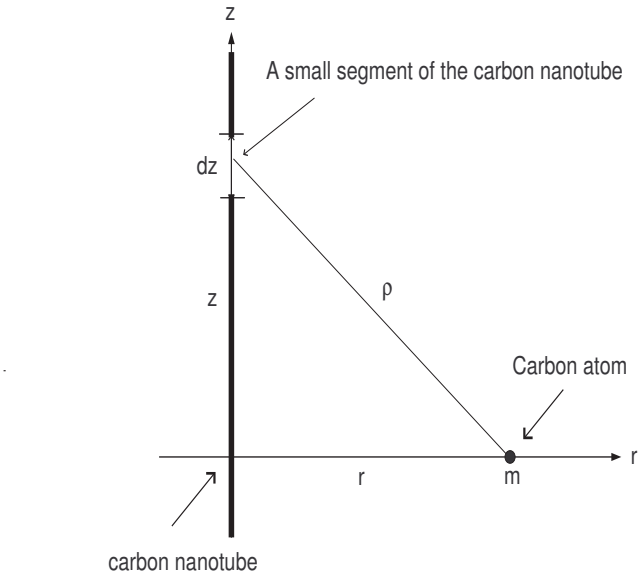

Figure 2.17: Atom–carbon nanotube system.

the van der Waals interaction energy of this system is given by

$$V(\rho) = n_t \int_{-\infty}^{\infty} \left(\frac{-A}{\rho^6} + \frac{B}{\rho^{12}} \right) dz, \tag{2.38}$$

where A and B are the attractive and repulsive constants, respectively, ρ denotes the distance between the orbiting atom and an arbitrary atom on the carbon nanotube, and n_t is the mean surface density of atoms on the carbon nanotube. The numerical values of the constants utilized throughout this thesis are presented in Table 2.1. From Fig. 2.17, we have $\rho^2 = z^2 + r^2$ so that the molecular potential energy $V(r)$ can be expressed as

$$V(r) = n_t \int_{-\infty}^{\infty} \left\{ \frac{-A}{(z^2 + r^2)^3} + \frac{B}{(z^2 + r^2)^6} \right\} dz, \tag{2.39}$$

which upon making the substitution $z = r \tan\theta$, Eq. (2.39) becomes

$$V(r) = n_t \int_{-\pi/2}^{\pi/2} \left\{ -\frac{A}{r^5} \cos^4\theta + \frac{B}{r^{11}} \cos^{10}\theta \right\} d\theta = -\frac{A'}{r^5} + \frac{B'}{r^{11}}, \tag{2.40}$$

where $A' = 3\pi n_t A/8 = 7.8$ eVÅ^5 and $B' = 63\pi n_t B/256 = 8547$ eVÅ^{11} are the modified attractive and repulsive constants respectively. This potential energy is

illustrated graphically in Fig. 2.18. According to Eq. (2.37), the effective potential energy $V_{eff}(r)$ is given by

$$V_{eff}(r) = \frac{C'}{r^2} - \frac{A'}{r^5} + \frac{B'}{r^{11}}, \tag{2.41}$$

where $C' = h^2/2m_a$ and m_a denotes the mass of a carbon atom. The extra term C'/r^2 corresponds to the atom's angular kinetic energy. The classification of the atom's loci can then be obtained by analyzing the total energy of the system E, which from Eqs. (2.37) and (2.41) becomes

$$E = \frac{1}{2}m_a\dot{r}^2 + \left(\frac{C'}{r^2} - \frac{A'}{r^5} + \frac{B'}{r^{11}}\right), \tag{2.42}$$

and upon changing the coordinate system from t to θ by utilizing Eq. (2.36), we obtain

$$d\theta = \frac{\sqrt{C'}dr}{r^2\sqrt{E + A'/r^5 - B'/r^{11} - C'/r^2}}. \tag{2.43}$$

We can simplify the above equation by making the substitution $u = r^{-1}$, and by integrating both sides of Eq. (2.43) to yield

$$\theta - \theta_0 = -\int \frac{\sqrt{C'}du}{\sqrt{E - B'u^{11} + A'u^5 - C'u^2}}. \tag{2.44}$$

Unlike the classical two-body problem, for which the polynomial under the square root is a quadratic, in this case the polynomial under the square root has a maximum degree of 11, which makes the integration much harder to effect in terms of well-known special functions. Thus, some numerical and perturbation methods are presented in order to gain some physical insight into this problem. The atom's orbiting circular radius can be readily computed by finding the minimum energy configuration of the effective potential energy. Since, there is a one-to-one relationship between its circular orbiting radius and its circular orbiting frequency (2.45), in the following sub-section the circular orbiting frequency of this system is estimated

and it is found to be operating in the gigahertz range.

2.3.3 Circular orbiting frequency of atom–carbon nanotube system

In this sub-section, the circular orbiting frequency of an atom orbiting around a carbon nanotube is estimated by examining the minimum energy configuration of the effective potential energy, since it can be shown from classical mechanics that the minimum energy configuration of Eq. (2.41) corresponds to a circular orbit of the atom. By solving $V'_{eff}(r) = 0$, the circular angular velocity, ω, is given by

$$\omega^2 = \frac{5A'}{m_a R^7} - \frac{11B'}{m_a R^{13}}, \tag{2.45}$$

where R is the atom's circular orbiting radius. In order to obtain Eq. (2.45), the conservation of angular momentum of the system is utilized. Note that Eq. (2.45) by itself is not sufficient to determinate the circular orbiting frequency of the atom. However, the stability of a nearly circular orbit and the boundness of the atom's locus at R have to be satisfied for the atom to keep orbiting in its circular orbit. To determine the stability of the atom's circular orbit, differentiating both sides of Eq. (2.42) with respect to t, yields

$$m_a \ddot{r} + \left(-\frac{2C'}{r^3} + \frac{5A'}{r^6} - \frac{11B'}{r^{12}} \right) = 0, \tag{2.46}$$

so that upon making the substitution $u = 1/r$, we get

$$\frac{d^2u}{d\theta^2} - \frac{m_a}{h^2}(5A'u^4 - 11B'u^{10} - 2C'u) = 0. \tag{2.47}$$

Now we consider the substitution $u = 1/R + \varepsilon$, where ε is an infinitesimal quantity, so that Eq. (2.47) gives

$$\frac{d^2\varepsilon}{d\theta^2} - \frac{m_a}{h^2}\left(\frac{20A'}{R^3} - \frac{110B'}{R^9} - 2C' \right)\varepsilon = 0. \tag{2.48}$$

For ε to be convergent, it is obvious that the following inequality has to be satisfied $2C'R^9 - 20A'R^6 + 110B' > 0$, where from the definition of C' and the conservation of angular momentum of the system, we find $R < (33B'/5A')^{1/6}$. In addition, the boundness of the atom at $r = R$, i.e. $V_{eff} < 0$ has to be verified. From Eq. (2.41), this gives the following condition

$$\frac{C'}{R^2} - \frac{A'}{R^5} + \frac{B'}{R^{11}} < 0 \quad \Rightarrow \quad R < \left(\frac{3B'}{A'}\right)^{1/6}. \tag{2.49}$$

Therefore, R must satisfy the following criteria for the atom orbiting in its stable and bounded circular orbit

$$R < \min\left\{\left(\frac{33B'}{5A'}\right)^{1/6}, \left(\frac{3B'}{A'}\right)^{1/6}\right\} = \left(\frac{3B'}{A'}\right)^{1/6} \approx 3.8 \text{ Å}. \tag{2.50}$$

Upon taking $R = 3.8$ Å, the circular orbiting frequency f can be estimated to be $f = 29$ GHz by utilizing Eq. (2.45). Given the circular orbiting frequency, the angular kinetic energy can be easily calculated as $0.074/r^2$ eV by fixing the angular momentum of the system $h = 5.4 \times 10^{-14}$ kgm^{2}s^{-1}, and the effective potential energy V_{eff} can then be computed by incorporating the angular kinetic energy. For comparison, we plot the angular kinetic energy, the molecular potential energy and the effective potential energy, as shown in Fig. 2.18. The effective potential energy of this system is found to resemble classical planetary motion and all possible classifications of the atom's loci can be explained in terms of its total energy. Note that the circular orbiting radius R, estimated in Eq. (2.50), agrees with the value of R suggested from Fig. 2.18. For an atom to stay orbiting in its circular orbit, the total energy must be equal to the minimum energy configuration of the effective potential energy V_{eff}, namely

$$E = \frac{B'}{R^{11}} - \frac{A'}{R^5} - \frac{C'}{R^2} \approx -1.14 \text{ meV}. \tag{2.51}$$

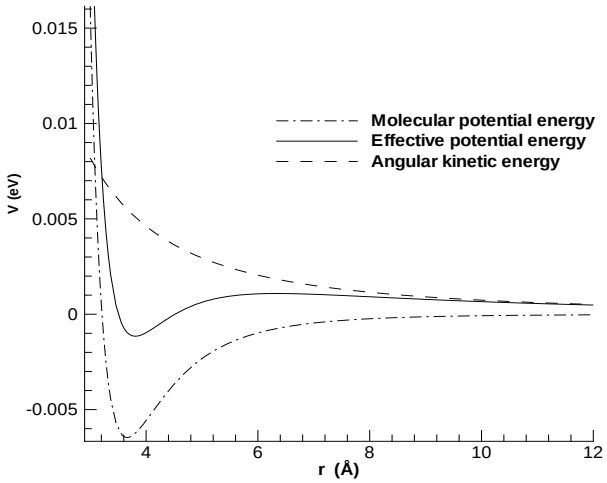

Figure 2.18: Comparison between angular kinetic energy, molecular potential energy and effective potential energy for atom–carbon nanotube system.

2.3.4 Numerical locus for atom–carbon nanotube system

In this sub-section, numerical solutions for the loci of Eq. (2.44) is determined. For a given value of angular momentum of the system h, we examine the conditions for which the atom's orbit is either bounded or unbounded. From Eq. (2.44), we have

$$\frac{du}{d\theta} = \pm\frac{\sqrt{E - B'u^{11} + A'u^5 - C'u^2}}{\sqrt{C'}}, \tag{2.52}$$

so that if we discretize a complete revolution into N grid points then a first order numerical scheme, utilizing Euler's method [20], is given by

$$u_{i+1} = u_i \pm \varepsilon\frac{\sqrt{E - B'u_i^{11} + A'u_i^5 - C'u_i^2}}{\sqrt{C'}}, \tag{2.53}$$

where $i \in [1, N]$, $\varepsilon = 2\pi/N$ and N is the total number of grid points. We comment that the Euler's method is sufficiently accurate numerical scheme to be utilized here because of the smooth function on the right hand side of Eq. (2.52). For Eq. (2.53) to have real solutions, $E \geq B'u_i^{11} - A'u_i^5 + C'u_i^2$ is required to be satisfied for all i. In particular, when $E = B'u_0^{11} - A'u_0^5 + C'u_0^2$, $u_{i+1} = u_i$ for all i and this corresponds to a circular orbit. The constant C' is taken to be 0.074 and this numerical scheme

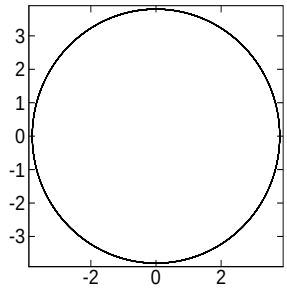

Figure 2.19: Locus for $E = -1.14$ meV with initial position 3.8 Å. Atom is orbiting in its stable circular orbit.

is carried out for different values of the total energy E.

Here, unless otherwise stated, we apply the numerical scheme to 20 revolutions of the orbiting atom, where 100 grid points are utilized. Owing to the feature of the effective potential energy in Fig. 2.18, one dip and one crest are observed, where the crest's tail goes to infinity. Therefore, we consider $E = -1.14$, -0.6, 0 , 0.5 and 1.1 meV, where -1.14 meV is the value of E at the dip of V_{eff}, -0.6 meV is the mid-point between 0 eV and the dip, 0.5 meV is the mid-point between the crest and the zero potential and 1.1 meV is the crest's energy. For a given total energy E, feasible initial positions are determined utilizing the expression $E = (1/2)m_a v^2 + V_{eff}$, for which the velocity is real if and only if $E \geq V_{eff}$. The numerical outcomes are presented below with physical explanations.

Case 1 ($E = -1.14$ meV): In this case (see Fig. 2.19), the only possible initial position r_0 is the atom's own circular orbit, which is equal to $R = 3.8$ Å. All other values of r_0 gives rise to $E < V_{eff}$, which is not physically feasible.

Case 2 ($E = -0.6$ meV): In this case, possible initial positions r_0 lie between 3.58 Å and 4.191 Å, which are determined numerically by solving r from $V_{eff} = -0.6$ meV. An orbit with this total energy is clearly bounded between 3.58 Å and 4.191 Å, which corresponds to an elliptic orbit (where here we define an elliptic orbit to be an orbit that is bounded by two different radii). Therefore, three initial positions, namely 3.6, 3.8 and 4 Å have been examined (see Fig. 2.20). From the figure, it is clear that any carbon atom with this total energy departs from its initial positions

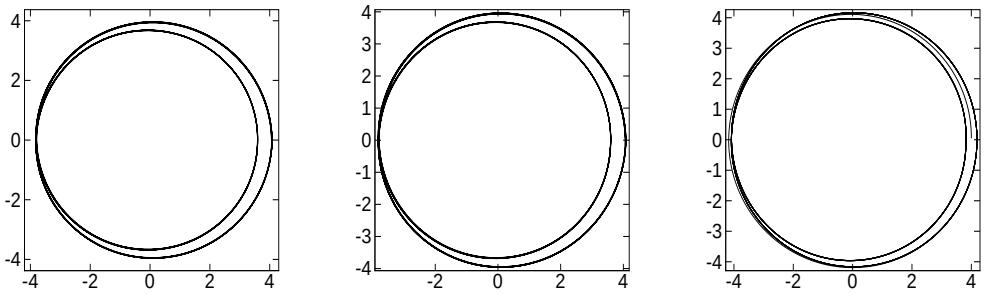

Figure 2.20: Loci for $E = -0.6$ meV with initial positions 3.6 Å, 3.8 Å and 4 Å from left to right respectively. Atom is bounded between 3.58 Å and 4.191 Å for all these initial positions.

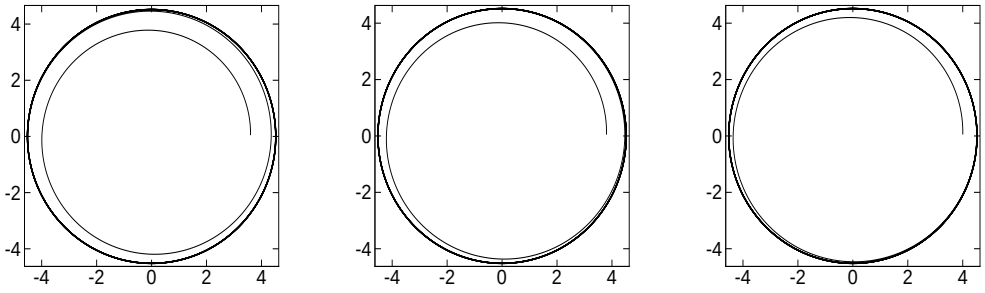

Figure 2.21: Loci for $E = 0$ eV with initial positions 3.6 Å, 3.8 Å and 4 Å from left to right respectively. Atom is swirling away from its bounded loci gradually for all these initial positions.

and then oscillates between the two boundaries $r = 3.58$ Å and $r = 4.191$ Å, which indicates that the molecular potential energy is strong enough to hold the atom in a bounded orbit but weak enough to keep it in a stable circular orbit.

Case 3 ($E = 0$ eV): In this case, r_0 lies between 3.504 Å and 4.509 Å. Unlike the previous cases, orbiting motion involving this energy level are bounded but unstable, owing to the fact that a point at infinity is also an initial accessible point. This form of locus corresponds to a parabolic orbit (where here we define a parabolic orbit to be an orbit such that an atom orbits to the outer-shell radius and then swirls away to infinity gradually). Similar to the second case, 3 initial positions have been chosen to examine, namely 3.6, 3.8 and 4 Å (see Fig. 2.21). It is clear that an atom will move away from its initial positions to the outer boundary $r = 4.509$ Å and then gradually swirls away to infinity.

Case 4 ($E = 0.5$ meV): In this case, r_0 lies between 3.46 Å and 4.86 Å and

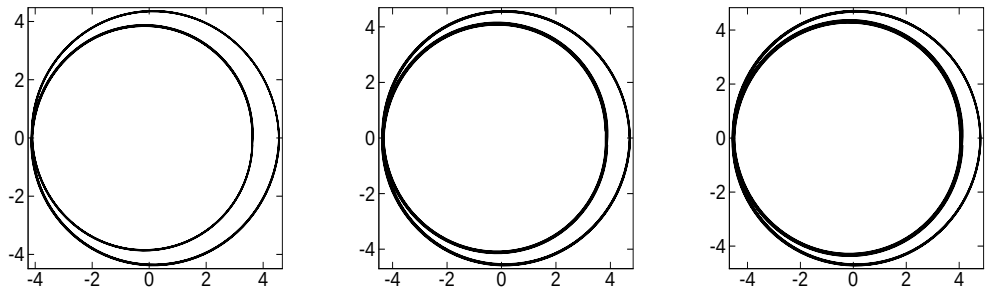

Figure 2.22: Loci for $E = 0.5$ meV with initial positions 3.6 Å, 3.8 Å and 4 Å from left to right respectively. Atom is oscillating between $r = 3.46$ Å and $r = 4.86$ Å for all these initial positions.

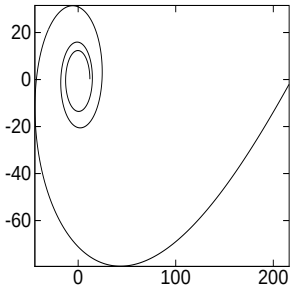

Figure 2.23: Locus for $E = 0.5$ meV with initial position 12 Å. Atom escapes from its initial position to infinity very quickly.

between 11.765 Å and infinity. In particular, the boundness of an atom's orbit depends heavily on its initial positions r_0. If 3.46 Å $\leq r_0 \leq$ 4.86 Å, its locus is elliptic, which is bounded, while if $r_0 \geq 11.765$ Å, its locus is a hyperbolic orbit (where here we define a hyperbolic orbit to be an orbit such that an atom swirls away from the nanotube quickly), which is unbounded. Four initial positions, namely 3.6, 3.8, 4 and 12 Å, have been examined (see Figs. 2.22 and 2.23). For $r_0 = 3.6$, 3.8, 4 Å, an atom departs from its initial positions and then oscillates between the two boundaries $r = 3.46$ Å and $r = 4.86$ Å. However, for $r_0 = 12$ Å, the numerical scheme is unstable, even in the third revolution, which indicates that the molecular potential energy is too weak to hold the atom in a bounded orbit and the atom escapes from its initial position to infinity quickly.

Case 5 ($E = 1.1$ meV): In this case, $r_0 \geq 3.42$ Å and the atom's locus is an hyperbola, which is unbounded. Two initial positions, namely 3.8 and 10 Å, have

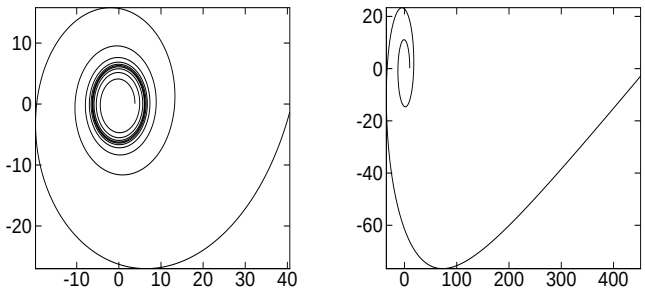

Figure 2.24: Loci for $E = 1.1$ meV with initial positions 3.8 Å and 10 Å from left to right respectively. Atom escapes from its initial position to infinity very quickly for all these initial positions.

been examined (see Fig. 2.24). For $r_0 = 3.8$ Å, the numerical scheme becomes unstable after 10 revolutions, while for $r_0 = 10$ Å the numerical scheme becomes unstable even after two revolutions. Therefore, the atom swirls away from its initial position to infinity for all accessible initial positions.

2.3.5 Perturbation solution for atom–carbon nanotube system

We suppose that an atom is introduced from infinity to a regime, where the attractive forces dominate. This assumption is particularly valid when the 6-12 Lennard-Jones potential is replaced by the hard-sphere repulsive potential given by Hirschfelder et al. [64], namely

$$V(\rho) = \begin{cases} -\frac{D}{\rho^6} & r > \sigma, \\ \infty & r \leq \sigma, \end{cases} \tag{2.54}$$

where D and σ are the modified attractive constant and the collision diameter respectively. At infinity, the total energy is simply equal to the atom's kinetic energy, and this initial energy helps the atom to gain its initial angular momentum orbiting around the carbon nanotube. According to this assumption, the total energy can be represented by $E = E_0 + \varepsilon E_1 + \varepsilon^2 E_2 + \ldots$, where E_0 is approximately zero, and ε is a small positive quantity. Initially, only $E = 0$ is considered, so that Eq. (2.44)

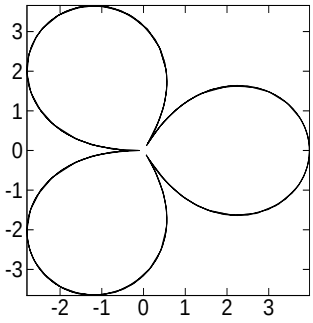

Figure 2.25: Orbiting path described by Eq. (2.56).

gives

$$d\theta = -\sqrt{C'}\frac{du}{\sqrt{A'u^5 - C'u^2}}. \tag{2.55}$$

It is interesting to note that the above equation is integrable and from [149], Eq. (2.55) can be integrated to yield

$$r = \left(\frac{A'}{C'}\right)^{1/3} \cos^{2/3}\left[\frac{3}{2}(\theta - \theta_0)\right], \tag{2.56}$$

where θ_0 is an initial angle and r results from the substitution $u = 1/r$. Eq. (2.56) suggests that without the initial energy, the atom is captured by the Lennard-Jones potential from infinity. After it encounters a repulsive potential barrier, which is located at the center of the nanotube, it bounces back to an amplitude of $(A'/C')^{1/3}$. Once there, the atom is re-captured by the attractive molecular potential energy and this process repeats periodically and endlessly. The graph of Eq. (2.56) is plotted in Fig. 2.25. We note that in Eq. (2.55), the repulsive energy is ignored. If it is included, r will not reach the center of the carbon nanotube as suggested by Eq. (2.56) and Fig. 2.25. Instead, the atom will start to bounce back when it enters the repulsive region of the carbon nanotube.

Now, we construct a small perturbation, i.e. $E = \varepsilon E_1 + O(\varepsilon^2)$, so that from

Eq. (2.44) we find

$$\begin{aligned} d\theta &= -\sqrt{C'}\frac{du}{\sqrt{\varepsilon E_1 + A'u^5 - C'u^2}}, \\ &\approx -\sqrt{\frac{C'}{A'}}\left\{\frac{du}{u\sqrt{u^3-\xi^3}} - \frac{\varepsilon E_1}{2}\frac{du}{u^3(u^3-\xi^3)^{3/2}}\right\}, \end{aligned} \tag{2.57}$$

where $\xi = (C'/A')^{1/3}$. Next, we transform Eq. (2.57) by making $d\theta = \theta_f - \theta_i$ and $du = u_f - u_i$, where θ_i, u_i, θ_f and u_f denote the initial angle, the initial radius, the final angle and the final radius, respectively. After some manipulation, we find that the evolution equation for r, is given by

$$r_f = H(u_i, E_1) r_i, \tag{2.58}$$

where $H(u_i, E_1)$ denotes $\Theta(u_i, E_1)/(\Theta(u_i, E_1) - \delta)$ and the expressions for $\Theta(u_i, E_1)$ and δ are

$$\begin{aligned} \Theta(u_i, E_1) &= \frac{1}{\sqrt{u_i^3 - \xi^3}} - \frac{\varepsilon E_1}{2}\frac{1}{u_i^2(u_i^3-\xi^3)^{3/2}} \\ \delta &= \sqrt{\frac{A'}{C'}}(\theta_f - \theta_i) > 0. \end{aligned} \tag{2.59}$$

We note that when $\Theta(u_i, E_1) = \delta/2$, $|H(u_i, E_1)| = 1$, the atom always stays on the circular orbit. If $|H(u_i, E_1)| > 1$, then the atom moves away from the carbon nanotube, while if $|H(u_i, E_1)| < 1$, then the atom moves towards the carbon nanotube. It can be easily shown that $|H(u_i, E_1)| > 1$ is satisfied whenever $\Theta(u_i, E_1) > \delta/2$, except for the case of $\Theta(u_i, E_1) = \delta/2$, whereas $|H(u_i, E_1)| < 1$ is satisfied whenever $\Theta(u_i, E_1) < \delta/2$. Given that, we can determine the minimum circular energy E_R by solving $\Theta(u_i, E_c) = \delta/2$ and the cut-off energy E_c by solving $\Theta(u_i, E_c) = 0$, thus

$$E_c = -\frac{2u_i^2}{\varepsilon}(\xi^3 - u_i^3), \qquad E_R = E_c - \frac{\delta u_i^2 (u_i^3 - \xi^3)^{3/2}}{\varepsilon}. \tag{2.60}$$

It is interesting to note that $E_R < E_c$. For simplicity, we assume here that E_1, E_c and E_R are all negative real numbers. However, this cut-off energy is not sufficient

to determine the atom's loci. For example, if $E_1 > E_c$, then $|H(u_i, E_1)| > 1$ follows. But, it is naive to think that r will always keep increasing, which corresponds to either a parabolic or a hyperbolic orbit. An increment in r may also increase the value of E_c if and only if $u_i < (2/5)^{1/3}\xi$. Assuming that the value of E_1 is sufficiently small such that E_1 falls below E_c, then $|H(u_i, E_1)| < 1$ occurs and the atom will start to move towards the carbon nanotube, which corresponds to an elliptic orbit. Hence, both the initial position and the initial total energy are paramount to determine the atom's loci. Note that in this sub-section, we investigate only a qualitative description of the atom's loci, where the full prediction of its loci can only be determined by solving Eq. (2.44).

2.3.6 Fullerene–carbon nanotube system

In this sub-section, we determine the loci of a C_{60} fullerene orbiting around a (6,6) carbon nanotube of infinite length. To obtain the interaction potential energy between the two molecules, we perform double integrals of the Lennard-Jones potential over the surface of the fullerene and the carbon nanotube. In addition, the classical spinning of a fullerene, which arises from atomic vibrations, is also incorporated into the model to encapsulate the possible physical phenomenon at the nanoscale. Due to the symmetry of the problem, there is a radial force acting between the center of the fullerene and the carbon nanotube, which provides a centripetal force to the fullerene moving around the carbon nanotube, so that the fullerene eventually orbits around the center of mass of the carbon nanotube in a perpendicular plane. Results from the previous atom–carbon nanotube system can be employed in this system. The illustration of this system is shown in Fig. 2.26, where a, b and r denote the radius of a $(6, 6)$ carbon nanotube, the radius of the C_{60} fullerene and the distance between the center of the carbon nanotube and the center of the fullerene respectively. The molecular potential energy of this system can be written as

$$V = n_t n_f \int_{\Sigma_t} \int_{\Sigma_f} \left(-\frac{A}{\rho^6} + \frac{B}{\rho^{12}} \right) dS_f dS_t, \tag{2.61}$$

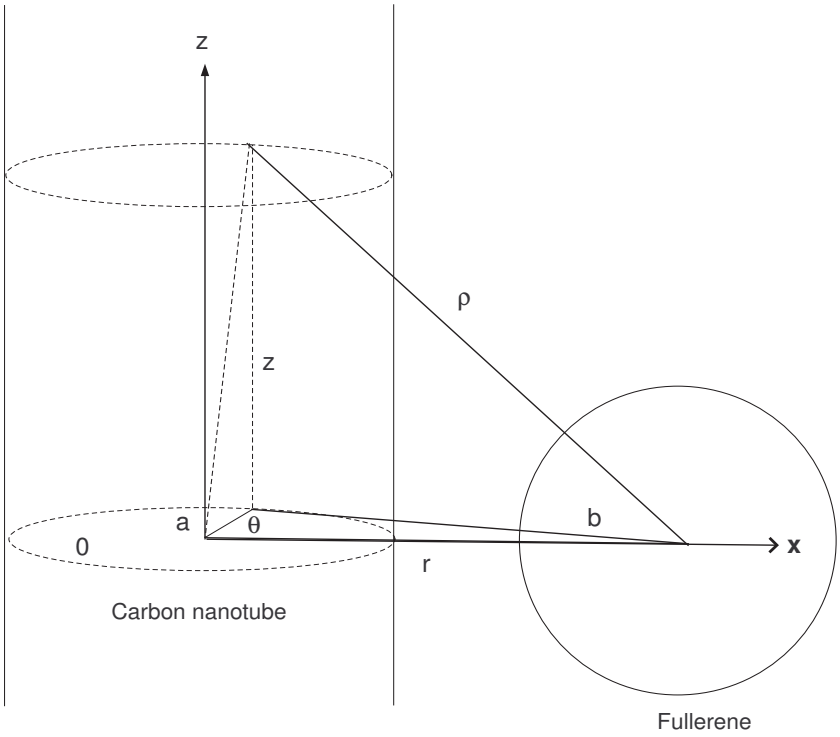

Figure 2.26: Fullerene orbiting around a carbon nanotube.

where n_t, n_f and ρ denote the mean surface density of atoms on the carbon nanotube, the mean surface density of atoms on the fullerene, and the distance between an atom on the fullerene and an atom on the carbon nanotube, respectively. In addition, dS_f and dS_t denote the surface area segments of the fullerene and the carbon nanotube, respectively. Following Mahanty and Ninham [96] and Ruoff and Lorentz [131], the potential energy for an atom interacting with a fullerene of radius b can be deduced as $P(\rho) = -Q_6(\rho) + Q_{12}(\rho)$, where $Q_n(\rho)$ is defined by

$$Q_n = \frac{2C_n n_f \pi b}{\rho(2-n)} \left\{ \frac{1}{(\rho+b)^{n-2}} - \frac{1}{(\rho-b)^{n-2}} \right\}, \tag{2.62}$$

where the constants C_6 and C_{12} denote A and B, respectively. By performing another surface integral over the surface of the carbon nanotube, the molecular potential energy becomes

$$\begin{aligned} V(\rho) &= n_t a \int_{-\infty}^{+\infty} \int_0^{2\pi} P d\theta dz = n_t n_f \pi a b \int_{-\infty}^{+\infty} \int_0^{2\pi} \frac{1}{\rho} \left(\frac{A}{2} \left[\frac{1}{(\rho+b)^4} - \frac{1}{(\rho-b)^4} \right] \right. \\ &- \left. \frac{B}{5} \left[\frac{1}{(\rho+b)^{10}} - \frac{1}{(\rho-b)^{10}} \right] \right) d\theta dz, \end{aligned} \tag{2.63}$$

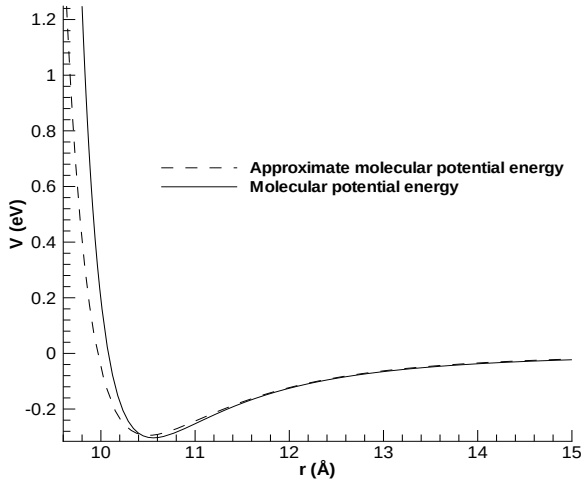

Figure 2.27: Molecular potential energy (2.64) and its approximation (2.65) for fullerene–carbon nanotube system.

where $\rho = \sqrt{\lambda^2 + z^2}$ and $\lambda = \sqrt{r^2 - 2ar\cos\theta + a^2}$. Upon integrating Eq. (2.63), we obtain

$$\begin{aligned} V(r) &= 16n_t n_f \pi ab\Bigg[- A\left(bJ_3 + 2b^3 J_4\right) \\ &+ \frac{B}{5}\left(5bJ_6 + 80b^3 J_7 + 336b^5 J_8 + 512b^7 J_9 + 256b^9 J_{10}\right)\Bigg], \end{aligned} \tag{2.64}$$

where

$$J_n = \frac{(2n-3)!!\pi^2}{(2n-2)!!}\frac{F(n-1/2, 1/2; 1; -4ar/[(r-a)^2 - b^2])}{[(r-a)^2 - b^2]^{n-1/2}},$$

where F and !! denote the usual hypergeometric function [26] and the double factorial notation such that $(2n-1)!! = (2n-1)(2n-3)...3\cdot 1$ and $(2n)!! = (2n)(2n-2)...4\cdot 2$, respectively. It is easy to observe from Eq. (2.64) that the molecular potential energy has a singularity at $r = a + b$ owing to the repulsive potential energy from the Lennard-Jones potential. The molecular potential energy of the system is plotted in Fig. 2.27.

We note that the behaviour of the potential energy (2.64) is similar to that of the atom–carbon nanotube system. However, the potential well is two orders of

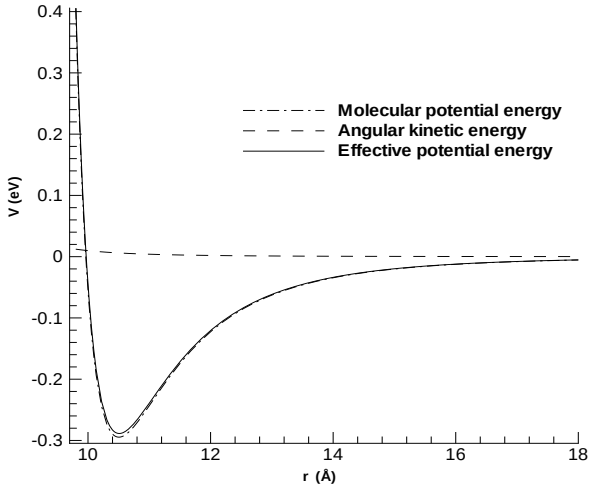

Figure 2.28: Fullerene's angular energy, ensemble molecular energy and effective potential energy.

magnitude larger than that of the atom–carbon nanotube system. This indicates that this system would be less sensitive to any thermal fluctuations arising from the environment. It is therefore expected that experimentally, the orbiting behavior of a fullerene can be observed easier than that of a single atom. Assuming that all the thermal energy, which is equal to the potential difference between the zero potential and the dip, is converted into the kinetic energy of the fullerene, the escape velocity is estimated to be 287.31 ms^{-1}, which can be achieved in laboratories by liquid helium cooling [137]. To simplify our analysis, if $a < r$ and only the lowest order of b is considered, then Eq. (2.64) reduces to a potential form, which is similar to the atom–carbon nanotube system, namely

$$V(r) = -\frac{A''}{[(r-a)^2 - b^2]^{5/2}} + \frac{B''}{[(r-a)^2 - b^2]^{11/2}}, \tag{2.65}$$

where $A'' = 6n_t n_f \pi^3 ab^2 A = 24 \times 10^2$ eVÅ^5 and $B'' = 39.375 n_t n_f \pi^3 ab^2 B = 0.26 \times 10^8$ eVÅ^{11} are modified attractive and repulsive constants respectively. As shown in Fig. 2.27, the approximate potential energy (2.65) is in good agreement with the actual molecular potential energy (2.64).

Owing to the symmetry of this problem, the results in the atom-carbon nanotube

system can be readily extended to this system by utilizing the substitution of $R \rightarrow \sqrt{(R-a)^2-b^2}$. According to Eq. (2.50), the threshold circular orbiting radius of this system, which is bounded and stable, is given by

$$\sqrt{(R-a)^2-b^2} = (3B''/A'')^{1/6} = 5.6 \text{ Å} \quad \Rightarrow \quad R = 10.7 \text{ Å}. \tag{2.66}$$

The orbiting frequency of the fullerene can be calculated utilizing Eq. (2.45), and is equal to $f = 4$ GHz, given that the angular momentum of the system h is equal to 3.44×10^{-12} kgm^{2}s^{-1}. In addition, the fullerene's angular kinetic energy can be computed to be equal to $5/r^2$ eV. The angular kinetic energy, molecular potential energy and effective potential energy for a C_{60}–carbon nanotube system are plotted together in Fig. 2.28 for comparison. Since the angular kinetic energy in this system is small in comparison to the molecular potential energy, the effective potential energy is essentially the same as the molecular potential energy and this gives rise to a different interpretation of the classification of loci in comparison to the atom–carbon nanotube system. In particular;

- The fullerene is in a circular orbit, which is bounded at the potential well of V_{eff},
- When the total energy of the fullerene increases but remains below 0 eV, the fullerene's locus is elliptic, which is bounded,
- When its total energy equals 0 eV, its locus is parabolic, which is unbounded,
- When its total energy becomes strictly positive, its locus is hyperbolic, which is unbounded.

Finally, the classical spinning effect of the fullerene may be incorporated into the model. Since the fullerene can spin due to the atomic vibrations at the nanoscale, the spinning kinetic energy may be written as $I\omega^2/2$, where $I = 2mb^2/3$ and ω are the moment of the inertia and the spinning frequency of the C_{60} molecule, respectively. The presence of the spinning shifts the effective potential energy upward

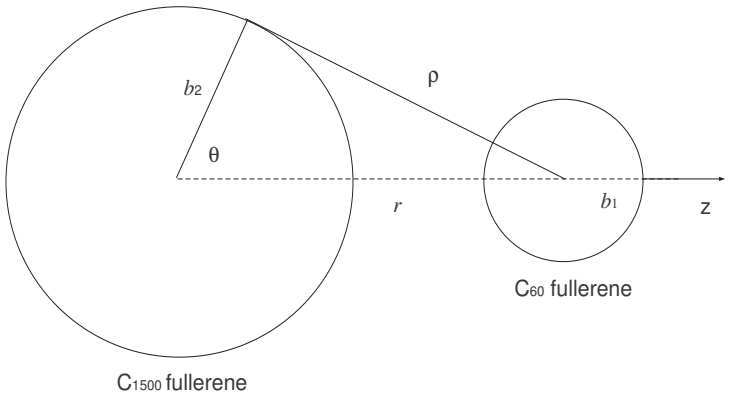

Figure 2.29: Geometry of a C_{60} molecule orbiting around a C_{1500} fullerene.

by the amount of $I\omega^2/2$, however the analysis to determine the fullerene's locus is principally the same as shown in this sub-section.

2.3.7 Fullerene–fullerene system

In this sub-section, we study the orbiting of a C_{60} fullerene around a C_{1500} fullerene. An illustration of this system is given in Fig. 2.29. The C_{1500} fullerene is chosen due to the fact that the center of mass of this system coincides with the center of the C_{1500} fullerene, which therefore simplifies our calculations. The solution method for this system is very similar to the fullerene–carbon nanotube system. However, due to the spherical symmetry of this system, the molecular potential energy can be obtained in a simpler manner because the axis of the line joining the centers of the two fullerenes can be aligned with the z-axis of the larger fullerene, and the molecular potential energy of the system becomes

$$V(\rho) = n_1 n_2 \pi b_1 \int_{\Sigma_2} \frac{1}{\rho} \Bigg\{ \frac{A}{2} \left[\frac{1}{(\rho + b_1)^4} - \frac{1}{(\rho - b_1)^4} \right] - \frac{B}{5} \left[\frac{1}{(\rho + b_1)^{10}} - \frac{1}{(\rho - b_1)^{10}} \right] \Bigg\} dS_2, \tag{2.67}$$

where n_1, n_2 and b_1 denote the mean surface densities of atoms on the C_{60}, the C_{1500} fullerenes and the radius of the C_{60} fullerene respectively. By exploring the symmetry of this system, the orbital radius r can be aligned with the z-axis of the larger C_{1500} fullerene. Hence, from the cosine law we have $\rho = \sqrt{b_2^2 + r^2 - 2b_2 r \cos\theta}$,

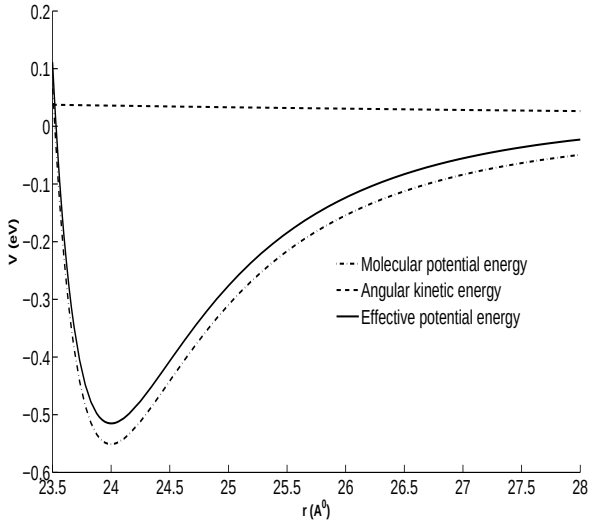

Figure 2.30: Molecular potential energy, angular kinetic energy and effective potential energy for C_{60}–C_{1500} system.

where b_2 denotes the radius of the C_{1500} fullerene. By performing the integration over the surface of C_{60} and C_{1500} fullerenes, the molecular potential energy $V(r)$ becomes

$$V(r) = -Q_6(r) + Q_{12}(r), \tag{2.68}$$

where

$$\begin{aligned} Q_n(r) &= \frac{4\pi^2 C_n b_1 b_2 n_1 n_2}{r(n-2)(n-3)} \left\{ \frac{1}{(b_1+b_2+r)^{n-3}} + \frac{1}{(b_1-b_2-r)^{n-3}} \right. \\ &- \left. \frac{1}{(b_1+b_2-r)^{n-3}} - \frac{1}{(b_1-b_2+r)^{n-3}} \right\}, \end{aligned} \tag{2.69}$$

where $C_6 = A$ and $C_{12} = B$. The molecular potential energy is plotted as shown in Fig. 2.30.

We observe that this energy becomes singular at $r = b_1 + b_2$, similar to that of the fullerene–carbon nanotube system. Further, the circular orbiting radius in this system becomes very close to the radius obtained directly by minimizing the

molecular potential energy alone. Therefore, according to Fig. 2.30, the circular orbiting radius can be readily read off as $R = 24$ Å and the orbiting frequency is calculated as

$$f = \frac{1}{2\pi}\sqrt{\frac{V'(R)}{mR}} = 1.6 \text{ GHz}, \tag{2.70}$$

where m is the total mass of the C_{60} molecule. The angular kinetic energy, which is given by $24.5/r^2$ eV, and the effective potential energy are plotted together with the molecular potential energy in Fig. 2.30. Similar to the fullerene–carbon nanotube system, the classical spinning effect can also be incorporated in this system and the classification of loci can be similarly examined. This orbiting effect may be detected experimentally since the fullerene's escape velocity is calculated to be 365.76 ms^{-1}.

2.3.8 Conclusion

In this section, three two-body nanoscale problems are examined, namely an atom-carbon nanotube system, a fullerene-carbon nanotube system and a fullerene-fullerene system. The effective potential energy of these proposed systems are found to be similar to the classical planetary potential energy. The circular orbiting radii of all the proposed nano systems are estimated by seeking the minimum energy configuration of their effective potential energies. Since the loci for these nano systems cannot be determined in terms of well-known analytical functions, a numerical method has been employed to obtain the various loci of the orbiting paths. In addition, a perturbation method has been utilized in order to gain some insight into possible analytical formulations of the loci. Most importantly, the circular orbiting frequencies of all three proposed nano systems reach the gigahertz range.

2.4 List of Symbols

Section 2.1

A is the attractive constant 14

B is the repulsive constant 14

E is the non-bonded molecular potential energy 13

$\mathbf{E_0}$ is the applied electrical field 24

$\mathbf{F_f}$ is the frictional force 24

$\mathbf{F_{vdW}}$ is the van der Waals force 17

F_r is the centripetal forces 19

T is the absolute temperature 20

$\mathbf{V}$ is the horizontal velocity 24

a is the radius of the nanotube 25

b is the radius of the C_{60} fullerene 25

$\mathbf{d}$ is the bulk dipole moment 24

dS_f is the surface element of the C_{60} fullerene 14

dS_t is the surface element of the nanotube 14

h is the conservation of angular momentum 18

$\mathbf{j}$ is the current density 24

m is the mass of the C_{60} fullerene 29

m_a is the mass of a single carbon atom 20

n_f is the mean surface density of the C_{60} fullerene 14

n_t is the mean surface density of the nanotube 14

r_0 is the preferred radial distance (Ideal system) 19

r_s is the preferred stable radius 19

t^* is the transitional time 30

v is the circumferential velocity 20

v_{rms} is the root mean square velocity 20

v_t is the translational velocity 31

Φ is the potential function between two atoms 14

ρ is the atomic distance between two typical surface elements 14

ρ_{ij} is the atomic distance between two atoms 14

Section 2.2

(A, A, C) is the principal moments of inertia at the center of mass 38

(X, Y, Z) is the space-fixed frame of the top 37

(x, y, z) is the body-fixed frame of the top 37

(ϕ, θ, ψ) are the Euler angles 38

$\mathbf{F}$ is the retarding force 38

$\mathbf{F_f}$ is the frictional force 39

$\mathbf{H}(\mathbf{B})$ is the retarding magnetic force at P 39

$\mathbf{L}$ is the total angular momentum in the body-fixed frame 38

$\mathbf{N}$ is the normal force 38

R is the radius of the top 38

$\mathbf{W}$ is the weight of the top 38

$\dot{\mathbf{X}}$ is the center of mass velocity 38

g is the gravitational constant 42

m is the mass of the top 38

$\mathbf{n}$ is the total angular velocity in the body-fixed frame 38

$\mathbf{r}$ is the position vector OP 38

$\mathbf{v_p}$ is the sliding velocity at P 38

Ω is the angular velocity around the Z axis 38

μ is the frictional coefficient 39

ω is the angular velocity around the z axis 38

Section 2.3

A is the attractive constant 47

B is the repulsive constant 47

A' is the modified attractive constant for atom-nanotube system 47

B' is the modified repulsive constant for atom-nanotube system 47

C' is the angular kinetic constant for atom-nanotube system 48

A'' is the modified attractive constant for fullerene-nanotube system .. 61

B'' is the modified repulsive constant for fullerene-nanotube system ... 61

D is the attractive constant for the hard-sphere potential 55

E is the total energy of the system 48

E_c is the cut-off energy 57

E_R is the minimum circular energy 57

L is the Lagrangian of the systems 45

M is the total mass of the system 45

R is the circular orbit of radius 46

$T(\dot{\mathbf{P}}, \dot{\mathbf{r}})$ is the kinetic energy of the system 45

V_{eff} is the effective potential energy 46

$V(r)$ is the connecting potential energy 45

a is the radius of the (6,6) nanotube 58

b is the radius of the C_{60} fullerene 57

dS_f is the surface area segment of the fullerene 59

dS_t is the surface area segment of the carbon nanotube 59

f is the circular orbiting frequency 50

h is the conservation of angular momentum 46

m_a is the mass of an carbon atom 48

n_f is the mean surface density of of the C_{60} fullerene 59

n_t is the mean surface density of of the carbon nanotube 47

r_0 is the initial position 52

u $u = r^{-1}$ 48

μ is the reduced mass of the system 46

ρ is the distance between two arbitrary atoms 47

σ is the collision diameter 55

ω is the circular angular velocity 49

Chapter 3

Axial buckling of carbon nanotubes and nanopeapods

In this chapter, we utilize continuum mechanics to model the axial buckling and the instability of carbon nanotubes and nanopeapods and discuss their applications in nano-electromechanical systems (NEMS), which couple between the mechanical properties of nanotubes and nanopeapods and the applied external electrostatics forces.

3.1 Single-walled carbon nanotubes as a nonlinear buckled beam for nano-electromechanical systems

In this section, the nano-electromechanical effects on a doubly clamped suspended carbon nanotube are studied. Doubly clamped suspended carbon nanotubes have been previously manufactured and their electronic transport [155, 109, 168, 44], acoustoelectric [122], thermal [77] and elastic [75] properties have been measured. We assume that a carbon nanotube is attached to two electrodes by tunneling contacts, in which Coulomb-blockade effects dominate the transport. We note that subtle effects like shuttle-like electromechanical instability may result in additional

charges transporting through the system due to the unstable ground state with respect to any small spatial deviations from the equilibrium position when the gate voltage exceeds a certain threshold, are ignored in this section [72]. The applied gate voltage bends the tube and affects both the carbon nanotube's electrical and mechanical properties (see Fig. 3.1 for a schematic picture). That is, the applied gate voltage pushes electrons inside the nanotube downwards by means of the electrostatic force which changes the nanotube's mechanical status. The nanotube undergoes an axial mechanical deflection, which leads to a prominent change in the tube electronic band gap, and these results in a sensitive change of the conductance of the nanotube. Since the buckled nanotube can act as an internal transistor [36], it can be utilized to sense its own motion through the electrical detection of conductance change [151]. Furthermore, the recent realization of nano-electromechanical sensors based on carbon nanotubes shows that the electrical measurement of the resistance of doubly clamped single-walled carbon nanotube under a mechanical load, such as pressure coming from an atomic force microscopy-tip, undergoes a significant increase in the nanotube resistance with respect to the deflection of the nanotube and such measurement is reversible owing to the sp^2 bonding of carbon atoms in the nanotube [60]. However, Sapmaz et al. [134] model this nano-electromechanical system by a linear beam theory, which completely ignores curvature effects at the nanoscale. We extend their model by fully incorporating curvature into the elastic energy term and we find that the numerical solution admits quite different buckling behavior to that obtained by Sapmaz et al. [134].

The section is organized as follows. In sub-section 3.1.1, we incorporate curvature into the elastic energy and we re-examine the electrostatic energy of the buckled carbon nanotube. The maximum displacement of the buckled carbon nanotube is then presented in the following two sub-sections, where both an approximate solution and a numerical solution, which incorporates curvature, are examined. While the approximate solution can be expressed analytically in both the weak and strong bending regimes, the full solution incorporating curvature obtained here can only be

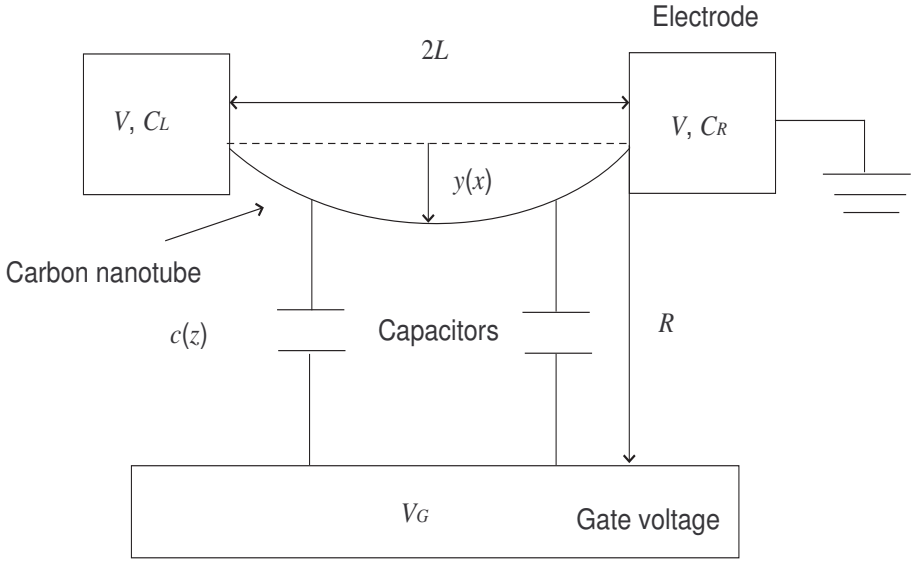

Figure 3.1: Schematic of experimental setup.

determined numerically. In sub-section 3.1.4, some numerical results and discussion are made and some conclusions are presented in the final sub-section of this section.

3.1.1 Total energy of nanotube with incorporation of curvature

In this sub-section, we examine a single-walled carbon nanotube of total length $2L$, which is strongly suspended between two electrodes through tunneling contacts. An electrostatic force, arising from the gate voltage, bends the nanotube in a discrete way when an electron is tunneled through the nanotube. Further the nanotube is assumed to be initially lying along the x-axis and the displacement of the nanotube, which arises due to the electrostatic force between the nanotube and the gate voltage, is denoted by y and is illustrated in Fig. 3.1. The elastic energy of this system $W_{el}[y]$, which is determined in Appendix 6.5, is given by

$$W_{el}[y] = \int_0^{2L} \left\{ \frac{1}{2} EI \frac{y''^2}{(1+y'^2)^{5/2}} + T_{total}[\sqrt{1+y'^2} - 1] \right\} dx, \tag{3.1}$$

where E and $I = \pi r^4/4$ (r further denotes the thickness of the nanotube), denote the elastic modulus and the inertial moment, respectively. In addition, T_{total} is defined as the sum of the residual stress T_0 resulting from the fabrication of the nanotube and the induced stress T resulting from the buckling of the nanotube caused by the gate voltage. Note that if $y' \approx 0$ is assumed, Eq. (3.1) reduces to the equation (1) in Sapmaz et al. [134], namely

$$W_{el}[y] = \int_0^{2L} \left\{ \frac{EI}{2} y''^2 + \frac{1}{2} T_{total} y'^2 \right\} dx.$$

For simplicity, the residual stress is assumed to be zero, so that the total stress T_{total} denotes only the induced stress T. By utilizing Hooke's law, the explicit form of T can be deduced. The infinitesimal stress is given by

$$dT = ES \frac{ds - dx}{2L} = ES \frac{\sqrt{dx^2 + dy^2} - dx}{2L}, \tag{3.2}$$

where S denotes the cross-sectional area of the nanotube. Upon integrating Eq. (3.2), we find

$$T = \frac{ES}{2L} \int_0^{2L} \left(\sqrt{1 + y'^2} - 1 \right) dx. \tag{3.3}$$

Similarly, Eq. (3.3) reduces to the equation (2) in Sapmaz et al. [134] if $y' \approx 0$ is assumed, namely

$$T = \frac{ES}{4L} \int_0^{2L} y'^2 dx. \tag{3.4}$$

Before determining the electrostatic energy of the system, we denote C_L, C_R, C_G and $c(y)$ as the capacitance of the left electrode, the right electrode, the gate voltage

and the capacitance of the gate per unit length, respectively. In addition, we define the distance between the nanotube in its relaxed state and the gate voltage by R and assume y is much smaller than R, which are illustrated in Fig. 3.1. Thus, $c(y)$ is given by

$$c(y) = \frac{1}{2}\left[\ln\frac{2(R-y)}{r}\right]^{-1} \approx \frac{1}{2}\left[\ln\frac{2R}{r}\right]^{-1} + y(x)\left[2R\ln^2\frac{2R}{r}\right]^{-1}. \tag{3.5}$$

A detailed derivation of Eq. (3.5) can be found in Appendix 6.6. The general expression for any electrostatic energy W_{est} is given by

$$W_{est} = \frac{1}{2}V_i C_j^i V^j, \tag{3.6}$$

where V_i and C_j^i denote the electrostatic potential and capacitance tensors respectively, and we utilize the suffix notation to imply summation over a repeated index. Due to the configuration of the system, V^i, which is the conjugate of V_i, and C_j^i are accordingly defined by

$$V^i = \begin{bmatrix} ne \\ V \\ V_G \end{bmatrix},$$
$$C_j^i = \frac{1}{C_L + C_R + C_G}\begin{bmatrix} 1 & -C_L & -C_G \\ -C_L & -C_L(C_R + C_G) & C_L C_G \\ -C_G & C_L C_G & -C_G(C_L + C_R) \end{bmatrix}. \tag{3.7}$$

Therefore, the W_{est} becomes

$$\begin{aligned} W_{est} &= \frac{1}{2(C_L+C_R+C_G)}\Big\{(ne)^2 - 2ne(C_LV + C_GV_G) \\ &- C_L(C_R+C_G)V^2 - C_G(C_L+C_R)V_G^2 + 2C_LC_GVV_G\Big\}, \end{aligned} \tag{3.8}$$

where by the definition of $c(y)$, the capacitance of the gate C_G is defined as

$$C_G = \int_0^{2L} c(y)dx. \tag{3.9}$$

Since our interest lies in examining how curvature affects the bending of the nanotube, C_L and C_R are assumed to be zero and the expression for W_{est} simplifies to

$$W_{est} = \frac{(ne)^2 \ln \frac{2R}{r}}{2L} - \frac{(ne)^2}{4L^2R}\int_0^{2L} y(x)dx - neV_G, \tag{3.10}$$

where n ane e denote the number of electrons and the electron charge, respectively. The total energy W_n, which is the sum of the elastic and the electrostatic energy, is then given by

$$\begin{aligned} W_n &= \int_0^{2L}\left\{\frac{EI}{2}\frac{y''^2}{(1+y'^2)^{5/2}} + T\left(\sqrt{1+y'^2}-1\right) - \frac{(ne)^2}{4L^2R}y\right\}dx \\ &+ \frac{(ne)^2 \ln \frac{2R}{r}}{2L} - neV_G. \end{aligned} \tag{3.11}$$

Owing to the minimum energy configuration of the buckled nanotube at statistical equilibrium, the total energy W_n has to be minimized. The functional F can be easily extracted from Eq. (3.11) as

$$F = \frac{EI}{2}\frac{y''^2}{(1+y'^2)^{5/2}} + T\left(\sqrt{1+y'^2}-1\right) - \frac{(ne)^2}{4L^2R}y. \tag{3.12}$$

In the following sub-sections, this functional is utilized to obtain the maximum displacement of the buckled nanotube for both the approximate analytical solution and the numerical solution.

3.1.2 Displacement for buckled nanotube with $y' \approx 0$

In this sub-section, for the sake of completeness, we restate the buckled displacement of the nanotube, which is given by section II.A. in Sapmaz et al. [134] by neglecting the curvature. Owing to the fact that the buckled nanotube will eventually reach its statistical equilibrium, variational principles can be utilized and the Euler-Lagrange equation reads

$$IEy'''' - Ty'' = K_0, \tag{3.13}$$

where $K_0 = (ne)^2/(4L^2R)$. To solve the above equation, the stress T has to be initially assumed to be constant, where the value of T can be determined later by utilizing the self-consistent Eq. (3.3) once the displacement y is known. If the origin of the coordinate system is located at the center of the relaxed nanotube, and the following Cauchy boundary conditions: $y(-L) = y(L) = y'(-L) = y'(L) = 0$, are employed, then the solution to the above equation can be easily obtained as

$$\begin{aligned} y &= \frac{K_0 L}{T\xi}\left\{\frac{\sinh 2\xi L}{\cosh 2\xi L - 1}\left[\cosh\xi(x+L)-1\right] - \sinh\xi(x+L)\right. \\ &+ \left.\xi(x+L) - \frac{\xi}{2L}(x+L)^2\right\}, \end{aligned} \tag{3.14}$$

where $\xi = \sqrt{T/(EI)}$. For this approximation, the stress T given by Eq. (3.3) reduces to the stress T given by Eq. (3.4), so that upon substituting Eq. (3.14) into Eq. (3.4), one may find the stress T in the weak and the strong bending limit as

$$T = \begin{cases} K_0^2 L^6 S/945EI^2 & T \ll (EI)/(4L^2), \\ \left(ESK_0^2 L^2/6\right)^{2/3} & T \gg (EI)/(4L^2), \end{cases} \tag{3.15}$$

where the solution for $T \ll (EI)/(4L^2)$ in Eq. (3.15) corresponds to the weak bending of the nanotube, while the solution for $T \gg (EI)/(4L^2)$ in Eq. (3.15) corresponds to the strong bending of the nanotube. We note that these stresses are asymptotic expression by taking the limit of stresses in both regimes. Furthermore, Eq. (3.15) can be substituted into Eq. (3.14) to obtain the displacement of the buckled nanotube. Owing to the symmetry of the buckled nanotube, the maximum displacement occurs at $x = 0$, so that the maximum displacement of the nanotube for both the weak bending and strong bending regimes are determined to be

$$y_n^{max} = \begin{cases} 0.012\left(neL/\sqrt{ER}r^2\right)^2 & T \ll (EI)/(4L^2), \\ 0.381\left(neL/\sqrt{ER}r^2\right)^{2/3} & T \gg (EI)/(4L^2). \end{cases} \tag{3.16}$$

Eq. (3.16) states that whenever an extra electron is tunneled through the potential barrier V by the gate potential V_G, the nanotube bends further, which is known as nano-electromechanical effect. However, the bending behavior is different for both the weak and strong bending regimes. In the weak bending regime, the maximum displacement y_n^{max} depends on n^2, while in the strong bending regime, y_n^{max} depends only on $n^{2/3}$, which indicates that the nanotube responds more sensitively to the existence of encapsulated electrons in the weak bending regime than in the strong bending regime. However, we doubt the result given by Eq. (3.16) in the strong bending regime due to the fact that Sapmaz et al. [134] adopt a strong stress limitation over the approximated beam theory, which may incur contradiction. In

practice, the number of electrons n is rather hard to measure experimentally, but we can relate the gate voltage to the number of the encapsulated electrons by substituting Eq. (3.14) into the electrostatic energy W_{est} and minimizing Eq. (3.10) with respect to the number of electrons n. Upon performing the calculation, one may find that

$$n = \text{int}\left\{ \frac{V_G L}{e \ln(2R/r)} + \frac{1}{2} + \delta n \right\}, \tag{3.17}$$

where int represents taking the closest minimum integer value.

3.1.3 Displacement for a buckled nanotube with incorporation of curvature

In this sub-section, the displacement of a buckled nanotube is sought by incorporating the full expression for curvature into the elastic energy of the buckled nanotube, which can be seen as a natural extension of the previous sub-section. However, in this scenario we are not able to solve the governing Eq. (3.21) analytically, and therefore a modified numerical method, which is analogous to Euler's method, is employed to obtain the maximum displacement of the buckled nanotube. Similar to the approximate case, we employ the Euler-Lagrange equation on the total energy W_n to derive the governing equation of the buckled nanotube. The Euler-Lagrange equation, which involves terms of y up to the second derivative, is given by

$$F_y - \frac{d}{dx}F_{y'} + \frac{d^2}{dx^2}F_{y''} = 0 \quad \Rightarrow \quad F_{y'} - \frac{d}{dx}F_{y''} = -K_0 x + c_1, \tag{3.18}$$

where from Eq. (3.12), $-F_y = K_0 = (ne)^2/(4L^2R)$ and c_1 denotes a constant of integration. However, upon substituting the functional (3.12) into Eq. (3.18), we find that to solve the above Euler-Lagrange equation is in vain. Instead, we employ the first integral (see Appendix 6.7 for details) to reduce the order of the differential

equation by one, which takes the invariance of F in the x-coordinate into account, such that the first integral is given by

$$F - y'\left(F_{y'} - \frac{d}{dx}F_{y''}\right) - y''F_{y''} = c_2, \tag{3.19}$$

where c_2 is another constant of integration. After simplifying Eq. (3.19) utilizing the Euler-Lagrange equation (3.18), gives

$$\frac{y''^2}{(1+y'^2)^{5/2}} - 2\xi^2\sqrt{1+y'^2} + F_0 y - y'(F_0 x - c_3) = c, \tag{3.20}$$

where $F_0 = (ne)^2/(2IERL^2)$, $c_3 = (2c_1)/(IE)$ and c is a recast constant. Upon applying the following Cauchy boundary conditions: $y(-L) = y(L) = y'(-L) = y'(L) = 0$, and exploring the symmetry of the buckled nanotube, c_3 is found to be zero, which further reduces Eq. (3.20) into

$$\frac{y''^2}{(1+y'^2)^{5/2}} - 2\xi^2\sqrt{1+y'^2} + F_0(y - xy') = c. \tag{3.21}$$

To determine c, the Cauchy conditions are again substituted into Eq. (3.21), giving

$$c = \alpha^2 - 2\xi^2, \tag{3.22}$$

where $\alpha = y''(-L) = y''(L)$. For natural boundary problems, i.e. by relaxing the fixed boundaries to obtain extra physical insights into a physical problem, see Appendix 6.7, we find that the second derivative and the third derivative of the displacement, i.e. $y''(x)$ and $y'''(x)$, correspond to the bending moment and the shear force of the buckled nanotube respectively. The maximum displacement y_{max} is given by

$$y_{max} = 2\left\{ y''^2(L) - y''^2(0) \right\} \frac{IERL^2}{(en)^2}. \tag{3.23}$$

However, the solution of y_{max} requires the known general solution for y in the first place. To determine y, we adopt a modified Euler's method to solve Eq. (3.21) numerically. Given Cauchy boundary conditions, the numerical solution of a second order differential equation, for example Eq. (3.21), can be obtained naturally and progressively. As a benchmark, we also show the compatibility between Eq. (3.23) and Eq. (3.16) in the weak bending regime given in Appendix 6.8. The numerical scheme is outlined as follows: The displacement y at a small distance, $\varepsilon > 0$, from the two ends of the nanotube can be found by utilizing Taylor expansions. That is

$$y(-L+\varepsilon) = y(-L) + \varepsilon y'(-L), \qquad y(L-\varepsilon) = y(L) - \varepsilon y'(L). \tag{3.24}$$

In addition, the second derivative of the displacement at any point on the interval $2L$, including the two end points, can be determined utilizing the governing equation (3.21) with the prescribed boundary conditions, namely

$$y''(\pm a) = \pm\sqrt{[c - F_0(y(a) - ay'(a)) + 2\xi^2\sqrt{1+y'(a)^2}][1+y'(a)^2]^{5/2}}, \tag{3.25}$$

where a takes values between 0 and L. Note that the positive moment y'' is defined as an anticlockwise moment and vice versa. The first derivative of the displacement y', can then be obtained utilizing Taylor expansions, in particular

$$y'(-L+\varepsilon) = y'(-L) + \varepsilon y''(-L), \qquad y'(L-\varepsilon) = y'(L) - \varepsilon y''(L). \tag{3.26}$$

Upon utilizing Eq. (3.25) and Cauchy boundary conditions, Eq. (3.26) can be determined uniquely. Likewise, $y(\mp L \pm 2\varepsilon)$ and $y'(\mp L \pm 2\varepsilon)$ can be evaluated in a similar manner. As a result, the Cauchy data propagates from the two ends towards the center of the nanotube gradually and hence the governing equation (3.21) can be solved numerically in this manner. If $y(-L+\varepsilon)$ is assumed to be equal to $y(L-\varepsilon)$, then $y'(L)$ must be equal to $-y'(-L)$ and more generally, $y'(a) = -y'(-a)$ for $a \in [0, L]$. After a close examination of Eq. (3.26), one may also find that the bending moment is symmetric, i.e. $y''(a) = y''(-a)$. Owing to the symmetry of the buckled nanotube, it is enough to consider only one half interval, i.e. $[0, L]$, where the displacement on the other half interval $[-L, 0]$ can be obtained by reflection. In addition, the buckled nanotube's curvature changes from concave up to concave down within the region from $x = 0$ to $x = L$, and for simplicity, we assume that the change of curvature occurs at $x = L/2$ for all n (we test this assumption and find that the change of curvature at $x = L/2$ gives us the correct buckling shape for all force regimes investigated in this section).

3.1.4 Numerical results and discussion

In this sub-section, numerical results for the maximum displacement of the buckled nanotube including the incorporation for the full expression of curvature into the elastic energy of the buckled nanotube are investigated and discussed. According to Figs. 3.2 and 3.4, the numerical solution indicates that while the approximate solution underestimates the maximum displacement of the buckled nanotube in the weak bending regime, it provides an entirely different prediction of the maximum displacement in the strong bending regime. We observe that the displacement y and its first derivative will both vanish if $c = -2\xi^2$, which corresponds to the case $n = 0$. For other values of n, the second derivative of the approximate solution given in Eq. (3.14), and the corresponding value of T in Eq. (3.15), are utilized to approximate c and the parameter F_0. For example, upon assuming that $r = 0.65$ nm, $E = 1.25$ TPa, $L = 250$ nm and $R = 100$ nm, then for 10 grid points and n

ranging from 0 to 1000. We note that the conversion between the number of the encapsulated electrons and the gate voltages V_G is related by Eq. (3.17) and the range is chosen for the comparison purposes only and may be practically difficult to detect but shows the sensitivity of the nano-electromechanical system. We determine numerical values of the maximum displacement of the buckled nanotube in the weak bending regime and the numerical solution, the semi-analytical solution, i.e. Eq. (6.50) and the approximate solution are shown in Fig. 3.2. The numerical results indicate that although there is a discrepancy between the numerical solution and the approximation solution/the semi-analytical solution (since they overlap) in the weak bending regime, the difference between the two solutions is linear, i.e. there is a 10% difference in comparison between two solutions. Hence, a scaling factor can be utilized to calibrate the discrepancy between both solutions in the weak bending regime. In addition, we note that the magnitude of the maximum displacement is small for the proposed range of gate voltage V_G due to the fact that the corresponding stress is small (see Fig. 3.3). We will expand these ranges later to obtain more measurable values of the maximum displacement.

We now examine the numerical results for the strong bending regime, for which we maintain the values of previous parameters but we employ the strong bending stress T from Eq. (3.15) to carry out the numerical scheme. In this case, for 10 grid points and n ranging from 0 to 5000, we determine both the numerical solution and the approximation solution and are shown in Fig. 3.4. The corresponding stress is also shown in Fig. 3.5 to indicate the small maximum displacement, which is suggested in Fig. 3.4. We note that the maximum displacement obtained from the numerical solution exceeds the maximum displacement obtained from the approximate solution after approximately $n = 3500$. Therefore, the numerical solution provides an entirely different picture in comparison to the results from the approximate solution in the strong bending regime, and for which the factor scaling proposed in the weak bending regime is no longer sufficient to correct for the discrepancy between both solutions owing to the non-linear effect arising from the

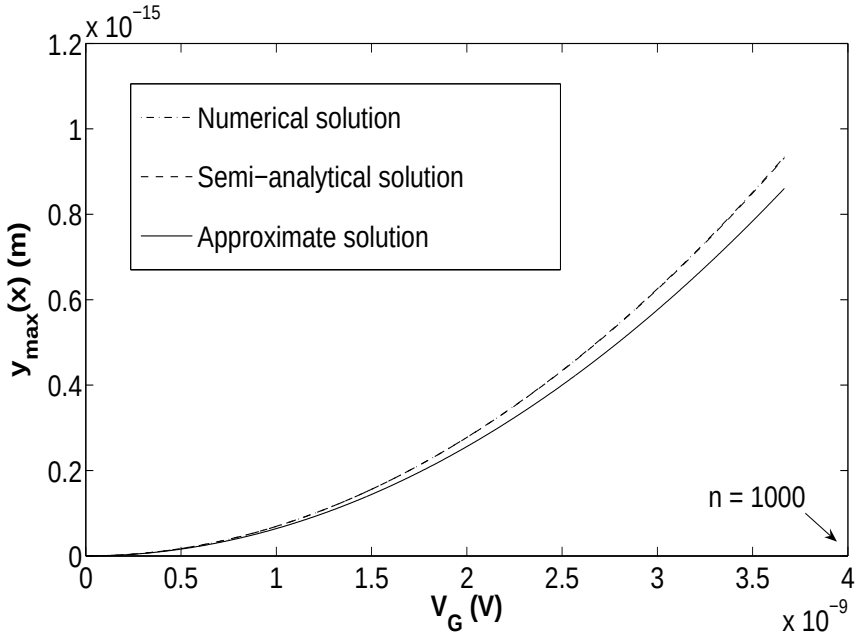

Figure 3.2: Numerical results for buckled nanotube in weak bending regime, where the upper line represents the numerical solution with the incorporation of curvature into the elastic energy of the buckled nanotube, the middle line represents Eq. (6.50) and the lower line represents the approximate solution without curvature.

utilization of the full expression for the curvature in the elastic energy. Therefore, according to the compatibility between the approximate solution and the numerical solution established in Appendix 6.8, we may only adopt the numerical solution to predict the more accurate maximum displacement in the strong bending regime.

Given the above numerical results, it is beneficial to plot the maximum displacement of the numerical solutions in both the weak and strong bending regimes as given in Fig. 3.6. The crossing from the weak bending regime to the strong bending regime is clearly demonstrated at approximately $n = 100$. Therefore, in practice we can totally ignore the weak bending regime provided that the corresponding maximum displacement is difficult to be measured experimentally. In addition, the numerical solution reveals that the buckled nanotube responds more sensitively, i.e. there is a higher rate of change of the maximum displacement with respect to the external electrostatic force in the strong bending regime than in the weak bending regime, which is shown to be reversible for the results given by the approximate solution. To determine a practically measurable maximum displacement, we relax

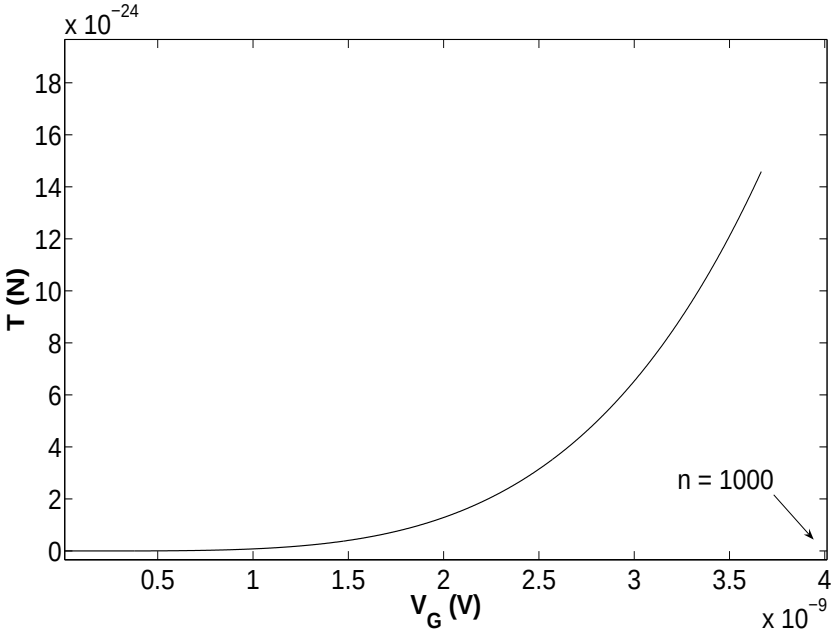

Figure 3.3: Stress for buckled nanotube in the corresponding weak bending regime shown in Fig. 3.2.

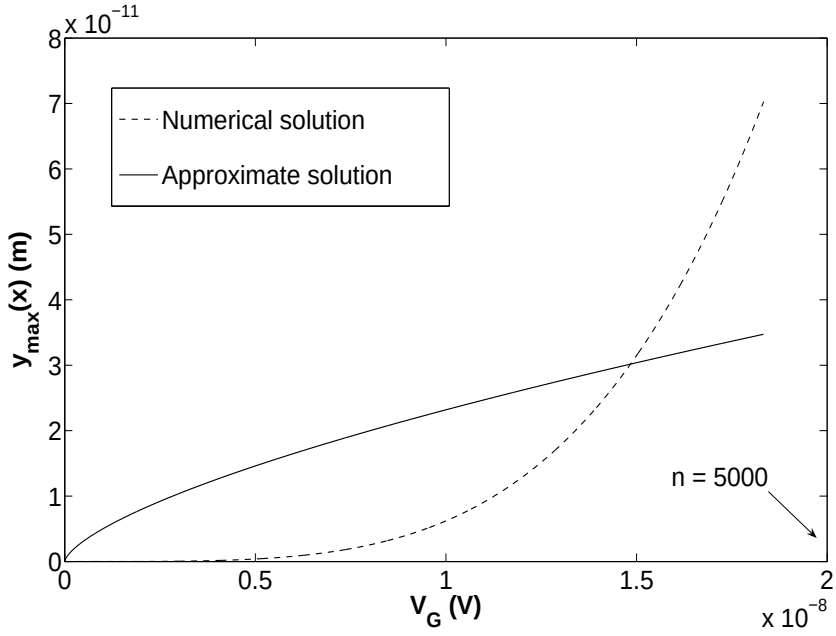

Figure 3.4: Numerical results for buckled nanotube in strong bending regime, where the flatter curve represents the approximate solution while the other curve represents the numerical solution.

the number of electrons to $n = 1 \times 10^4$ and the numerical results for both regimes together with the corresponding stress are plotted in Figs. 3.7 and 3.5 respectively. It is noteworthy that the buckling displacement in the weak bending region is severely compressed in comparison to the buckling displacement in the strong bending re-

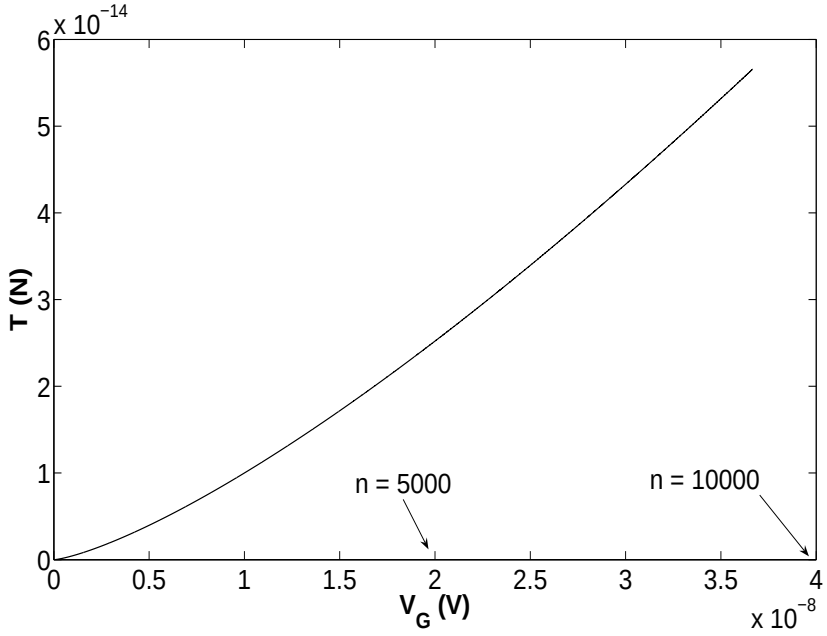

Figure 3.5: Stress for buckled nanotube in the corresponding strong bending regime shown in Fig. 3.4 and Fig. 3.7.

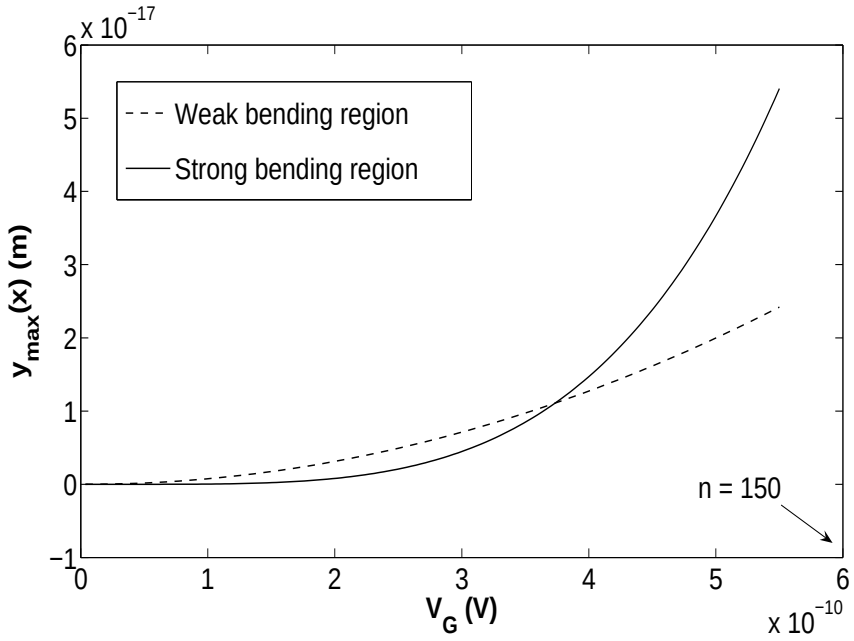

Figure 3.6: Numerical results for buckled nanotube in both weak and strong bending regimes, where the crossing between both bending regimes occurs around $n = 100$.

gion. Since the most practical bending usage lies in the strong bending regime, the full curvature effects must be addressed at the nanoscale.

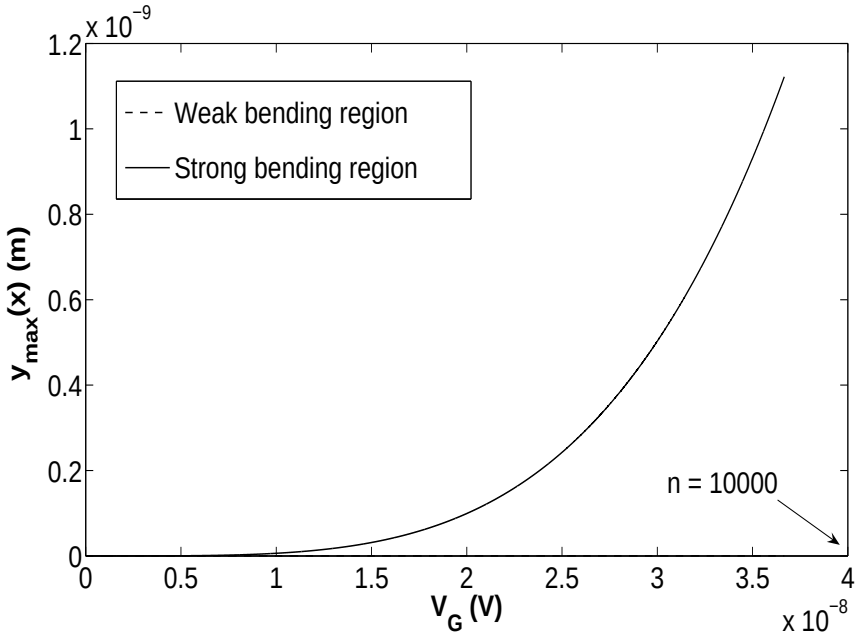

Figure 3.7: Numerical results for buckled nanotube in both weak and strong bending regimes with the maximum $n = 10000$.

3.1.5 Conclusion

We have determined a new solution for the maximum displacement of a buckled nanotube in both the weak and strong bending regimes by incorporating the full expression for curvature into the elastic energy of the buckled nanotube, which is ignored in previous investigations. We find that while the approximate solution underestimates the maximum displacement of the buckled nanotube in the weak bending regime, our numerical solution predicts an entirely different bending behavior in comparison to the approximate solution in the strong bending regime. Further, in the former case, a scale factor can be utilized to calibrate the discrepancy between the approximate solution and the numerical solution. However, this scale factor is found not to be sufficient in correcting the maximum displacement of the buckled nanotube due to the nonlinear bending phenomenon in the strong bending regime. Hence, for most practical purposes a numerical solution with the full curvature effects has to be utilized in this bending regime.

3.2 Axial buckling of multi-walled carbon nanotubes and nanopeapods

Continuum mechanics has been widely and successfully applied for the mechanical analysis of carbon nanotubes as an alternative to the overwhelming Molecular dynamics simulation approaches. More recently, Govindjee et al. [50] adopt the Benoulli-Euler beam theory to obtain the Young's modulus of multi-walled nanotubes. According to a multiple-elastic beam model, Yoon et al. [175] examine resonant frequencies and obtain vibrational modes of an individual multi-walled carbon nanotube embedded inside an elastic medium. Li et al. [92] also utilize a space truss model to determine the Young and shear moduli of a single-walled carbon nanotube. Moreover, Yakobson et al. [171] utilize a traditional continuum shell model to predict the buckling of a single-walled carbon nanotube and their results are compared with molecular dynamics simulation. Last but not least, a finite element method [116] and a molecular dynamics simulation [110, 147, 93, 178] is also utilized to investigate the buckling behavior of nanotubes.

Here, we further investigate the axial buckling of a nanopeapod, which possesses a chain of fullerenes inside a carbon nanotube. Nanopeapods have been experimentally observed by Smith et al. [145, 146] through high-resolution transmission electron microscopy. It is suggested that encapsulation of C_{60} molecules occurs either through a large opening in the tube wall [13] or through the open ends of the nanotube [158, 159]. For the different possible equilibrium configurations of fullerenes inside a nanotube (e.g. linear, zigzag and spiral patterns), we refer the reader to Baowan et al. [8].

Axial buckling can be practically demonstrated as a nano-electromechanical effect on a doubly clamped suspended nanotube or nanopeapod. We assume that a nanotube or a nanopeapod is attached by two electrodes through tunneling contacts, in which Coulomb-blockade effects dominate the transport. The applied gate voltage bends the tube by an applied external electrical field $\mathbf{E_0}$ and affects both

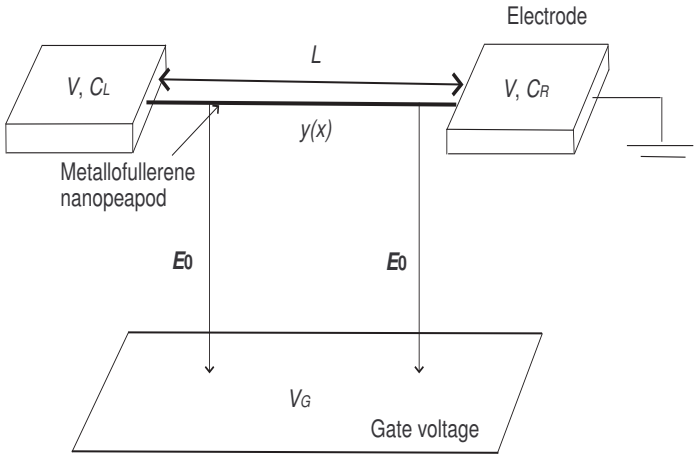

Figure 3.8: Experimental setup for doubly clamped suspended nanopeapods.

the electrical and mechanical properties of the nanostructure, which is generally called nano-electromechanical system (see Fig. 3.8). Similar to the case of doubly clamped single-walled carbon nanotubes, such hybrid molecular structures as multi-walled carbon nanotubes and nanopeapods can be implemented as nanotweezers [76, 1], switches in a random access memory device [129], actuators [10] and nano-electromechanical switches [34, 78]. In addition, with its electronic properties in nature, nanopeapods with metallofullerenes embedded can be utilized as more efficient on-and-off gigahertz oscillators [179, 90, 27, 28] through an applied external electric field.

This section is structured as follows. In sub-section 3.2.1, we introduce Donnell's equation and from which we determine the critical forces for single- and double-walled carbon nanotubes and single- and double-walled nanopeapods. We also comment on the issues regarding the various interactions between molecules mainly van der Waals interactions which affect the critical forces of our proposed systems. In sub-section 3.2.2, we approximate the single-walled carbon nanotube and the single-walled nanopeapods by one-dimensional structures so that we may adopt Euler-Bernoulli beam theory to study the doubly clamped suspended single-walled nanopeapods, and the resulting buckling displacements are compared with the buckling displacement of a single-walled carbon nanotube. Some conclusions are given in the final sub-section and certain detailed mathematical derivations are

presented in three appendices to avoid logical disruption in the main text.

3.2.1 Axial buckling stability analysis

Thin shell theories based on continuum mechanics have been successfully applied to predict several mechanical properties of carbon nanostructures, such as single- and double-walled carbon nanotubes. In particular, Ru et al. [128, 56] investigate an axial stability and the wave-like behavior of double- and multi-walled carbon naotubes by incorporating van der Waals interactions between layers of the carbon structures. Similar approaches have also been utilized in other studies, such as for the vibration of a multi-layered graphene sheet [12] and the torsional and axial bending stability of carbon nanotubes [53, 173, 164]. While some studies have been done on the torsional stability of nanopeapods [161, 147]. Only recently, Sohi and Naghdabadi [148] investigate the stability of single-walled carbon nanopeapods under both the axial and compressive load by utilizing Donnell's equilibrium equation. Here, we extend the work from Sohi and Naghdabadi [148] but determine the axial buckling stability of multi-walled carbon nanotubes and nanopeapods theoretically but only analytically investigate up to double-walled nanopeapods. In addition, Euler-Bernoulli beam equation has also been adopted to predict the post-buckling behavior of the single-walled nanotube and nanopeapods with the incorporation of curvature effect. We have to emphasize that all results presented in this section are obtained analytically, which set our work apart from the prior work of Sohi and Naghdabadi [148].

Here, we investigate axial stability of the proposed nanostructures by utilizing Donnell's equation. Forces between the layers of carbon nanotubes with different radii must satisfy Newton's third law, i.e. $p_{i,j}R_i = -p_{j,i}R_j$, where $p_{i,j}$ denotes the pressure exerted from the jth layer to the ith layer, R_i denotes the tube radius for the ith layer and where subscripts $i = 1...N$ denote the ith layer of the carbon nanotube. We further assume that the incremental pressure Δp_i of the ith layer arising from an adjacent jth layer to be linear in the displacement difference between the two

layers, i.e. $\omega_j - \omega_i$, where ω_i denotes the displacement of the ith layer. From these assumptions we may deduce

$$\begin{aligned}
&\Delta p_1 = p_{1,2} = c_1(\omega_2 - \omega_1),\\
&\Delta p_2 = p_{2,3} + p_{2,1} = c_2\left[(\omega_3 - \omega_2) - \frac{R_1}{R_2}(\omega_2 - \omega_1)\right],\\
&\quad\vdots \qquad \vdots\\
&\Delta p_N = p_{N,N-1},
\end{aligned} \tag{3.27}$$

where c_i denotes the linearity constant for the ith layer, which is derived in Appendix 6.9 utilizing the van der Waals interactions between nanotubes' layers and Taylor's expansion around an equilibrium configuration. On the other hand, the internal van der Waals pressure caused by fullerenes to the inner nanotube is defined by

$$p_{vdW}(z) = F_{vdW}(z)\left(\frac{3\sqrt{3}}{4}d_{cc}^2\right)^{-1}, \tag{3.28}$$

where $F_{vdW}(z)$ denotes the internal van dar Waals force and $(3\sqrt{3}d_{cc}^2)/4$ is the effective surface area of a carbon atom [132], and where d_{cc} is the carbon-carbon bond length. The circumferential membrane force per unit length (nanotube) or simply called circumferential membrane force caused by the van der Waals pressure p_{vdW} is given by

$$N_{1\theta} = -R_1 p_{vdW}(z), \tag{3.29}$$

where the negative sign accounts for the inward forces acting by fullerenes against the external forces. We model the carbon nanotubes utilizing infinitesimal buckled beam theory and Donnell's equation [128, 53], which originates from thin-shell theory, namely

$$D\nabla^8\omega + \frac{Eh}{R^2}\frac{\partial^4\omega}{\partial z^4} - \nabla^4\left[N_z\frac{\partial^2\omega}{\partial z^2} + 2N_{z\theta}\frac{\partial^2\omega}{\partial z\partial\theta} + N_\theta\frac{\partial^2\omega}{\partial\theta^2}\right] - \nabla^4 p(z,\theta) = 0, \tag{3.30}$$

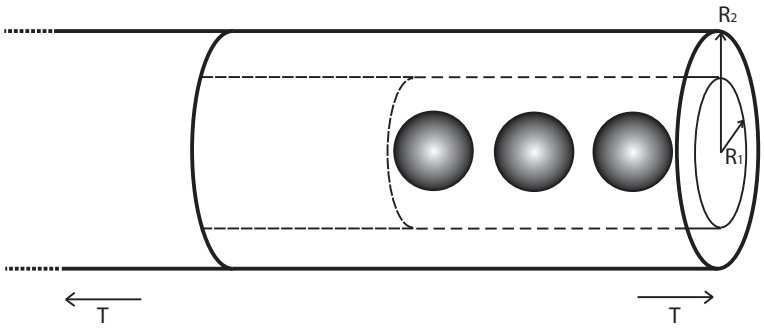

Figure 3.9: Nanopeapods.

where D, E, R, h, N_z, $N_{z\theta}$, N_θ and $p(z,\theta)$ denote the bending stiffness of the carbon nanotube, elastic modulus of the nanotube, the radius of the nanotube, the thickness of the nanotube, the axial force, the shear membrane force, the circumferential membrane force due to pre-buckling loading conditions, and the pressure exerted on the nanotube, respectively. Here, the operator ∇^2 is defined by $\partial^2/\partial z^2 + (1/R^2)\partial^2/\partial\theta^2$ and $p(z,\theta)$ comprises the van der Waals pressure between fullerenes and the wall of the inner nanotube as well as the pressure between two adjacent layers of nanotubes (see Fig. 3.9). Since we are only considering axial buckling, the shear membrane force $N_{z\theta}$ can be omitted, and this simplifies Eq. (3.30) to

$$D\nabla^8\omega + \frac{Eh}{R^2}\frac{\partial^4\omega}{\partial z^4} - \nabla^4\left[N_z\frac{\partial^2\omega}{\partial z^2} + N_\theta\frac{\partial^2\omega}{\partial\theta^2}\right] - \nabla^4 p(z,\theta) = 0, \tag{3.31}$$

Note that, we can practically determine N_z from the net applied axial force T, which is acting on the system arising practically from electrostatic forces, e.g. metallofullerenes so that we may write T as

$$T = qE_0/2\pi R_i, \tag{3.32}$$

where q, E_0 and R_i denote the total charge existing in the system, the strength of the externally applied electric field and the radius of the outer nanotube respectively. Assuming that the molecules are at equilibrium, the force per unit length acting on

different layers must be equal, which can be written as

$$N_{1z} = R_1 p_1 = N_{2z} = R_2 p_2 = \ldots = N_{Nz} = R_N p_N. \tag{3.33}$$

Thus, for the total applied force per unit length T, we have

$$\begin{aligned} T &= R_1 p_1 + R_2 p_2 + \ldots + R_N p_N, \\ &= R_1 p_1 + R_2 \left(\frac{R_1}{R_2} p_1\right) \quad + \ldots + R_N \left(\frac{R_1}{R_N} p_N\right) = N R_1 p_1, \end{aligned} \tag{3.34}$$

from which we obtain

$$p_1 = \frac{T}{N R_1}, \qquad N_{z_1} = R_1 \left(\frac{T}{N R_1}\right) = \frac{T}{N}, \tag{3.35}$$

where Eq. (3.33) is utilized to obtain Eq. (3.35). Following the same argument as that stated above, we may deduce

$$p_i = \frac{T}{N R_i}, \qquad N_{1z} = N_{2z} = \ldots = \frac{T}{N}. \tag{3.36}$$

We now propose that the axial buckling stability of doubly clamped suspended nanotubes or nanopeapods is periodic and the low-amplitude solution applies which takes the form

$$\omega_i = A_i \sin(\alpha z) \cos(\tau \theta), \tag{3.37}$$

where $\alpha = (k\pi)/L$ and L is the length of the nanotube, k and τ are the axial and circumferential wave numbers, respectively. Upon substituting Eq. (3.37) into Eq. (3.31), we obtain the system of equations which may be written in terms of the matrix equation as

$$\mathbf{F\Omega} = \mathbf{0}, \tag{3.38}$$

where the matrices $\mathbf{F}$ and $\mathbf{\Omega}$ are given by

$$\mathbf{F} = \begin{bmatrix} F_{11} & F_{12} & 0 & \cdots & \cdots & 0 \\ F_{21} & F_{22} & F_{23} & \cdots & \cdots & 0 \\ \cdots & \cdots & & & & \\ \cdots & \cdots & & & & \\ 0 & 0 & 0 & \cdots & F_{NN-1} & F_{NN} \end{bmatrix},$$

$$\mathbf{\Omega}^T = \begin{bmatrix} \omega_1, & \omega_2, & \cdots & \omega_N \end{bmatrix}, \tag{3.39}$$

and the elements F_{ij} of the matrix $\mathbf{F}$ are given explicitly by

$$\begin{aligned}
F_{11} &= D\left[\alpha^2 + \left(\frac{\tau}{R_1}\right)^2\right]^4 + \frac{Eh}{R_1^2}\alpha^4 + \left[\alpha^2 + \left(\frac{\tau}{R_1}\right)^2\right]^2 \left\{T\alpha^2 - p_{vdW}(z)\left(\frac{\tau}{R_1}\right)^2 - c_1\right\}, \\
F_{12} &= -c_2\left[\alpha^2 + \left(\frac{\tau}{R_2}\right)^2\right]^2, \\
F_{21} &= -c_1\left(\frac{R_1}{R_2}\right)\left[\alpha^2 + \left(\frac{\tau}{R_1}\right)^2\right]^2, \\
F_{22} &= D\left[\alpha^2 + \left(\frac{\tau}{R_2}\right)^2\right]^4 + \frac{Eh}{R_2^2}\alpha^4 + \left[\alpha^2 + \left(\frac{\tau}{R_2}\right)^2\right]^2 \left\{T\alpha^2 - c_2\left(1 + \frac{R_1}{R_2}\right)\right\}, \\
F_{23} &= -c_3\left[\alpha^2 + \left(\frac{\tau}{R_3}\right)^2\right]^2, \\
&\vdots \qquad \vdots \\
F_{NN-1} &= -c_{N-1}\left(\frac{R_{N-1}}{R_N}\right)\left[\alpha^2 + \left(\frac{\tau}{R_{N-1}}\right)^2\right]^2, \\
F_{NN} &= D\left[\alpha^2 + \left(\frac{\tau}{R_N}\right)^2\right]^4 + \frac{Eh}{R_N^2}\alpha^4 + \left[\alpha^2 + \left(\frac{\tau}{R_N}\right)^2\right]^2 \left\{T\alpha^2 - c_N\frac{R_{N-1}}{R_N}\right\},
\end{aligned} \tag{3.40}$$

and further denotes $c_1 = c$, where c is the constant arising from the van der Waals pressure between the first two layers and is defined by Eq. (6.58) in Appendix 6.9. For Eq. (3.38) to have a non-zero solution, it is necessary that $\det\mathbf{F} = 0$. For a double-walled nanopeapod, we obtain $F_{11}F_{22} - F_{21}F_{12} = 0$. Since $F_{11} \approx F_{22}$, we can simply approximate $F_{11}F_{22}$ by F_{11}^2 but we also adopt the mean approximation of $R_1 = \overline{R} = (R_1 + R_2)/2$ to correct any small variation between F_{11} and F_{22}.

Thus, we find the axial force per unit length $T = T(k, \tau)$ for the single-walled nanotube (10,10), the single-walled nanopeapods C_{60}@(10,10), the double-walled nanotube (10,10)@(16,16) and the double-walled nanopeapods C_{60}@(10,10)@(16,16) to be given respectively as

$$|T| = \begin{cases} \frac{D[\alpha^2+(\tau/R_1)^2]^4+(Eh/R_1^2)\alpha^4}{\alpha^2[\alpha^2+(\tau/R_1)^2]^2}, \\ \\ \frac{D[\alpha^2+(\tau/R_1)^2]^4+(Eh/R_1^2)\alpha^4-p_{vdW}(\tau^2/R_1)[\alpha^2+(\tau/R_1)^2]^2}{\alpha^2[\alpha^2+(\tau/R_1)^2]^2}, \\ \\ \frac{D[\alpha^2+(\tau/\overline{R})^2]^4+(Eh/\overline{R}^2)\alpha^4-c[\alpha^2+(\tau/\overline{R})^2]^2+\sqrt{cc_2(R_1/R_2)}[\alpha^2+(\tau/R_1)^2][\alpha^2+(\tau/R_2)^2]}{\alpha^2[\alpha^2+(\tau/\overline{R})^2]^2}, \\ \\ \frac{D[\alpha^2+(\tau/\overline{R})^2]^4+(Eh/\overline{R}^2)\alpha^4-[p_{vdW}(z)(\tau^2/\overline{R})+c][\alpha^2+(\tau/\overline{R})^2]^2+\sqrt{cc_2(R_1/R_2)}[\alpha^2+(\tau/R_1)^2][\alpha^2+(\tau/R_2)^2]}{\alpha^2[\alpha^2+(\tau/\overline{R})^2]^2}. \end{cases} \tag{3.41}$$

For the buckling of a single-walled nanotube without any fullerene enclosed, we have $F_{11} = 0$ with $p_{vdW} = c = 0$, namely there is no interaction arising from fullerenes and other layers between nanotubes. Similarly, for the single-walled nanopeapods, we incorporate p_{vdW} into Eq. $(3.41)_2$ to account for the molecular interactions arising from fullerenes. While we add both c and c_2 to describe the correct physical behavior arising from the layer's interactions for the double-walled nanotube, an extra van der Waals pressure p_{vdW} is also incorporated into Eq. $(3.41)_4$ to take the effect of the fullerenes inside the double-walled nanotube as the form of double-walled nanapeapods. We note that while the forces for (10,10) and (10,10)@(16,16) have the same analytical forms as stated in He et al. [56], the forces for C_{60}@(10,10) has the analytical forms as stated in Sohi and Naghdabadi [148]. However, Eq. $(3.41)_3$ and Eq. $(3.41)_4$ are obtained by mean approximation.

Further, we note that p_{vdW} can be determined analytically by utilizing the molecular interactions between a fullerene and an atom on the carbon nanotube (see Fig. 3.10). Such potential energy between a fullerene and an atom on the carbon nanotube, E^* is determined utilizing the 6-12 Lennard-Jones potential and the con-

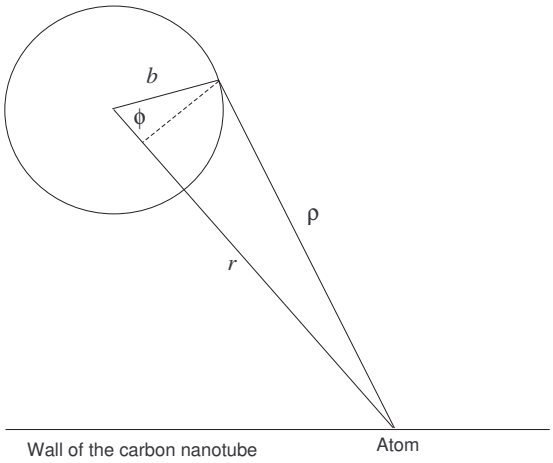

Figure 3.10: An atom on a carbon nanotube interacting with a C_{60} fullerene.

tinuous approximation, namely

$$E^* = n_f \int_{\Sigma_f} \left(-\frac{A}{\rho^6} + \frac{B}{\rho^{12}} \right) dS_f, \tag{3.42}$$

where A and B are the attractive and repulsive constants, n_f is the surface density of carbon atoms on the fullerene, ρ denotes a typical distance between the carbon atom and an atom on the fullerene and dS_f is the surface element of the fullerene. The numerical values of constants utilized in this model are given in Table 3.1. As

Radius of (10,10)	$R_1 = 6.784$ Å
Radius of (16,16)	$R_2 = 10.846$ Å
Radius of C_{60}	$b = 3.55$ Å
Carbon-carbon bond length	$d_{cc} = 1.421$ Å
Mean surface density of C_{60}	$n_f = 0.3789$ Å^{-2}
Attractive constant	$A = 17.4$ eV×Å^6
Repulsive constant	$B = 29 \times 10^3$ eV×Å^{12}

Table 3.1: Numerical values of constants utilized in Section 3.2.

shown in Cox et al. [27, 28], the potential E^* is given by

$$E^*(r) = \frac{\pi b n_f}{r} \left\{ \frac{A}{2} \left[\frac{1}{(r+b)^4} - \frac{1}{(r-b)^4} \right] - \frac{B}{5} \left[\frac{1}{(r+b)^{10}} - \frac{1}{(r-b)^{10}} \right] \right\}, \tag{3.43}$$

where b denotes the radius of the C_{60} fullerene. As such, the molecular force F_{vdW}

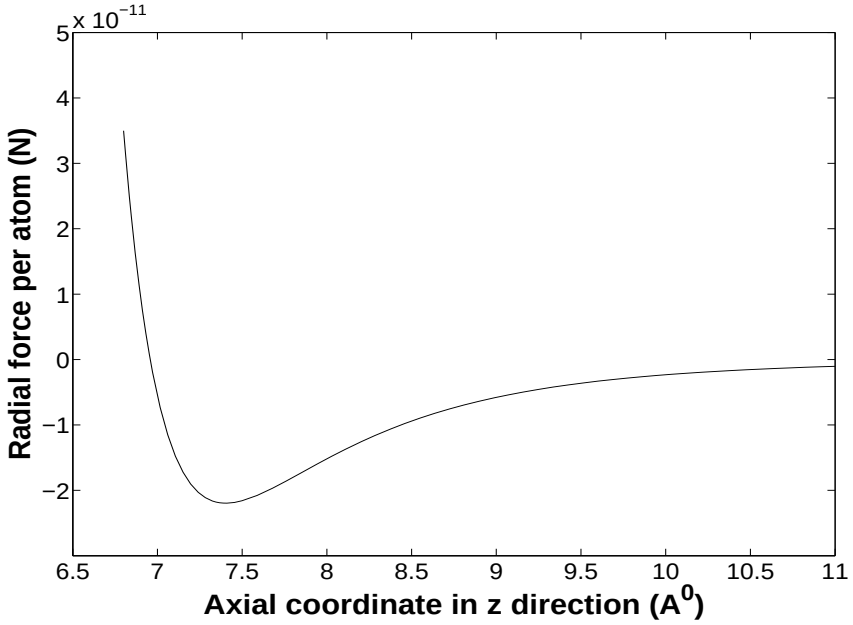

Figure 3.11: Radial force for an atom on a carbon nanotube interacting with a C_{60} fullerene.

between the atom and the fullerene can be determined from

$$F_{vdW} = -\nabla E^*. \tag{3.44}$$

Eq. (3.44) is plotted in Fig. 3.11 indicating that the maximum attractive force of 21 pN occurs at $z = 7.4$ Å, which is in agreement with the numerical data obtained from Smith et al. [145]. Hence, according to Eq. (3.28), the maximum p_{vdW} is found to be 0.8 GPa and the critical axial force can be obtained by minimizing the right hand side of Eq. (3.41).

Further, utilizing Eq. (3.41) we adopt the following parameter values: $L = 36.8$ Å, $D = 0.85$ eV, $h = 3.4$ Å, $Eh = 360$ J/m^2, $R_1 = 6.784$ Å, $R_2 = 10.846$ Å to determine the axial force distribution for (10,10), C_{60}@(10,10), (10,10)@(16,16) and C_{60}@(10,10)@(16,16). These results are shown graphically in Figs. 3.12, 3.13, 3.14 and 3.15 for the axial wave number k ranging from 1 to 50 and the circumferential wave number τ ranging from 1 to 10, respectively. For all four cases, we note that the critical forces T_c, or local minimum for such axial forces are obtained as 86 nN, 69 nN, 64 nN and 56 nN for (10,10), C_{60}@(10,10), (10,10)@(16,16) and

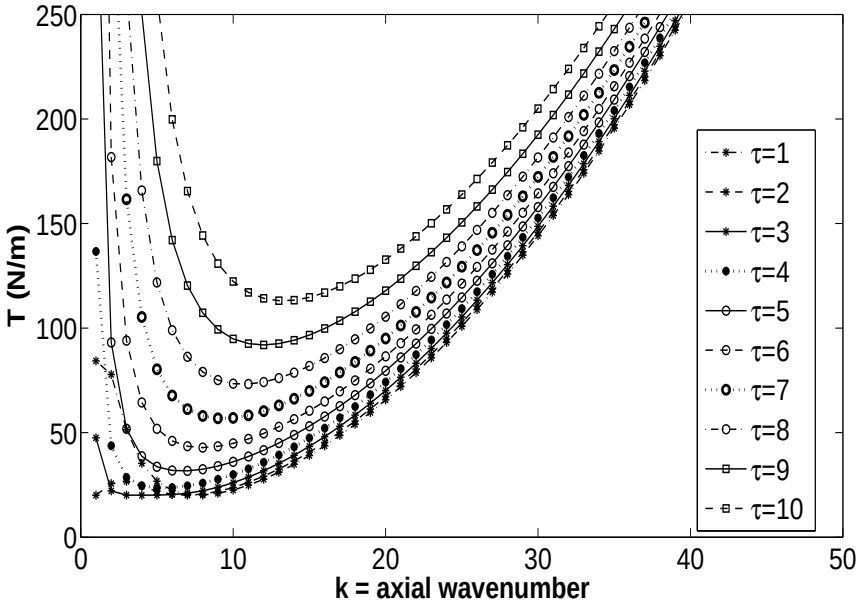

Figure 3.12: Applied force T for different k and τ for (10,10).

C_{60}@(10,10)@(16,16), respectively. We note that while the first two are obtained by multiplying the corresponding critical forces per unit length by $2\pi R_1$, the last two are obtained by multiplying by $2\pi R_2$. The numerical results for the critical forces indicate that both the molecular interactions from the layers between the inner and the outer nanotubes as well as fullerenes and the inner nanotube decrease the resistance to the axial buckling of the nanostructures in order to maintain the global stable minimum energy state of the material. That is consistent with classical beam theory for which it is known that the presence of the inward internal force reduces the critical force of a cylindrical shell [154].

Upon utilizing Hooke's law, we can relate the critical strain ε_c with the critical force T_c by $\varepsilon_c = T_c/(SE)$, where S and $E = 1.06$ TPa denote the cross-section area and elastic modulus of the nanotube, respectively. For (10,10) nanotube, we obtain from Fig. 3.12 that $\varepsilon_c = 5.7\%$. This value is generally well in agreement with the range of published data obtained by utilizing molecular dynamics (MD) simulation on (10,10) nanotube with various methodologies. The critical strain comes close to the results of Yakobson et al. [171], i.e. $\varepsilon_c = 5.68\%$. Moreover, our value also lies between Liew et al. [93], i.e. $\varepsilon_c = 6.6\%$ and Zhang et al. [178], i.e. $\varepsilon_c = 5.6\%$. As

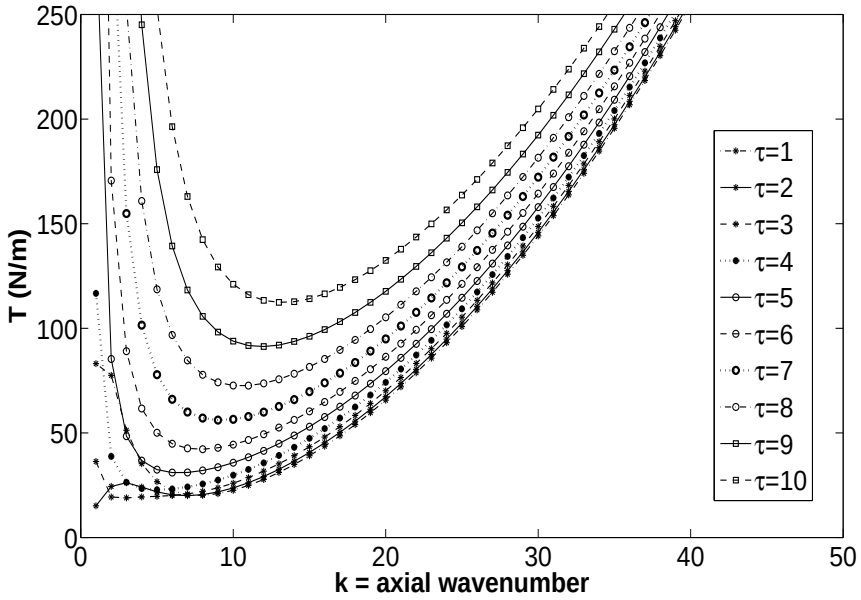

Figure 3.13: Applied force T for different k and τ for C_{60}@(10,10).

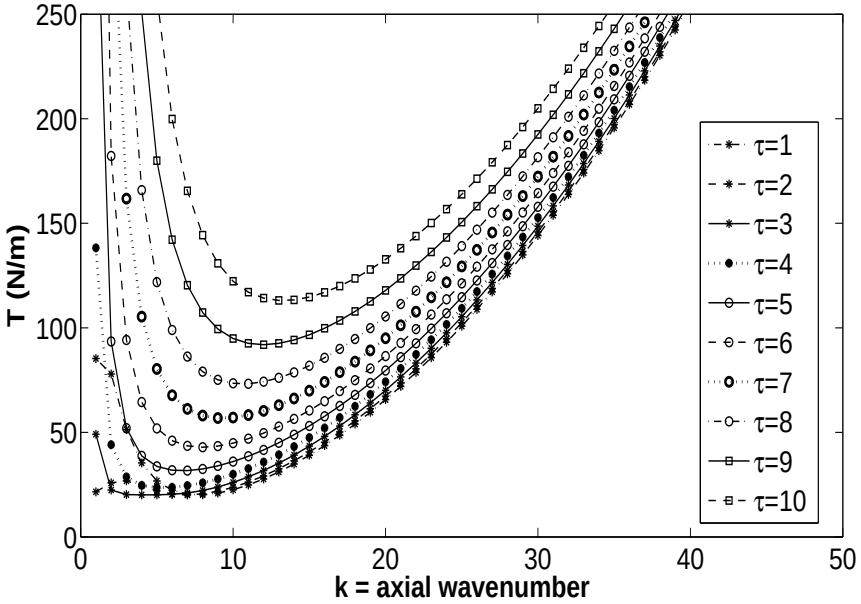

Figure 3.14: Applied force T for different k and τ for (10,10)@(16,16).

for the case of C_{60}@(10,10) nanopeapods, upon comparing between Figs. 3.12 and 3.13, the critical force for the C_{60}@(10,10) is around 69 nN, which is 25% less than the critical force for (10,10) nanotube, i.e. 86 nN. Such reduction in the critical force of the single-walled nanopeapods in comparison to that of the single-walled nanotube can be explained by the existence of the inward van der Waals pressure between the wall of the nanotube and the nearby fullerene. The critical strain for the

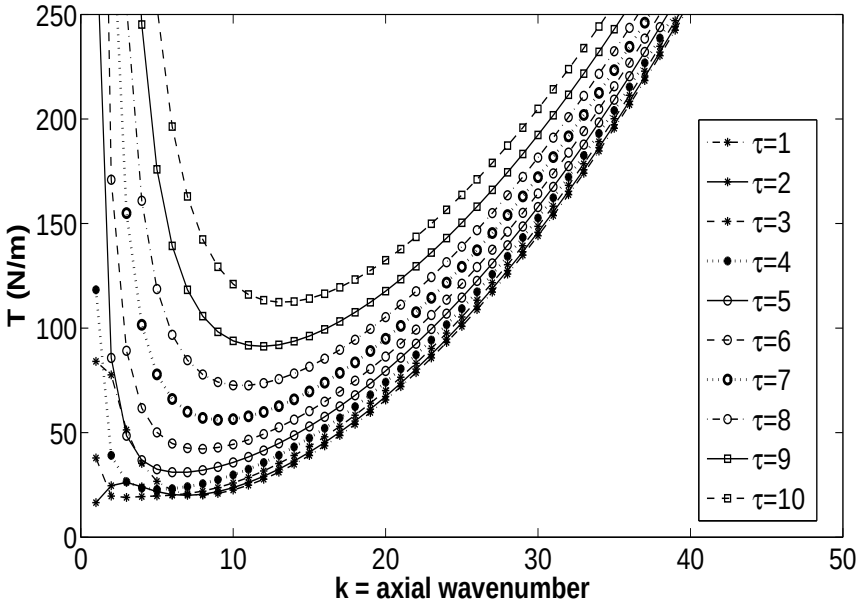

Figure 3.15: Applied force T for different k and τ for C_{60}@(10,10)@(16,16).

single-walled nanopeapods can be analogously obtained as $\varepsilon_c = 4.5\%$, which is also comparable with the molecular dynamics simulation result obtained by Shen [143], who investigates the axial buckling of nanopeapods either filled with or without argon atoms. For the empty capacity, the author reports $\varepsilon_c = 4.8\%$. Since most literature investigates the buckling instability of a smaller nanotube embedded inside a (10,10) nanotube as a double-walled nanotube, we adopt the same methodology presented above but replace R_1 and R_2 by 3.39 Å and 6.78 Å representing for the radius of the (5,5) nanotube and the (10,10) nanotube, respectively and obtain the critical stress for the (5,5)@(10,10) as 84.6 nN, which are comparable with Zhang et. al [178], i.e. 88 nN. The comparison between the results arising from our continuum model and the MD results are then summarized in Table. 3.2

For the buckling phenomena for the double-walled nanotubes and nanopeapods, upon comparing between Fig. 3.12 and Fig. 3.14, the critical force for the double-walled nanotube (10,10)@(16,16) is slightly less than the critical force for the single-walled nanopeapods by 5 nN due to the fact that the larger outer-tube radius in the former case resulting in a smaller critical force [3]. The small discrepancy between the critical forces for the single-walled nanopeapods and the double-walled nanotube

Molecular type	Our results	MD results
(10,10)	$\varepsilon_c = 5.7\%$	$\varepsilon_c = 5.6\%$ (Zhang et al. [178]) $\varepsilon_c = 5.68\%$ (Yakobson et al. [171]) $\varepsilon_c = 6.6\%$ (Liew et al. [93])
C_{60}@(10,10)	$\varepsilon_c = 4.5\%$	$\varepsilon_c = 4.8\%$ (Shen et al. [143])
(10,10)@(16,16)	$T_c = 64$ nN	NiL
(5,5)@(10,10)	$T_c = 84.6$ nN	$T_c = 88$ nN (Zhang et al. [178])
C_{60}@(10,10)@(16,16)	$T_c = 56$ nN	NiL

Table 3.2: Comparison between our continuum model and MD results.

can also be explained by (I) the short interaction range of the van der Waals forces, (II) the effective contact surface area and (III) the distance between the internal molecular structures. Since we model the van der Waals force in particular by the Lennard-Jones potential, which is a short range potential, for each atom on the outer shell of the nanotube, it experiences a spectrum of molecular forces arising from the inner shell in the case of the double-walled nanotube, but only experiences molecular forces arising from the nearby fullerene in the case of the single-walled nanopeapods. In other words, the effective contact surface area between layers of nanotubes is larger than the effective contact surface area between fullerenes and the inner nanotube. In addition, since we assume that the fullerenes are located along the axis due to the prescribed radius of the inner nanotube (10,10) [8], but the layers come closer to each other and hence the larger inward van der Waals forces acting between layers rather than fullerenes and the inner wall of (10,10) nanotube gives rise to the smaller critical force. Comparing Fig. 3.14 and Fig. 3.15, the further reduction of the critical force for the double-walled nanopeapods by 8 nN in comparison to the critical force for the double-walled nanotube can be explained from a combination of the analysis in this paragraph and the previous one. We have not derived the stability analysis for multi-walled nanotubes/nanopeapods because of the difficulty of solving $\det\mathbf{F} = 0$ analytically in general. However, we strongly suspect that the critical forces for multi-walled nanopeapods will be reduced even further as the number of layers increases due to the increasing influence of the van der Waals interactions between layers [56], while the van der Waals forces arising

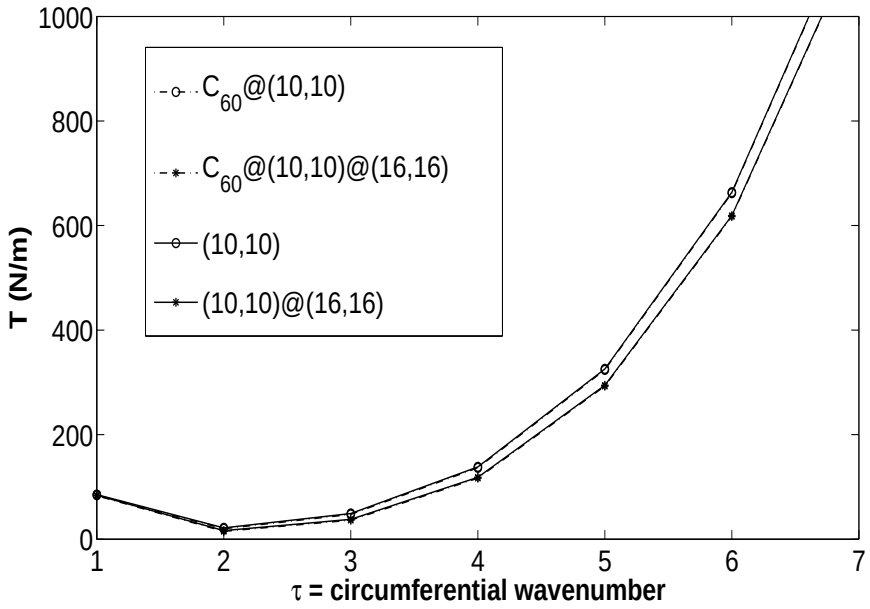

Figure 3.16: Applied force T for k=1 for all proposed systems.

from fullerenes in the multi-walled nanopeapods is almost negligible.

To investigate the influence of the embedded fullerenes and the layer effect in the high force regime, we can plot a graph by fixing k, for instance $k = 1$, but varying τ for four different proposed nanostructures. Numerical results for T are then plotted in Fig. 3.16 for τ ranging from 1 to 5. We observe that the force distributions for all four proposed nanostructures are degenerate at $\tau < 2$. However, the force distribution of the double-walled nanotube falls below the force distribution of the single-walled nanotube, which is linear owing to the linearity assumption embodied in Eq. (3.27). However, the existence of fullerenes inside both the single and the double-walled nanotubes has almost no contribution for the force distribution in the strong force regime, which is demonstrated again in the next sub-section from the Euler-Bernoulli beam equation. Unlike Wang [161], who utilizes molecular dynamics simulation to investigate the torsional stability of the single-walled nanopeapods, we can not predict the rippling effect on the nanotube's surface (decrease in local stability by the incursion of fullerenes inside the single-walled nanotube under torsional load) due to the fact that we assume perfect rigidity of the cylindrical carbon structures in this sub-section.

3.2.2 Buckling of nanopeapods utilizing Euler-Bernoulli beam equation

In this sub-section, we approximate a single-walled nanotube and a single-walled nanopeapod as a one-dimensional beam so that Euler-Bernoulli beam theory can be applied to study the axial bending of such nanostructures. Sapmaz et al. [134] have previously utilized this technique to investigate a doubly clamped suspended single-walled carbon nanotube. However, Sapmaz et al. [134] ignore curvature effects by letting $y(x) \approx 0$ when investigating a buckled nanotube. We comment that the effect of curvature is crucial at the nanoscale, and we incorporate the curvature into the Euler-Bernoulli beam equation for both weak and strong force regimes. Since we investigate the axial bending of the single-walled nanopeapods, the molecular interactions between fullerenes and the nanotube, i.e. F_{vdW} is also incorporated into the total force but negative given by Eq. (3.46). For the case with the inclusion of the curvature, we derive the Euler-Bernoulli beam equation from first principles by utilizing a variational principle, and we utilize a first integral to obtain both semi-analytical solutions and numerical solutions. The elastic energy of this system $W_{el}[y]$, which is derived in Appendix 6.5, is given by

$$W_{el}[y] = \int_0^L \left\{ \frac{1}{2} EI \frac{y''^2}{(1+y'^2)^{5/2}} + T_{tot}[\sqrt{1+y'^2} - 1] \right\} dx, \tag{3.45}$$

where E and I denote the elastic modulus and the inertial moment of the single-walled carbon nanotube, respectively. We note that both molecular potential energy and electrostatic energy could be incorporated in to the total. However, they are constant, which incur no effect on the variational formulation. We utilize x instead of z to avoid z defined later as $y'(x)$. In addition, we assume the linearity of the total force T_{tot} under infinitesimal buckling, which involves the sum of the molecular forces F_{vdW} between fullerenes and the carbon nanotube and the induced external forces T_{ext} resulting from the electrostatic forces caused by the uniform gate voltage

qE_0, is given by

$$T_{tot} = \frac{ES}{L}\int_0^L \left(\sqrt{1+y'^2}-1\right)dx = T_{ext} - F_{vdW}, \tag{3.46}$$

where S denotes the cross section of the nanotube and negative sign represents the internal repulsive force against the applied load. Eq. (3.46) tells us that both electrostatic and van der Waals forces alter y' and eventually change T_{tot}. We note that if we assume that $y' \approx 0$, the Eq. (3.45) and Eq. (3.46) reduce to

$$W_{el}[y] = \int_0^L \left\{\frac{EI}{2}y''^2 + \frac{1}{2}T_{tot}y'^2\right\}dx, \qquad T_{tot} = \frac{ES}{2L}\int_0^L y'^2 dx = T_{ext} - F_{vdW}. \tag{3.47}$$

Case 1: Without curvature

Assuming statistical equilibrium, i.e. constant temperature, we apply the Euler-Lagrange equation (6.43) to Eq. $(3.47)_1$ to obtain the Euler-Bernoulli beam equation

$$IEy'''' - T_{tot}y'' = 0. \tag{3.48}$$

The general solution obtained from Eq. (3.48) can be written as

$$y(x) = C_1 + C_2 x + C_3 \sinh\gamma x + C_4 \cosh\gamma x, \tag{3.49}$$

where $\gamma = \sqrt{T_{tot}/IE}$, C_1, C_2, C_3 and C_4 denote constants of integration. We utilize Dirichlet boundary conditions, i.e. $y(0) = y(L) = 0$, to deduce

$$y(x) = C_1\left\{1 - \frac{1-\cosh\gamma L}{\sinh\gamma L}\sinh\gamma x - \cosh\gamma x\right\}, \tag{3.50}$$

where C_1 can be determined by the maximum buckling displacement y_{max} from experimental data. For simplicity, we normalized C_1 to be 1 and the following constants are adopted; $E = 1.25$ TPa, $r = 0.65$ nm, $L = 81.36$ Å, $I = (\pi r^4)/4$ [134]. Due to the symmetry of the buckled beam, the maximum displacement y_{max}

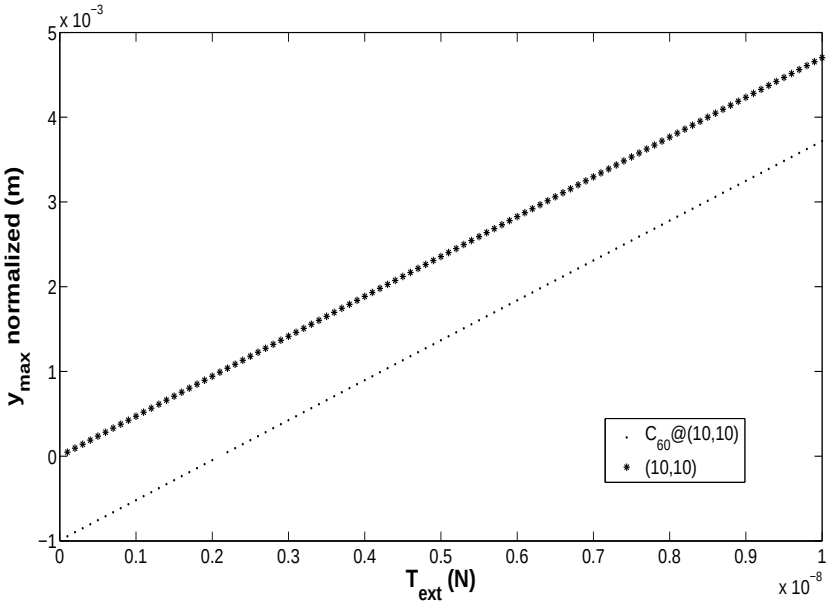

Figure 3.17: Maximum displacement y_{max} as a function of applied force T_{ext} for the approximate case.

is calculated upon letting $x = L/2$. The numerical result for Eq. (3.50) at $x = L/2$ is plotted in Fig. 3.17 for both cases of with and without F_{vdW}. We note that the response of y_{max} relates linearly to the external applied load. This is owing to the fact that the curvature effect is ignored in Eq. (3.50). However, due to the molecular interactions between fullerenes and the host carbon nanotube, residual molecular force is incurred, which causes a reduction in bending of 1×10^{-3} m, even though there is no external force is applied. We note that such bending magnitudes are not physical owing to the fact that we have normalized $C_1 = 1$. Since the difference between the two curves is linear, one may obtain the bending of the single-walled nanopeapods simply by the correction from the results of the single-walled nanotube.

Case 2: With curvature

In this case, we relax the approximation $y' \approx 0$ in Case 1 by incorporating the curvature effect. We start with Eq. (3.45), upon utilizing the first integral, i.e. Eq. (6.45) shown in Appendix 6.7 and simplifying the result with those obtained

from the Euler-Lagrange equation and the symmetry of the buckled beam, we obtain

$$z' = \pm\sqrt{(c + 2\gamma^2\sqrt{1+z^2})(1+z^2)^{5/2}}, \tag{3.51}$$

where $z = y'$ and + and − correspond to concave downwards and concave upwards, respectively. From which, we can transform the differential equation into the integral equation. Now, if we introduce $z = \tan\theta$, then we obtain

$$\frac{\cos\theta d\theta}{\sqrt{c\cos\theta + 2\gamma^2}} = \pm dx. \tag{3.52}$$

Upon making the substitution $\theta = 2\phi$ and integrating both sides with respect to x, we have

$$\frac{4}{k^2}\int_0^{\arctan y'} \sqrt{1 - k^2\sin^2 u}du - \left(\frac{4}{k^2} - 2\right)\int_0^{\arctan y'} \frac{1}{\sqrt{1 - k^2\sin^2 u}}du = \pm\beta x, \tag{3.53}$$

where $k^2 = (2c)/(c + 2\gamma^2)$ and $\beta = \sqrt{c + 2\gamma^2}$. We note that while $c = y''(0)^2 - 2\gamma^2$ can be estimated by the approximate solution, i.e. Eq. (3.50), y' can be numerically determined upon solving Eq. (3.53) for different x. If we further assume Neumann condition, i.e. $y'(0) = y'(L) = 0$, we can solve Eq. (3.53) numerically. However, it is time consuming to solve the semi-analytical solution (3.53) in this way. Instead we utilize Dirichlet conditions and solve Eq. (3.51), which is similar to Eq. (3.25) numerically as given in sub-section 3.1.3 but with the modification of the nanotube length from $2L$ to L.

Upon utilizing the same parameters as given in Case 1, we plot the buckled displacement against x-axis as shown in Fig. 3.18 for the case of the applied force equals to 1×10^{-10} N. We note that the internal van der Waals force due to F_{vdW} resists the bending of the rod in comparison to the bending displacement of the single-walled carbon nanotube under the same applied force. In order to see how the curvature affects the buckling behavior of the proposed systems, we follow Case 1 by plotting the maximum displacement (letting $x = L/2$) from $T_{ext} = 1 \times 10^{-10}$

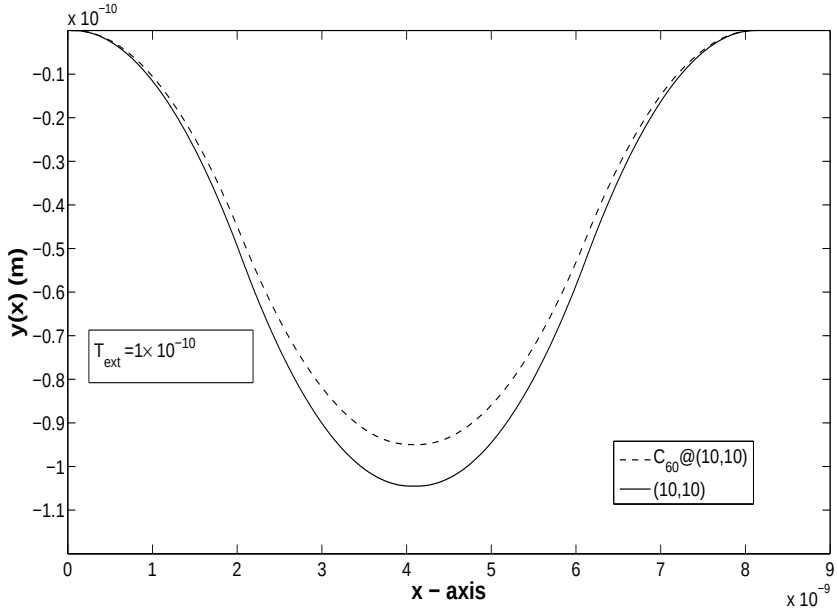

Figure 3.18: Displacements of (10,10) and C_{60}@(10,10) for $T_{ext} = 1 \times 10^{-10}$ N with the corporation of curvature.

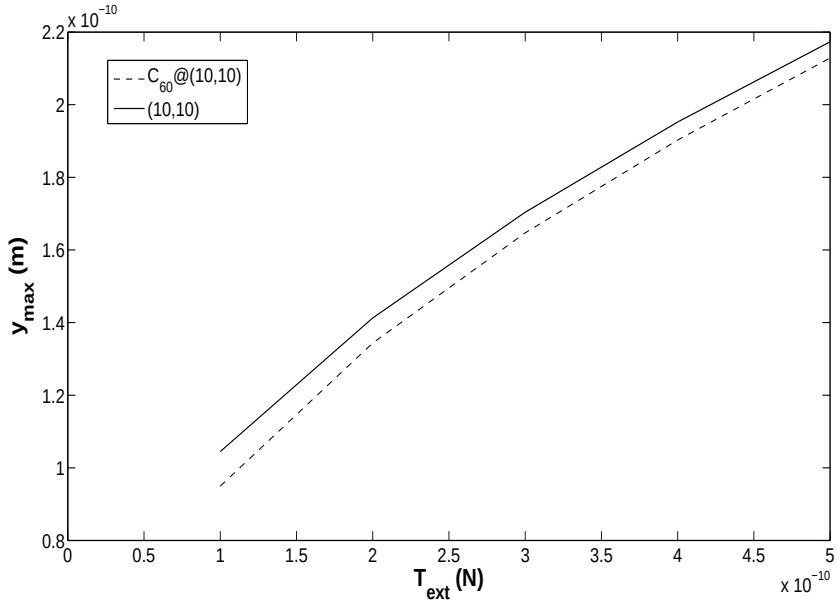

Figure 3.19: Variation of y_{max} with applied force T_{ext} from 1×10^{-10} to 5×10^{-10} N.

N to 5×10^{-10} N and $T_{ext} = 1 \times 10^{-10}$ N to 1×10^{-8} N, as shown in Figs. 3.19 and 3.20. The effect of the internal molecular force can also be observed in Fig. 3.19. Comparing with the case of no curvature effect (see Fig. 3.17), we note that in the low force limit, while the response of y_{max} to the applied external forces is non-linear, y_{max} is linear in the strong force limit, which can be demonstrated in Fig. 3.20

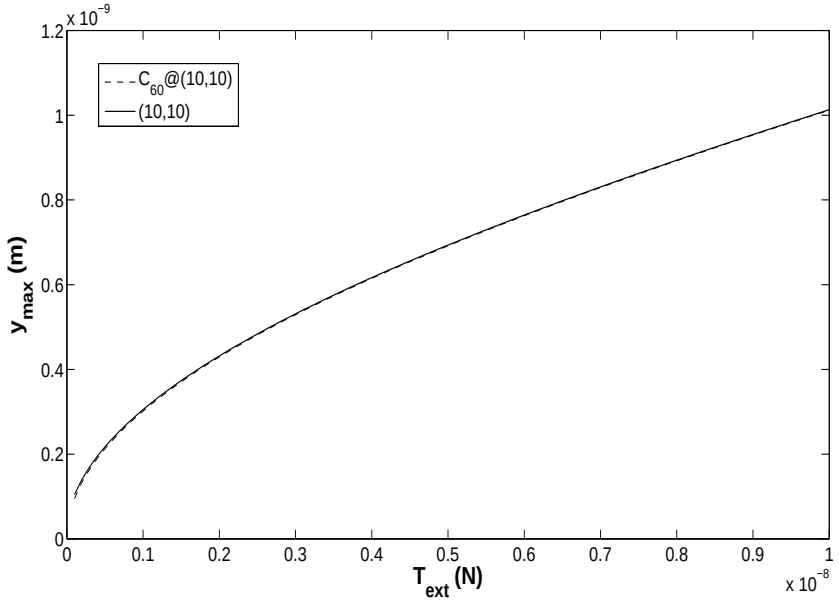

Figure 3.20: Variation of y_{max} with applied force T_{ext} from 1×10^{-10} to 1×10^{-8} N.

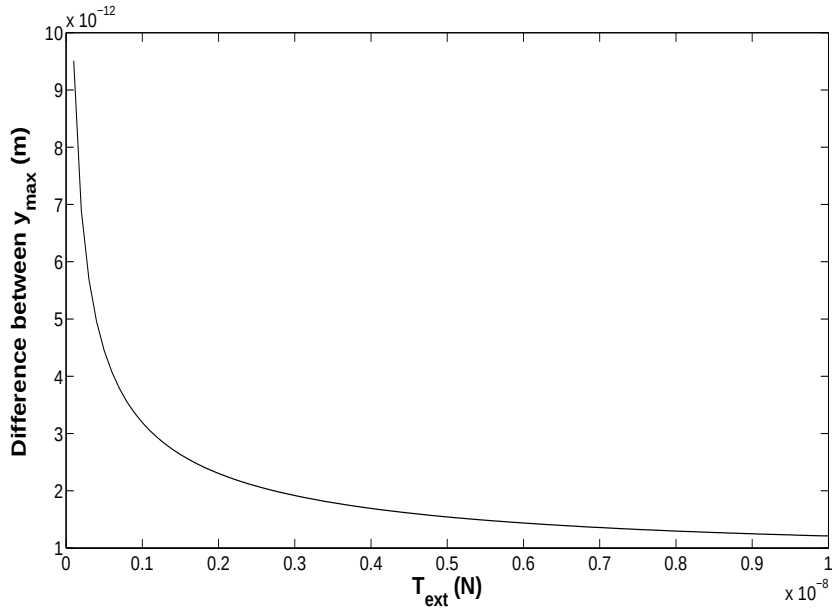

Figure 3.21: Difference between maximum displacements as a function of the applied force T_{ext}.

by raising the applied force up to 10 nN. Such effect is non-linear and as such we cannot deduce the buckling results from the single-walled carbon nanotube to those for the single-walled nanopeapods, especially in the low force limit. In order to find the effect of F_{vdW} on the nanopeapods' buckling, we plot the difference of two displacements in Fig. 3.21, and we observe that the effect of F_{vdW} fades out when

the applied force becomes very large. Given Figs. 3.16 and 3.21, we can conclude that while both internal forces from fullerenes and layers of nanotube contribute to the global buckling phenomenon in the low force regime, only internal force from layers of nanotube counts for the global buckling phenomenon in the strong force regime.

3.2.3 Conclusion

We investigate the buckling of the (10,10), (10,10)@(16,16), the C_{60}@(10,10), and the C_{60}@ (10,10)@(16,16) nanostructures by incorporating the van der Waals molecular potential energies between the various components of the carbon nanotubes. These potential energies are determined analytically from the Lennard-Jones potential and a continuous approach. We find that the critical forces reduce as a result of the molecular interactions between layers of carbon nanotubes and the interactions between fullerenes. The Euler-Bernoulli beam equation is also utilized to obtain the buckling displacement of the (10,10) and C_{60}@(10,10), and we find that while the response to the applied force is linear in the strong force regime, the curvature effect is dominant in the low force limit. In addition, we note that the molecular interactions arising from fullerenes and layers of nanotubes affects the buckling in the low force regime. While the molecular interactions between the layers of the nanotubes has an increasing effect on the buckling with increasing outer nanotube radius, the molecular interactions between fullerenes and nanotubes fades out in the strong force regime. This suggests that the enclosure of fullerenes inside nanotubes might be the sole means of the buckling (e.g. metallofullerene) but insignificantly affects the general buckling phenomenon. Finally, we comment that the study of buckling of nanopeapods, such as the C_{60}@(10,10) and C_{60}@(10,10)@(16,16) structures, may lead to the development of potential nano devices, such as biological sensing, measuring devices for small forces, electric charges or Casimir forces.

3.3 List of Symbols

Section 3.1

$2L$ is the total length of the (6,6) nanotube 72

C_G is the capacitance of the gate voltage 75

$C_{L,R,G}$ are the capacitances of electrodes 73

C^i_j is the capacitance tensor 74

E is the elastic modulus of the nanotube 73

I is the inertial moment of the nanotube 73

K_0 $K_0 = (ne)^2/(4L^2R)$ 76

R is the distance between the electrode and the gate voltage 74

S is the cross-sectional area of the nanotube 73

T is the induced stress 73

T_{total} is the total stress 73

V_i is the electrostatic potential tensor 74

$W_{el}[y]$ is the elastic energy of the system 72

$W_{est}[y]$ is the electrostatic energy of the system 74

W_n is the total energy of the system 75

$c(y)$ is the capacitance of the gate per unit length 73

n is the number of electrons 75

y is the buckling displacement of the buckled nanotube 72

y_n^{max} is the maximum displacement of the buckled nanotube 77

α is the bending moment at the ends of the buckled nanotube 79

ξ $\xi = \sqrt{T/(EI)}$ 77

Section 3.2

A is the attractive constant 95

B is the repulsive constant 95

D are the bending stiffness of the carbon nanotube 91

E is elastic modulus of the nanotube 91

E^* is the potential energy between a fullerene and an atom on the carbon nanotube 94

E_0 is the strength of the applied electric field 91

$F_{vdW}(z)$ is the van dar Waals force 90

I is the inertial moment of the single-walled carbon nanotube 102

L is the length of the nanopeapods 92

N_z is the axial force 91

$N_{z\theta}$ is the shear membrane force 91

N_θ is the circumferential membrane force 91

R is the radius of the nanotube 91

$\overline{R}$ $\overline{R} = (R_1 + R_2)/2$ 93

R_i is the radius of the ith layer 89

S is the cross section of the nanotube 103

T is the net applied axial force 91

T_c is the critical force 97

T_{tot} is the total external force 102

$W_{el}[y]$ is the elastic energy of the system 102

b is the radius of the C_{60} fullerene 95

c_i is the linearity constant for the ith layer 90

dS_f is the surface element of the fullerene 95

d_{cc} is the carbon-carbon bond length 90

h is the thickness of the nanotube 91

k is the axial wave number 92

n_f is the surface density of of the fullerene 95

$p_{i,j}$ is the pressure exerted from the jth layer to the ith layer 89

$p(z, \theta)$ is the van der Waals pressure between molecules 91

p_{vdW} is the van dar Waals pressure 90

q is the total charge 91

y_{max} is the maximum buckling displacement 103

$y(x)$ is the displacement of the buckled nanotube or nanopeapod 102

Δp_i is the incremental pressure of the ith layer 89

α $\alpha = (k\pi)/L$ 92

γ $\gamma = \sqrt{T_{tot}/IE}$ 103

ρ is the distance between the carbon atom on the nanotube and an atom on the fullerene 95

τ is the circumferential wave number 92

ω_i is the displacement of the ith layer 90

Chapter 4

Worm-like chain model and applications

In this chapter, we re-examine the worm-like chain model from the perspective of a variational principle. Some extra information, namely that of the free energy and the cut off force of a stretched molecule, are newly defined. In addition, we apply Hooke's law and the worm-like chain model to investigate the molecular stretching in the extracellular matrix and find that the toughness of the connective tissue is intimately related to the microscopic characteristics of the anionic glycosaminoglycan.

4.1 Force-extension formula for the worm-like chain model from a variational principle

A force-extension relationship for some biomacromolecules can be experimentally measured by stretching a single molecule, utilizing either an atomic force microscope [22, 67] or an optical tweezer [153], and the force-extension curves can be theoretically predicted from models of semi-flexible polymers. Butt et al. [22] provide an excellent review on the force measurements utilizing an atomic force microscope.

The freely-jointed chain (FJC) model and the worm-like chain (WLC) model [160] are commonly utilized to describe semi-flexible polymers and a good introduc-

tion of these two models can be found in Storm et al. [152]. While the WLC model describes an isotropic and homogeneous rod that is continuously flexible, the FJC model discretizes the molecule into Kuhn segments, which are unbendable, completely straight and can only rotate around the joints. Therefore, in comparison to the FJC model, the WLC model provides better predictions for the force and extension relationship of stiffer polymers like single-stranded DNA, unstructured RNA and polypeptides. In addition, an extensible WLC model has also been proposed for an enthalpic region where deterministic mechanics takes place [160]. Both interpolation formulae and exact solutions for the WLC model have been previously obtained [97, 160]. However, an exact solution can only be determined numerically due to the fact that a variational parameter has to be minimized for any given force [97, 152]. Recently, [152, 127] attempt to seek an exact solution utilizing the FJC model. Such a solution would provide a good mathematical basis for the incorporation of the ring conformational transitions because each segment can be easily scaled with a preferred monomer's length . In this section, the WLC model is utilized and the calculus of variations is employed to determine an analytical force-extension formula for the WLC model, which turns out to be expressed in terms of elliptic integrals.

The section is structured as follows. In sub-section 4.1.1, the WLC model is introduced, which is followed by the derivation of an analytical force-extension formula of the WLC model utilizing variational principle in sub-section 4.1.2. In subsection 4.1.3, the possible phase changes of the molecule undergoing an external applied force are examined, while in sub-section 4.1.4 our new force-extension formula is compared with some recent experimental data. In the final sub-section, a summary and some general conclusions are made.

4.1.1 Worm-like chain model

The WLC model was first introduced by Fixman and Kovac [43] and after a preliminary analytical approach by Kovac and Crabb [82], a comprehensive treatment

was given by Marko and Siggia [97]. The WLC model has some advantages over the FJC model; for example, the best-fit value of the Kuhn segment for a typical double-stranded DNA from utilizing the FJC model is approximately 100 nm, which is completely different from its physical contour length per base pair of 0.34 nm, and the FJC model provides a poor prediction over the intermediate-force region. Therefore, we choose to examine the WLC model instead of the FJC model. We note that the WLC model can be thought of as a limiting case of the FJC model when the Kuhn segment length approaches zero. Since there are different versions of the force-extension formulae for the WLC model, the interpolation solution [97], which is most commonly utilized by biologists and chemists to fit their experimental data, is given by

$$\frac{fA}{k_BT} = \frac{z}{L} + \frac{1}{4(1-z/L)^2} - \frac{1}{4}, \tag{4.1}$$

where f, A, k_B, T, z and L denote the applied external force, the bending stiffness of the molecule, the Boltzmann's constant, the absolute temperature, the extension of the molecule and the total molecular contour length respectively. This interpolation formula provides a good fit for most of the experimental data. However, it has up to 6% error when compared to the exact solution in an intermediate-force regime.

4.1.2 An analytical force-extension formula for the WLC model by utilizing the variational principle

In this sub-section, we assume that a molecule behaves like an isotropic and homogeneous rod. The effective energy of the stretched molecule W can be expressed as an integral of the segmental bending energy, $Ak_BT\kappa^2/2$ over the entire polymer curve, constrained by the external force f for end to end extension as given by [43, 172]

$$W = \int_0^L \left\{ \frac{Ak_BT}{2}\kappa^2 - f\cos\theta \right\} ds, \tag{4.2}$$

where κ is the principal curvature of the molecule. We comment that while the first term inside the integration is the usual strain energy, the second term corresponds to the work done performed by the external force during stretching, which can be viewed as Lagrangian multiplier (constraint) in mathematical sense. Unlike previous statistical mechanical approaches; for example those adopted by Marko and Siggia [97], they derive a partition function from the Boltzmann distribution for a given elastic energy. Upon minimizing the eigen-energy obtained from the partition function, useful information such as the extension can be naturally extracted, here we utilize a variational principle approach to examine analytically the minimum energy configuration of a stretched molecule by incorporating all possible orientations of the monomers under thermal equilibrium to determine the force-extension formula for the WLC model. The displacement vector $\boldsymbol{R}$ of a molecule is firstly parametrized by its arc length $s \in [0, L]$ (see Fig. 4.1 for details). Since all possible orientations of each monomer can be projected onto a unit sphere, the principal curvature can be further parametrized by the polar angles (θ, ϕ). That is,

$$x = \sin\theta\sin\phi, \quad y = \sin\theta\cos\phi, \quad z = \cos\theta. \tag{4.3}$$

Given the relationship of the Cartesian coordinate system in terms of the usual spherical coordinate system, the unit tangential vector $\hat{\boldsymbol{t}}$ and the principal curvature κ can be shown to be

$$\hat{\boldsymbol{t}} = (\sin\theta\sin\phi, \sin\theta\cos\phi, \cos\theta), \qquad \kappa^2 = |\frac{\partial\hat{t}}{\partial s}|^2 = \dot{\phi}^2\sin^2\theta + \dot{\theta}^2, \tag{4.4}$$

where $\dot{\theta}$ and $\dot{\phi}$ denote $d\theta/ds$ and $d\phi/ds$, respectively. Substituting Eq. (4.4) back into Eq. (4.2), gives

$$W = \int_0^L \left\{ \frac{Ak_BT}{2} \left(\dot{\phi}^2 \sin^2\theta + \dot{\theta}^2 \right) - f\cos\theta \right\} ds, \tag{4.5}$$

where the functional F can be extracted from Eq. (4.5) to give

$$F = \frac{Ak_BT}{2}(\dot{\phi}^2 \sin^2\theta + \dot{\theta}^2) - f\cos\theta. \tag{4.6}$$

The two independent Euler-Lagrange equations for θ and ϕ are easily obtained from

$$\frac{\partial F}{\partial \theta} = \frac{d}{ds}\frac{\partial F}{\partial \dot{\theta}}, \qquad \frac{\partial F}{\partial \phi} = \frac{d}{ds}\frac{\partial F}{\partial \dot{\phi}}. \tag{4.7}$$

The functional, which is given in Eq. (4.6), can then be substituted into Eq. (4.7), to obtain

$$\ddot{\phi}\sin^2\theta + 2\dot{\theta}\dot{\phi}\sin\theta\cos\theta = 0, \qquad \ddot{\theta} = \dot{\phi}^2\sin\theta\cos\theta + \mu\sin\theta, \tag{4.8}$$

where μ denotes $f/(Ak_BT)$. From Eq. (4.8), one possible solution is given by $\sin\theta = 0$, which gives rise to trivial solutions. Therefore, assuming $\sin\theta \neq 0$ leads us to the following integrals

$$\dot{\phi} = \frac{c_1}{\sin^2\theta}, \qquad \dot{\theta}^2 = -\frac{c_1^2}{\sin^2\theta} - 2\mu\cos\theta + c_2, \tag{4.9}$$

where c_1 and c_2 are constants of integration. In terms of classical mechanics, c_1 and c_2 can be regarded as the conservation of the "angular momentum" and the

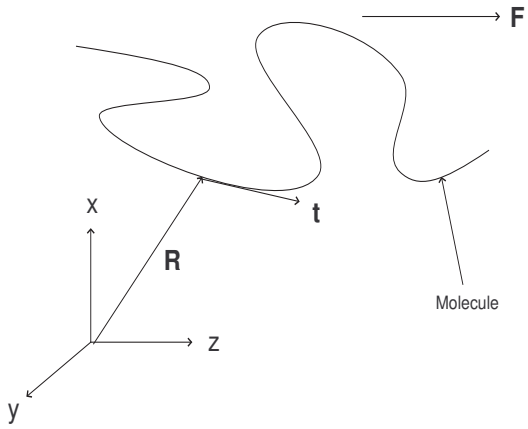

Figure 4.1: Worm-Like Chain model. An external force is applied to the molecule in the z-direction. The position vector of each monomer is parametrized by s with tangential vector $\boldsymbol{t}(s)$.

conservation of the "total energy" respectively. In addition, we note that Eq. (4.9) resembles the mathematical description of a spinning heavy top with one point fixed on the ground [49].

To proceed, given Eq. (4.9), $\dot{\phi}$ and $\dot{\theta}$ can be substituted back into Eq. (4.5) to obtain

$$W = -2\int_0^L f\cos\theta ds + \frac{c_2 A k_B T L}{2}. \tag{4.10}$$

As an aside, it is evident from Eq. (4.10) that the free energy, which is defined by the total energy required to stretch the molecule from its relaxed state to its total contour length, is given by $(aAk_BTL)/2$, where a is set equal to c_2, which is evaluated at $\mu = 0$ and is an invariant constant. Now, we define I as

$$\begin{aligned} I &= -2\int_0^L f\cos\theta ds = -2\int_0^\pi \frac{f\cos\theta}{\dot{\theta}} d\theta, \\ &= \mp\lim_{\epsilon\to 0}\int_\epsilon^{\pi-\epsilon} \frac{2f\sin\theta\cos\theta}{\sqrt{-c_1^2 - 2\mu\cos\theta\sin^2\theta + c_2\sin^2\theta}} d\theta, \end{aligned} \tag{4.11}$$

where the second equality in Eq. (4.11) is achieved when the coordinate system is

transformed from the arc-length reference frame into the angular reference frame, and then θ is integrated from zero to π so as to sum all possible orientations of the monomers under thermal equilibrium T in the entropic regime. In addition, when θ approaches either zero or π, c_1 has to be sufficiently small in order to ensure that the integral remains real, which leads to the conclusion that $c_1 = 0$ and therefore Eq. (4.11) is further reduced to

$$I = \mp \int_0^{\pi} \frac{2f\cos\theta}{\sqrt{c_2 - 2\mu\cos\theta}} d\theta. \tag{4.12}$$

This equation is found to be integrable in terms of complete elliptic integrals of first and second kinds, where a basic treatment of elliptic integrals can be found in [17]. We note that the positive sign of Eq. (4.12) has been taken to carry on our investigation. It can be shown that Eq. (4.10) becomes

$$W(f) = 2Ak_BT\left\{\sqrt{c_2 - 2\mu}E\left[k(f)\right] - \frac{c_2}{\sqrt{c_2 - 2\mu}}K\left[k(f)\right] + \frac{c_2 L}{4}\right\}, \tag{4.13}$$

where $k^2(f) = -4\mu/(c_2 - 2\mu)$, $K = \int_0^{\pi/2} 1/\sqrt{1 - k^2\sin^2 x}dx$ is the complete elliptic integral of the first kind and $E = \int_0^{\pi/2}\sqrt{1 - k^2\sin^2 x}dx$ is the complete elliptic integral of the second kind. In addition, the effective energy W must not become complex, which forces $c_2 > 2\mu$, where this inequality gives rise to the cut-off force of the stretched molecule and the possible phase changes of the molecule, which will be discussed later. Adopting the same approach from Lai et al. [87], we may determine c_2 utilizing a boundary condition that the molecule is fixed on the attached substrate and is free on the other end

$$c_2 = b\mu + a, \tag{4.14}$$

where a and $-2 \leq b \leq 2$ are real constants. Thus, Eq. (4.14) can be interpreted as the total energy of the system, which is interpreted by the modification of its ground energy a by the work done $b\mu$, and this technique has also been employed by Haverkamp et al. [54] in their study of the ring conformational transitions by modifying the Gibbs energy with an additional work term. Given that, c_2 is substituted back into Eq. (4.13) to get

$$W(f) = 2Ak_BT\left\{\sqrt{a-(2-b)\mu}E\left[k(f)\right] - \frac{(a+b\mu)}{\sqrt{a-(2-b)\mu}}K\left[k(f)\right] + \frac{L(a+b\mu)}{4}\right\}, \tag{4.15}$$

where $k^2 = -4\mu/[a-(2-b)\mu]$. Since the effective energy is expressed entirely in terms of the function f, one may find the extension z of the molecule by utilizing

$$z = -\frac{\partial W}{\partial f}, \tag{4.16}$$

which gives

$$z = \frac{(2-b)(2+b)\mu - ab}{\sqrt{a-(2-b)\mu}[a+(b+2)\mu]}E(k) + \frac{b}{\sqrt{a-(2-b)\mu}}K(k) + \xi(\delta T), \tag{4.17}$$

where $\xi(\delta T)$ denotes the error due to thermal fluctuations, which will be addressed in sub-section 4.1.4 but is found to be neglectable. To achieve the above equation, the following elliptic integral identities have been utilized [167], namely, $dE/dk = (E-K)/k$ and $dK/dk = E/\left[k(1-k^2)\right] - K/k$. Note that Eq. (4.17) is compatible with equation (2) obtained by Neumann [106] for his study on the polymer stretching under an homogeneous elongational flow, especially the singularity under the square root. We observe that z approaches zero when μ approaches zero; Hooke's Law is re-discovered in the low-force limit; and z possesses a non-linear effect such that

z approaches L with a distinctive $1/f^{1/2}$ behavior [82], which constitute a special characteristic of the WLC model. The above equation can then be easily extended into the extensible WLC model by releasing the elasticity of the molecule. That is,

$$z = \frac{(2-b)(2+b)\mu - ab}{\sqrt{a-(2-b)\mu}[a+(b+2)\mu]}E(k) + \frac{b}{\sqrt{a-(2-b)\mu}}K(k) + \frac{f}{\Phi}, \tag{4.18}$$

where Φ is the modulus of elasticity.

Upon comparing Eq. (4.17) with the interpolation formula given in Eq. (4.1), we see that apart from the bending stiffness A, two extra parameters a and b need to be fitted utilizing experimental data. In particular, these extra parameters can be determined by matching experimental data in the low and high forces regimes. For the low forces limit, where up to the first order of $b\mu$ is considered, Eq. (4.17) reduces to Hooke's Law. That is,

$$f = \frac{4\sqrt{2}Ak_BT}{\pi a^2}z. \tag{4.19}$$

While for the high forces limit, one may obtain

$$L = \frac{(2-b)(2+b)\mu_c - ab}{\sqrt{a-(2-b)\mu_c}[a+(b+2)\mu_c]}E(k_c) + \frac{b}{\sqrt{a-(2-b)\mu_c}}K(k_c), \tag{4.20}$$

where $\mu_c = f_c/(Ak_BT)$ and $k_c^2 = -4\mu_c/[a-(2-b)\mu_c]$. We refer the reader to Eq. (4.21) for the definition of f_c. The new exact force-extension formula has more degrees of freedom than the interpolation formula given in Eq. (4.1), and as such it is expected to produce more accurate results in comparison to the naive interpolation formula. For example, a relates to "the ground energy"; b is related to the tendency of the molecule to lie towards the z-axis and hence affects the force-extension curve in the high force regime; and most importantly, the newly derived force-extension

formula predicts the cut-off force, which is defined as the force that is required to stretch a molecule into its total contour length, but is absent in the interpolation formula. The asymptotic solution of the interpolation formula implies the utilization of an infinite applied force to stretch a molecule into its total contour length. It is easy to observe from Eq. (4.17) that the cut-off force is defined as

$$f_c = \frac{aAk_BT}{2-b}. \tag{4.21}$$

We note that this cut-off force is equivalent to the case of $c = 1$ introduced in Neumann [106] where $0 \leq c < 1$ while determines the entropic regime, $c \geq 1$ determines the enthalpic regime. We also note that the linear dependence of f_c in temperature and the existence of the singularity are compatible with the simple derivation of the new molecular model, i.e. equation (5), introduced by Misof et al. [101] for his study of stress-strain relationship for a collagen pair. That is, $\sigma = K\epsilon/(1-\epsilon/\epsilon_0)$, where σ and ϵ denote stress and strain of the collagen pair respectively. Readers are referred to the definition of the constants K and ϵ_0 in Misof et al. [101] but note that K depends linearly on temperature. It is easy to observe from Eq. (4.21), and the constraint for b, that the minimum cut-off f_c^{min} force is given by

$$f_c^{min} = \frac{aAk_BT}{4}. \tag{4.22}$$

4.1.3 Phase changes of a stretched molecule

In this sub-section, the Euler-Lagrange equations, Eq. (4.9), are utilized to obtain some observation that the mathematics suggests the possibility of phase changes existing in such molecules, which has also been previously investigated by Fain et al.[40] for their study on, in particular the conformations of linear DNA and

separately confirmed by a molecular dynamic calculation performed by Kuttel et al. [85]. In our study, two phase changes of the molecule's configuration are predicted to occur when it is stretched beyond its total physical contour length L. To derive the phase change of the molecule, the second equation of Eq. (4.9) is rearranged to obtain

$$(\dot{\theta}\sin\theta)^2 = -c_1^2 - 2\mu\cos\theta\sin^2\theta + c_2\sin^2\theta, \tag{4.23}$$

so that upon making the substitution $x = \cos\theta$, Eq. (4.23) becomes

$$\dot{x} = \pm\sqrt{-c_1^2 - (1-x^2)(2\mu x - c_2)}, \tag{4.24}$$

which is separable. Thus after rewriting, Eq. (4.24) becomes

$$\frac{dx}{\sqrt{-c_1^2 - 2\mu x(1-x^2) + c_2(1-x^2)}} = \pm ds, \tag{4.25}$$

where if $c_1 = 0$, then Eq. (4.25) is further simplified to

$$\frac{dx}{\sqrt{(x-1)(x+1)(x-c)}} = \pm\sqrt{2\mu}ds, \tag{4.26}$$

where $c = c_2/(2\mu)$. Physically, Eq. (4.26) is a special case of the governing equations of a spinning top, which describes what is called a vertical top, as the locus lies between 0 and π, and covers the entire surface of a sphere S^2. Upon integrating Eq. (4.26), we obtain

$$\int \frac{dx}{\sqrt{(x-1)(x+1)(x-c)}} = \pm\sqrt{2\mu}s + C, \tag{4.27}$$

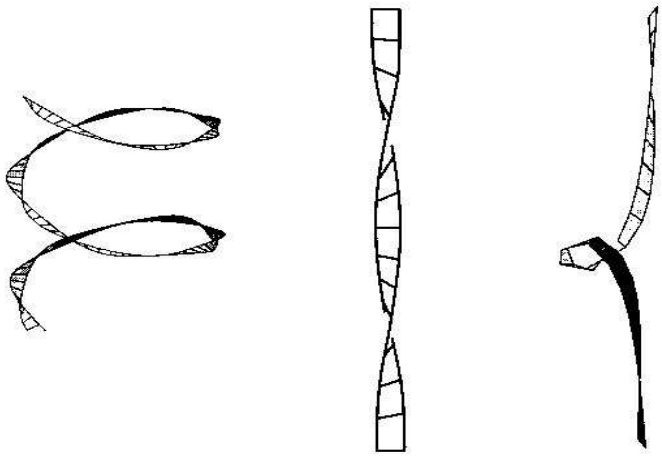

Figure 4.2: Schematic of super-helix, soliton and twisted vertical lines are shown from left to right.

where C is a constant of the integration, which may be complex depending on the value of c. Since the polynomial under the radical is a cubic, Eq. (4.27) is integrable in terms of elliptic integrals. Solutions for both the non-degenerate case (three distinct real roots) and the degenerate case (double roots) are presented below.

The non-degenerate case (i.e., $c \neq -1, 1$):

$$-\frac{2}{\sqrt{c-1}} \int \frac{d\theta}{\sqrt{1-k^2 \sin^2 \theta}} = -\frac{2}{\sqrt{c-1}} F = \pm\sqrt{2\mu} s + C, \tag{4.28}$$

where a substitution of $x = \cos\theta$ has been made to obtain the above equation and F is the incomplete elliptic integral of the first kind with $k^2 = 2/(1-c)$. Note that s is complex when $c < 1$, which gives rise to a spiral structure.

The degenerate case (i.e., $c = 1$ and -1):

$$\mp\sqrt{2} \tanh^{-1}\left(\sqrt{\frac{x \pm 1}{2}}\right) = \pm\sqrt{2\mu} s + C, \tag{4.29}$$

where the $\pm$ correspond to $c = \pm 1$. This solution is obtained by examining the derivative of the tanh function. When the applied force increases from 0 to infinity, c decreases from the infinity towards $b/2 \in [-1, 1]$. It is interesting to observe that when $c > 1$, the solution in Eq. (4.28) represents a super-helix, while if $c = 1$, then the solution in Eq. (4.29) is a soliton, and finally for $-1 < c < 1$, the solution in Eq. (4.28) corresponds to a twisted vertical line (see Fig. 4.2 for details). Hence the driving force f changes the general structure of the stretched molecule gradually and creates phase changes for the stretched molecule. However, whether a given molecule will undergo all these phase changes (i.e., from a super-helix to a soliton and then to a twisted vertical line), just one (i.e., from a super-helix to a soliton), or none (i.e., remains in the super-helix) depends entirely on the cut-off force f_c, which is derived in Eq. (4.21). It is not obvious that all molecules must undergo two phase changes when they are stretched beyond their total contour lengths. In the following, we derive criteria for which these phase changes take place. It is obvious that all molecules must start from the super-helix when $\mu = 0$.

For a molecule with no phase changes:

In this case, a molecule remains in the initial super-helix configuration and the root c has to be greater than 1. This requires that

$$c = \frac{aAk_BT}{2f} + \frac{b}{2} > 1,$$

After rearrangement, the above inequality becomes

$$f < \frac{aAk_BT}{2-b} = f_c. \tag{4.30}$$

Therefore, the molecule undergoes no phase change before it is fully stretched into its total contour length.

For a molecule with one phase change:

In this case, one phase change takes place from a super-helix to a soliton, for which the root c must be equal to 1. Following the same line of the argument as the first case, we find that

$$f = \frac{aAk_BT}{2-b} = f_c. \tag{4.31}$$

Therefore, the molecule undergoes one phase change when it is exactly stretched into its contour length.

For a molecule with two phase changes:

In this case, the root c is smaller than one and the following inequality is held

$$f > f_c. \tag{4.32}$$

Hence, the molecule undergoes another phase change from a soliton to a twisted vertical line while it is stretched beyond its contour length, which implies that all molecules have to undergo two phase changes after entering into the enthalpic regime. From further examination of the definition of the constant c, the critical force f_s for the phase change is related to the critical angle θ_s as follows

$$f_s = \frac{aAk_BT}{2(1-\cos\theta_s)}, \tag{4.33}$$

and this result can be checked by the available experimental results. It is worth noting that all of the criteria derived so far ignore the existence of external forces from thermal fluctuations, which could affect the outcome. Until now, one question still remains open: Can we possibly have a case that $c = -1$? For this to occur, b

must be equal to -2 and the molecule has to be stretched into its total contour length by an infinite external force, which corresponds to a nonphysical outcome from the interpolation formula. However, for a very stiff molecule, a phase change from a vertical twisted line into a stiff vertical twisted line might occur. These results for phase changes need to be checked by molecular stretching experiments.

4.1.4 Numerical results

In this sub-section, the new force-extension formula for the WLC model is employed to fit some recent force-extension data of the response of the polysaccharide hyaluronan given by Haverkamp et al. [55]. Our newly derived force-extension formula has been fitted to this data, where the outcome is reported in Fig. 4.3 and Fig. 4.4 with the domains of the applied force ranging from 0 nN to 0.7 nN and 0 nN to 8 nN correspondingly. Note that the extensions in both Fig. 4.3 and Fig. 4.4 have been normalized by the total contour length L, which is assumed to be equal 76 nm. We utilize the new extensible WLC model, i.e. Eq. (4.18), to fit the data.

According to the results coming from the curve-fitting (we first fit the curve at the low force regime to obtain Ak_BT and a and b is obtained by examining the curve at the high force regime by fixing the values of Ak_BT and a), the best fitted value of Ak_BT and Φ are given by 2.3×10^{-25} m^{-1} and 2.9×10^{-2} Nm^{-1} respectively. In addition to the existing parameter Ak_BT and Φ, two new parameters a and b have been introduced in the new force-extension formula, which in this case are equal to 6.5×10^{14} Nm and 1.982 respectively. The parameter "A" is traditionally referred to as the stiffness of the polysaccharide, while the new parameter a corresponds to "the ground energy". Hence, a and Ak_BT combine to give the free energy, as derived previously in this sub-section, i.e. $aAk_BTL/2$. Given the fitted values of a and A, the free energy can also be verified from the force-extension curve. That is, the energy that is put into the system to stretch the molecule from the relaxing state to its total contour length, can be approximated by taking the area under the un-normalized force-extension curve from Fig. 4.3, gives 7.1×10^{-18} J, which is

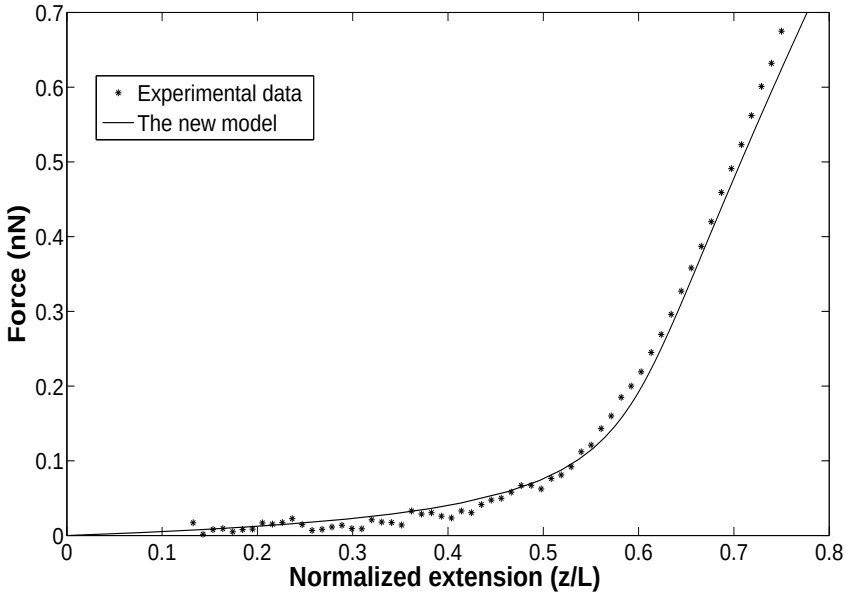

Figure 4.3: The fitting of the new force-extension formula with the experimental data. The applied force ranges from 0 nN to 0.7 nN and the extension has been normalized by its total contour length L, which is equal to 75.85 nm.

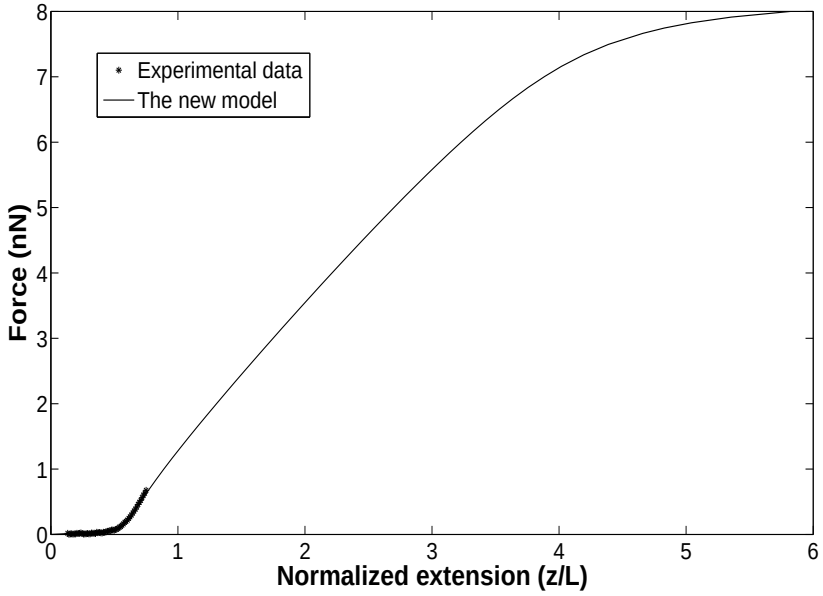

Figure 4.4: The fitting of the new force-extension formula with the experimental data. The applied force ranges from 0 nN to 8 nN.

comparable with the free energy calculated theoretically by $aAk_BTL/2 = 5.7\times10^{-18}$ J.

To determine the full features of this force-extension curve, the z-domain of the force-extension curve is extended from the total contour length L to $6L$, which is

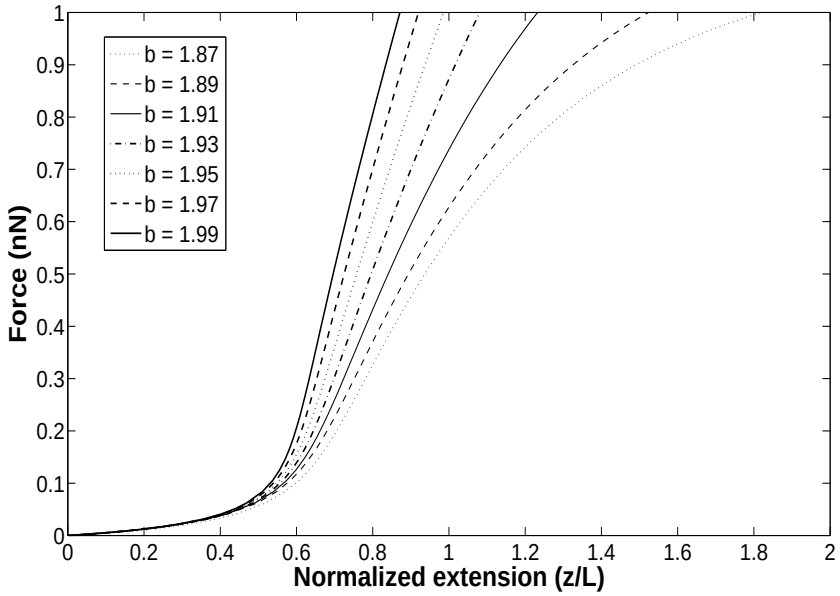

Figure 4.5: A force-extension curve of the WLC model with $b = 1.87, 1.89, ..., 1.99$ with an increment of 0.02, which correspond to the curves from bottom to top respectively.

shown in Fig. 4.4. The cut-off force, which results from the singularity of the force-extension formula, can be observed in Fig. 4.4. This cut-off force occurs when the applied force is around 8 nN and can be directly obtained upon utilizing Eq. (4.21). The same phenomenon can also be demonstrated in Figure 1 of Neumann [106]. We note that this value is substantially larger than the usual value of maximum bond stretching forces, which is around 2 nN [98]. However, the new model does predict the cut-off force in the right magnitude and we don't have sufficient experimental data for curve fitting in the very high forces regime. Finally, the physical meaning of b can be determined by varying b while keeping the other parameters constant. Values ranging from 1.87 to 1.99 with an increment of 0.02 have been chosen because they reflect the wide spectrum of deflection curves in the high-force regime. Note that very low values of b correspond to Hooke's law in all regimes whereas very large values of $b \approx 2$ correspond to the fracture of the molecule in the high-force regime. The numerical results are plotted in Fig. 4.5. Apparently, b affects the stretching behavior of the molecule in the high-force limit, while keeping the stretching behavior of the molecule in the low-force limit almost intact (see

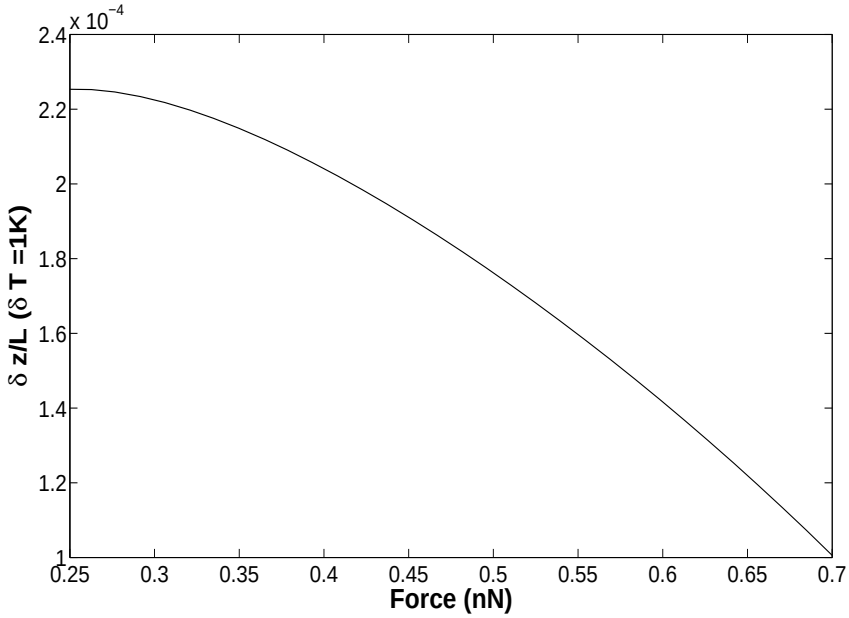

Figure 4.6: Error analysis of the new force-extension formula subject to thermal fluctuations.

Eq. (4.19) for string constant in the low forces regime). Mathematically, according to Eq. (4.14), b affects the amount of work done arising from the applied force put into the system, and therefore b becomes decisive in the high-force limit when the entropy of the system is essentially removed. In particular, the new force-extension formula suggests a family of force-extension curves in the high-force regime, where the new formula covers almost all possibilities of the deflection of the force-extension curve in this limit by choosing different values of b, and this property makes our new formula more powerful than previous interpolation formulae in capturing the mechanical behavior of molecules in the high-force regime.

Finally, we investigate the error of our new force-extension formula subject to thermal fluctuations, i.e. we consider the change of temperature $T \to T + \delta T$ leading to the change of extension $z \to z + \delta z$. A simple mathematical deviation gives $\delta z = (\partial z/\partial T)\, \delta T$. Upon using the same values of parameters given in this sub-section and assuming that $\delta T = 1\text{K}$, we numerically obtain the relative error in the extension, i.e. $\delta z/L$, which is plotted in Fig. 4.6. As the numerical result for the instability suggests, extension in our new formula does not respond sensitively within $\delta T = 1\text{K}$ for most of the force regimes, and the relative error of extension

decreases while the applied force increases as the stretching approaches the enthalpic regime.

4.1.5 Conclusion

In this section, a new analytical force-extension formula for the WLC model is determined by minimizing the effective energy of the molecule by the variational principle. We have utilized the new formula to predict additional physical parameters such as expressions for the free energy and the cut-off force of the stretched molecule, which are absent in the existing interpolation formula. In addition, the new force-extension formula predicts phase changes of the stretched molecule and anticipates that all molecules must undergo two phase change, i.e. changing from a super-helix to a soliton, from a super-helix to a soliton and then from a soliton to a vertical line, after they are entering into the enthalpic regime. The new force-extension formula is then utilized to fit some recent experimental data. However, in the future more work needs to be undertaken to incorporate a Boltzmann energy distribution into the model to account for the effect of thermal fluctuations.

4.2 Mechanical model for a collagen fibril pair in the connective tissue extracellular matrix

Numerous computational and continuum mechanical methodologies have been utilized to study the mechanics of such connective tissue (CTs) [121, 2, 45, 57, 68, 70, 81, 162]. However, most tend to ignore the microscopic details of CTs or assume a simple form of the molecular potential energy in order to make their models tractable. In particular, for a continuum mechanical approach, generally a homogeneous structure of CTs is assumed. Since the CTs comprise of collagen pairs, here we adopt basic physical concepts and simple mathematical techniques to investigate the mechanical properties of a single collagen pair. While utilizing a quadratic energy form for the collagen, we incorporate the statistical nature of anionic glycosamino-

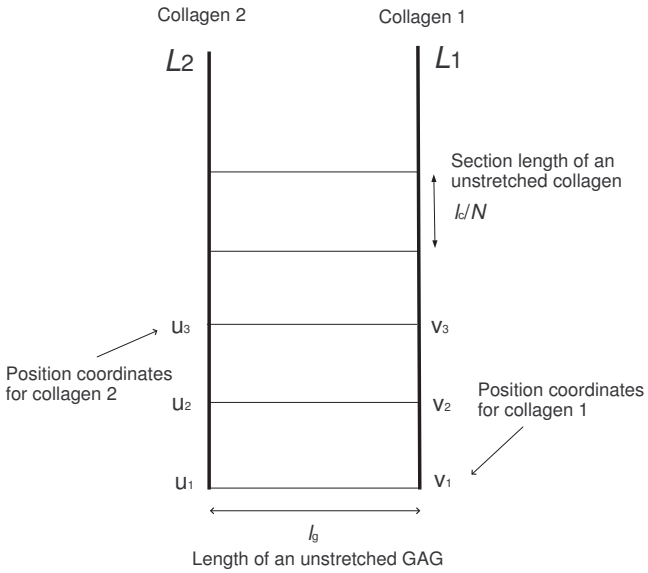

Figure 4.7: Collagen pair before stretching, where L_1 and L_2 denote the collagens 1 and 2 respectively, $v_1 \dots v_N$ and $u_1 \dots u_N$ denote the position coordinates of oligomers in L_1 and L_2 respectively, l_c and l_g are the natural lengths of the collagens and GAGs respectively and N is the total number of oligomers that could exist in each collagen.

glycan (GAGs) into our model by utilizing the worm-like chain model, which has both theoretically and experimentally been proved to be applicable to wide ranges of bio-macromolecules including unstructured DNA, RNA, GAGs and polysaccharide [55, 11, 124, 123, 112]. We note that our work may form a theoretical basis for experimentalists for their work on collagen pairs.

This section is divided into four sub-sections. In sub-section 4.2.1, we derive a mathematical model for CTs, while in sub-section 4.2.2, numerical results and some extension work on CTs are developed. In the last sub-section, we present some conclusions.

4.2.1 Theory

In this sub-section, we consider some simple applied mathematical models for a collagen pair. Since CTs contain repeated units of collagen pairs, a collagen pair is denoted by a single unit of such repeated collagen pairs, which is illustrated in Fig. 4.7. While we model collagens utilizing Hooke's law, GAGs are modeled

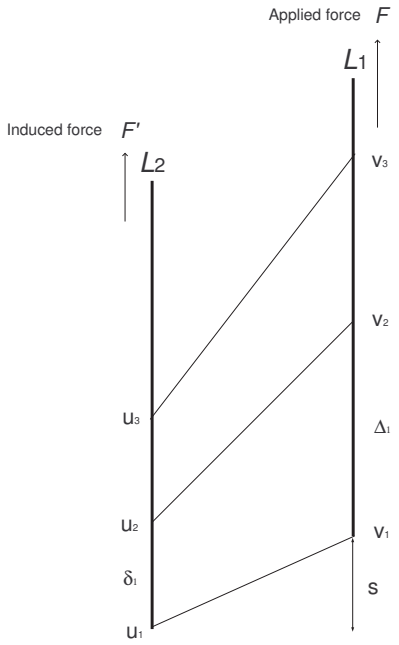

Figure 4.8: Collagen pair after stretching, by an applied force F assumed to be acting on L_1 causing an induced force F' in L_2, while s denotes the offset length between L_1 and L_2, Δ_1 and δ_1 denote the length of the first oligomer in L_1 and L_2 respectively and so on.

utilizing the worm-like chain model, which has carefully taken the entropic nature of the molecular chain into account. Due to the symmetry of CTs, we consider a pair of collagens with axial and regular GAGs in between, especially bone. In reality, to assemble such segments into a whole CTs is a challenging task owing to the complicated molecular interactions between fibrils. In addition, to simplify our study of external applied forces, which consist of both tensile and compressive forces, only the tensile stress is examined because GAGs can convert compression stress into tensile stress and hence the total tensile stress is assumed to be the vectorial sum of both tensile and compression forces.

A well constructed and stable collagen pair is assumed to maintain its structure by the attachment of GAGs, subject to at least a small perturbation due to molecular interactions between collagen-collagen, collagens-GAGs, thermal fluctuations, sudden shocks etc. Suppose that we apply a tensile stress on one end of the collagen 1 (see Fig. 4.8), where this perturbation alters the mechanical structure of the collagen pair.

The displacements between v_{i+1} and v_i are denoted by Δ_i for $i = 1, \ldots, N-1$ where N is the total number of oligomers, which are defined by a segment of the collagen pair with two GAGs attached at its ends. Likewise for the collagen 2, the displacements of u_{i+1} and u_i are denoted by δ_i. Schematic diagrams of an unstretched and a stretched collagen pair are shown in Fig. 4.7 and Fig. 4.8 respectively. We postulate the potential energy of collagens utilizing Hookes's law, which reads

$$V = \frac{1}{2}k\delta^2,$$

where k is a spring constant and δ is the extension. Given the potential energy form, it is straightforward to show that the potential energy of a collagen pair, V_c, is given by

$$V_c = \sum_{i=1}^{N} \frac{1}{2}k_c \left(\delta_i - \frac{\ell_c}{N}\right)^2 + \sum_{i=1}^{N} \frac{1}{2}k_c \left(\Delta_i - \frac{\ell_c}{N}\right)^2, \tag{4.34}$$

where N, k_c and ℓ_c are the total number of oligomers that exist in the collagen, the spring constant of the collagen, and the natural length of a collagen respectively. Moreover, δ_i and Δ_i are defined by $\delta_i = u_{i+1} - u_i$ and $\Delta_i = v_{i+1} - v_i$ for $i = 1, 2, \ldots, N-1$ respectively. In addition, we postulate the potential energy of GAGs utilizing the worm-like chain model. We now leave the more sophisticated model of section 4.1 and return here to Eq. (4.1) restated here for convenience as

$$f = \frac{k_B T}{A}\left\{\frac{z}{L} + \frac{1}{4}\left(1 - \frac{z}{L}\right)^{-2} - \frac{1}{4}\right\}, \tag{4.35}$$

where f, k_B, T, A, z, L denote the applied force, Boltzmann's constant, the absolute temperature, the persistence length, extension and the total contour length of the GAG respectively. Then, the potential energy of all GAGs, V_g, can then be obtained

by integrating Eq. (4.35) with respect to z and summing up the total number of GAGs, N, to yield

$$\begin{aligned} V_g &= \sum_{i=1}^{N} \left\{ \frac{1}{2} k_g \left\{ \sqrt{(v_i - u_i)^2 + (\ell_g)^2} - \ell_g \right\}^2 \right. \\ &+ \frac{L^2}{4} k_g \left\{ 1 - \frac{\sqrt{(v_i - u_i)^2 + (\ell_g)^2} - \ell_g}{L} \right\}^{-1} \\ &- \left. \frac{L}{4} k_g \left\{ \sqrt{(v_i - u_i)^2 + (\ell_g)^2} - \ell_g \right\} \right\}, \end{aligned} \tag{4.36}$$

where k_g and ℓ_g denote $(k_B T)/(AL)$ and the natural length of GAGs respectively. We can then relate u_i and v_i to δ_i, Δ_i and s, which is the off-set between fibrils (See Fig. 4.8). Notice that s is a function of f as the collagen pair starts to slide away with respect to each other, subject to the external force. Hence, u_i and v_i are geometrically related by

$$\begin{aligned} &v_1 = u_1 + s, \\ &v_2 = u_2 + s + (\Delta_1 - \ell_c/N) - (\delta_1 - \ell_c/N) = u_2 + s + (\Delta_1 - \delta_1), \\ &\quad \vdots \\ &v_i = u_i + s + \sum_{k=1}^{i} (\Delta_k - \delta_k), \\ &\quad \vdots \\ &v_N = u_N + s + \sum_{k=1}^{N} (\Delta_k - \delta_k). \end{aligned} \tag{4.37}$$

After we relate the kinematics between the collagen pair, we can simplify Eq. (4.36) in terms of the displacements δ_i and Δ_i, giving

$$
\begin{aligned}
V_g &= \sum_{i=1}^{N} \left\{ \frac{1}{2} k_g \left\{ \sqrt{\left[s + \sum_{k=1}^{i} (\Delta_k - \delta_k) \right]^2 + (\ell_g)^2} - \ell_g \right\}^2 \right. \\
&+ \frac{L^2}{4} k_g \left\{ 1 - \frac{\sqrt{\left[s + \sum_{k=1}^{i} (\Delta_k - \delta_k) \right]^2 + (\ell_g)^2} - \ell_g}{L} \right\}^{-1} \\
&- \left. \frac{L}{4} k_g \left\{ \sqrt{\left[s + \sum_{k=1}^{i} (\Delta_k - \delta_k) \right]^2 + (\ell_g)^2} - \ell_g \right\} \right\}. \qquad (4.38)
\end{aligned}
$$

Since the elongation of collagen 1 causes the elongation of collagen 2, we can relate δ_i and Δ_i by the relative displacements ϵ_i. That is

$$
\Delta_i = \delta_i + \epsilon_i. \qquad (4.39)
$$

Assuming statistical equilibrium, we let $\delta_i = \delta$, $\Delta_i = \Delta$ and $\epsilon_i = \epsilon$ for all i. Hence, Eqs. 4.34 and 4.38 reduce to

$$
\begin{aligned}
V_c &= \frac{1}{2} k_c N \left\{ \left(\delta - \frac{\ell_c}{N} \right)^2 + \left(\delta + \epsilon - \frac{\ell_c}{N} \right)^2 \right\}, \\
V_g &= \sum_{i=1}^{N} \left\{ \frac{1}{2} k_g \left\{ \sqrt{(s + i\epsilon)^2 + (\ell_g)^2} - \ell_g \right\}^2 \right. \\
&+ \frac{L^2}{4} k_g \left\{ 1 - \frac{\sqrt{(s + i\epsilon)^2 + (\ell_g)^2} - \ell_g}{L} \right\}^{-1} \\
&- \left. \frac{L}{4} k_g \left\{ \sqrt{(s + i\epsilon)^2 + (\ell_g)^2} - \ell_g \right\} \right\}. \qquad (4.40)
\end{aligned}
$$

Since each GAG has its own maximum length K and the displacement between u_N and v_N corresponds the maximum length of GAG given in the collagen pair, which must be smaller or equal to K. Given that, we have

$$|v_N - u_N| = \sqrt{(s + N\epsilon)^2 + (\ell_g)^2} \leq K, \tag{4.41}$$

from which, we show that the maximum number of oligomers N_{max} allowed in a given collagen satisfies the following inequality

$$N_{max} \leq \frac{\sqrt{(K)^2 - (\ell_g)^2} - s}{\epsilon} = \lfloor \frac{\sqrt{(K)^2 - (\ell_g)^2} - s}{\epsilon} \rfloor, \tag{4.42}$$

where $\lfloor \quad \rfloor$ denotes minimum integer value of the enclosed real number, e.g. $\lfloor 4.3 \rfloor = 4$ respectively. Note that Eq. (4.42) ignores the maximum strain that can be held by a collagen, and while ϵ is a rather abstract quantity, it can be expressed in terms of s by minimizing the maximum potential energy E_{max} of the collagen pair with respect to ϵ at equilibrium (see Appendix 6.10 for details). At first glance, s is insignificant under small natural external forces, i.e. thermal fluctuations and internal molecular interactions. However, s becomes crucial when we consider the collagen pair under large external tractions. One interesting thing about the above equation is that it limits the possible number of oligomers that can exist for a given stable collagen and it is model independent because it arises solely from a geometric point of view. Also, the inequality reveals the importance of GAGs in relation to the growth of the collagen pair. Hence, the longer the maximum length of GAGs, the longer the structural collagen pair can be. Although the inequality does not prove the possibility of the existence of ring conformational transitions of GAGs, it does provide evidence that the existence of conformational transitions increases K and hence encourages the growth of the collagen pair. Further, the higher the effectiveness of the force transmission of GAGs between fibril and fibril, the lower the value of ϵ, and hence longer the collagen can be.

The induced force, F', in collagen 2, generated by collagen 1 and the relative displacement, ϵ, of the system, can be determined to be

$$F' = F - k_c\epsilon, \qquad \epsilon = \frac{1}{N}(L_1 - L_2), \tag{4.43}$$

where L_1 and L_2 are the total molecular contour length of the collagen 1 and 2 respectively. F' and ϵ can hence be determined experimentally by knowing k_c, F, N, L_1 and L_2. In particular, ϵ can be measured to find N_{max}. Given N_{max}, we can obtain the maximum molecular energy for a collagen pair, E_{max}, namely

$$\begin{aligned} E_{max} &= \frac{1}{2}k_c N_{max}\left\{ \left(\delta - \frac{\ell_c}{N_{max}}\right)^2 + \left(\delta + \epsilon - \frac{\ell_c}{N_{max}}\right)^2 \right\} \\ &+ \sum_{i=1}^{N_{max}} \left\{ \frac{1}{2}k_g \left\{ \sqrt{(s+i\epsilon)^2 + (\ell_g)^2} - \ell_g \right\}^2 \right. \\ &+ \frac{L^2}{4}k_g \left\{ 1 - \frac{\sqrt{(s+i\epsilon)^2 + (\ell_g)^2} - \ell_g}{L} \right\}^{-1} \\ &- \left. \frac{L}{4}k_g \left\{ \sqrt{(s+i\epsilon)^2 + (\ell_g)^2} - \ell_g \right\} \right\}. \end{aligned} \tag{4.44}$$

The maximum molecular energy E_{max} grows quadratically with the extension δ and is related linearly to N_{max}, which is given by Eq. (4.42) and determined by K and ϵ. Hence, the existence of flexible GAGs with long maximum length K increases the number of oligomers N_{max}, which in return tightens the system dramatically. In addition, assuming a large N_{max} and a small ϵ, the modulus of a collagen pair, k_t, can be determined easily by the second derivative of E_{max} with respect to δ. Upon performing two differentiations, we approximate the modulus of the collagen pair, k_t, as

$$k_t \approx k_c N_{max}. \tag{4.45}$$

Again, k_t depends linearly on N_{max}, where the rest of arguments are very similar to

the discussion for the maximum molecular energy above.

4.2.2 Numerical results and analysis

In this sub-section, we carry out a numerical analysis on the results derived in the previous sub-section, and finally we examine the breaking point of a collagen pair. Firstly, given Eq. (4.44), we assume the value of the parameters given in [121], namely $k_c = 0.2$ GPa, $k_g = 0.02$ GPa, $\ell_c = 100$ μm, $\ell_g = 0.02$ nm, $L = 0.2$ nm and 3 maximum numbers of oligomer are examined, namely $N_{max1} = 1$ K, $N_{max2} = 10$ K and $N_{max3} = 0.1$ M. Further, without loss of generality, the offset s is assumed to be zero, which corresponds to the tight molecular interaction between fibrils or the collagen pair under a small traction. The potential energy of GAGs is neglected due to its insignificance in comparison to the potential energy of the collagen pair that is demonstrated in Fig. 4.9, where ϵ has been linearized with the extension δ. The numerical result shows that the potential energy of GAGs utilizing the above parameters is 6 orders of magnitude smaller than the potential energies of the paired collagen for all three cases we considered. Given that, the potential energies of the collagen pair versus the extension δ, ranging from 0 to 100 nm for N_{max1}, N_{max2} and N_{max3}, are plotted together in Fig. 4.10.

Note that the maximum molecular energy increases quadratically when the extension increases linearly. In addition, δ is determined by the applied force F and the relative displacement ε. For example, for a constant Δ, δ achieves its maximum value when $\varepsilon = 0$. Further, E_{max} increases linearly with N_{max}, which in return depends positively on K but negatively on ε. The toughness of a collagen pair, k_t, is defined in the previous sub-section as the second derivative of E_{max} with respect to δ, and hence the higher the slope of E_{max} with respect to the extension δ, the stiffer the collagen pair is. In conclusion, given a collagen pair, it is tougher whenever GAGs have a higher value of K and a higher ability in transmitting forces between fibrils. However, the existence of GAGs contributes almost nothing to the toughness of the collagen pair but is significant to maintain the stable structure and boost up

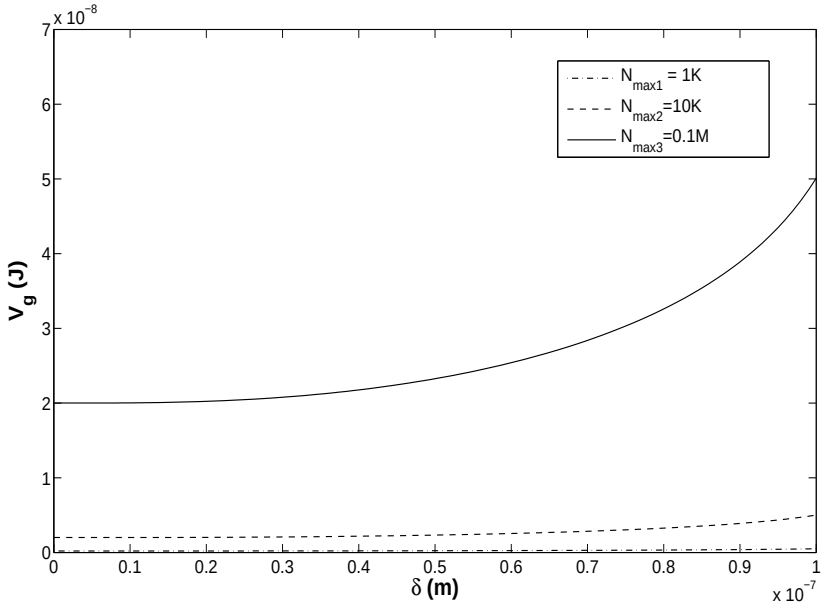

Figure 4.9: Potential energy of GAG, V_g, versus extension, δ ranging from 0 to 100 nm, for $N_{max1} = 1$ K, $N_{max2} = 10$ K and $N_{max3} = 0.1$ M respectively.

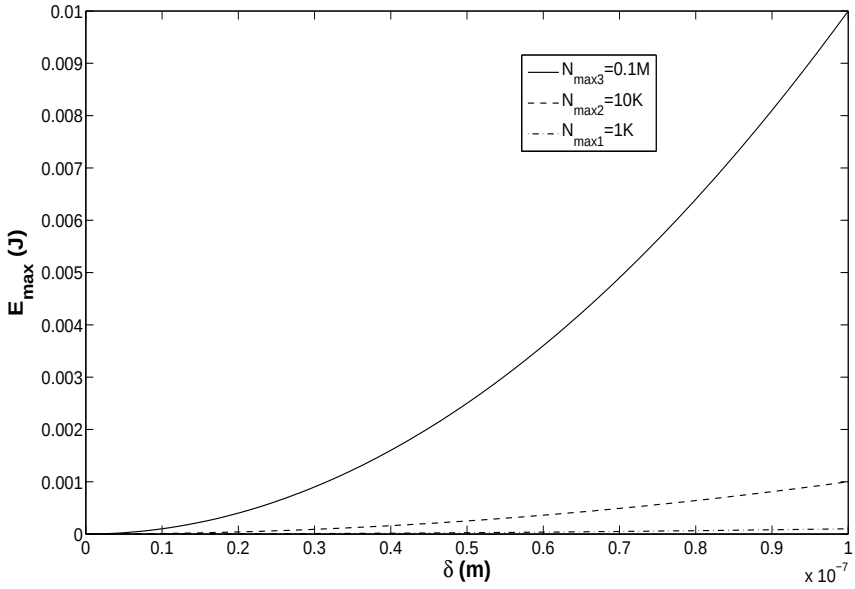

Figure 4.10: Potential energy of the collagen pair, E_{max}, versus extension, δ ranging from 0 to 100 nm, for $N_{max1} = 1$ K, $N_{max2} = 10$ K and $N_{max3} = 0.1$ M respectively.

the toughness of the collagen pair, which are consistent to the results that an increased PYD or DPD ratio (the most abundant mature GAGs in bone collagen) is related to the increased compressive strength in bone (CTs) [89, 5, 114, 115, 6] but has no huge effect on toughness or ductility of bone [180, 163, 74, 59].

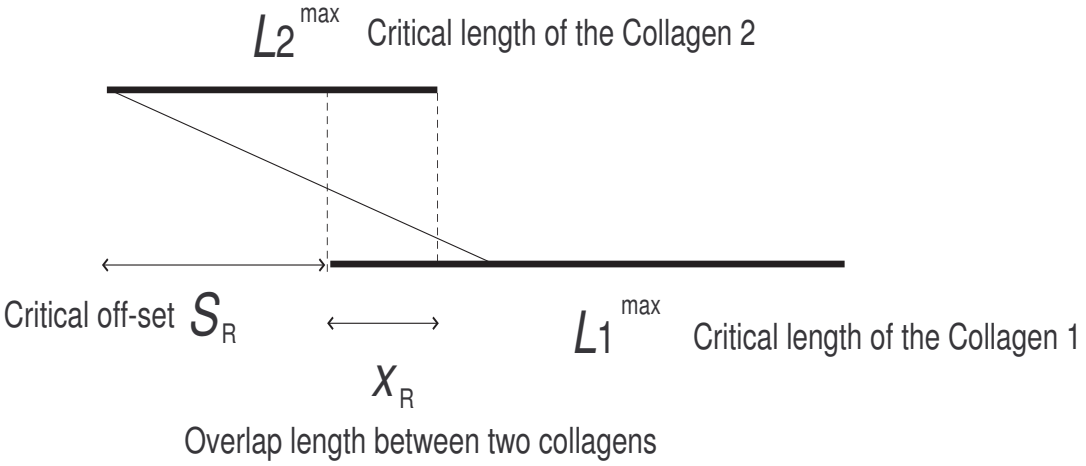

Figure 4.11: The breaking fraction of the collagen pair.

We end this sub-section by extending concepts that we developed above to determine the point at which a collagen pair will break. For the study of a collagen pair, an important parameter is the fraction of the collagen pair, χ_R, in which the breaking point occurs (see Fig. 4.11). The breaking point is assumed to occur when the bridge between u_1 and v_1 is finally broken (see Figs. 4.7 and 4.8). From Fig. 4.11, we write

$$L_1^{max} + L_2^{max} - \chi_R = s_R + L_1^{max}, \tag{4.46}$$

where L_1^{max} and L_2^{max} are the critical lengths of collagens 1 and 2 respectively and s_R is the critical off-set of the system. After some re-arrangement, we find that

$$\chi_R = L_2^{max} - s_R. \tag{4.47}$$

In addition, we know that when the collagen pair is about to be torn apart, $N_{max} = 0$, from Eq. (4.42), we deduce

$$s_R = \sqrt{(K)^2 - (\ell_g)^2}. \tag{4.48}$$

Therefore, upon comparing Eqs. 4.47 and 4.48, we have

$$\chi_R = L_2^{max} - \sqrt{(K)^2 - (\ell_g)^2}. \tag{4.49}$$

Notice that the above equation links the macro-quantity χ_R to micro-quantities such as L_2^{max}, K and ℓ_g. Once again, the larger the possible length of GAGs, the smaller the breaking fraction of the collagen pair, which implies that we need to put more forces in the system to tear the collagen pair apart, which is consistent to the theoretical result obtained by [19].

4.2.3 Conclusion

In this section, we utilize simple applied mathematical modeling techniques to describe the mechanics of a stretched collagen pair. We find that the maximum number of oligomers that can exist in a given collagen depends on the maximum length of GAGs and the effectiveness of the GAGs in transferring forces between fibrils. That is, a collagen can grow longer for the longer GAGs and the higher effectiveness of GAGs in transferring forces between fibrils. This concept can then be extended naturally to the toughness and the breaking point of a collagen pair, which are found to be intimately related to the microscopic characteristics of GAGs. In addition, the possible conformational transitions of GAGs strengthen the whole structure of CTs and as such CTs maintain our body shape from any large external traction. Last but not least, we refer the reader who is interested in utilizing computing simulations and continuum mechanics to model the macroscopic structure of CTs, to those references listed in the introduction of this section.

4.3 List of Symbols

Section 4.1

(θ, ϕ) is the polar angles 115

A is the bending stiffness 114

F is the functional 116

L is the total molecular contour length 114

T is the absolute temperature 114

W is the effective energy 114

f is the applied external force 114

f_c^{min} is the minimum cut-off force of the molecule 121

f_c is the cut-off force of the molecule 120

f_s is the critical force of the molecule 125

k_B is the Boltzmann's constant 114

z is the extension of the molecule 114

Φ is the modulus of elasticity 120

κ are the principal curvature of the molecule 115

μ $\mu = f/(Ak_BT)$ 116

Section 4.2

A is the persistence length of the GAG 133

E_{max} is the maximum molecular energy of a collagen pair 137

K is the maximum length of the GAG 135

L is the total contour length of the GAG 133

L_1^{max} is the critical length of the collagen 1 140

L_2^{max} is the critical length of the collagen 2 140

L_1 is the total molecular contour length of the collagen 1 137

L_2 is the total molecular contour length of the collagen 2 137

Chapter 5

Conclusion

In this thesis, physical principles, classical continuum mechanics and applied mathematical modeling have been employed to the fields of nano and biotechnology. The topics fall into three broad areas, namely the mechanics of three distinct nano structures, the axial buckling of nanotubes and nanopeapods and the worm-like chain model for stretched semi-flexible molecules and its applications to molecular stretching in the extracellular matrix. For each section wherever possible, we compare the applied mathematical models with experimental or molecular dynamics simulation results, and we find that the major merit of the applied mathematical modeling lie in the fast computational times and the ability to produce illustrative insightful arguments. The broad overview of each chapter is now summarized.

In Chapter 2, we investigate the dynamics of a carbon atom or a C_{60} fullerene inside a carbon nanotube. We assume that the carbon atoms are uniformly distributed over the surface of the carbon nanotube so that the molecular potential energy can be approximated by the continuous approach. We determine the oscillatory motion of a carbon atom inside various nanotubes. In particular, the spiral-like motion is found when the atom is oscillating inside sufficiently large nanotubes. A similar phenomena is also predicted for a C_{60} fullerene oscillating inside a nanotube. However, we find that the spiral-like motion of C_{60}-nanotube oscillators is induced but it is unstable, which allows us to determine the resultant oscillatory frequency of such oscillators. Next, we investigate a nano tippe top spinning either on a graphene

sheet or inside a carbon nanotube in the presence of an applied magnetic field. We find that while the retarding magnetic force makes the nano top precess, it does not flip over like the classical tippe top, due to the fact that gravity is insignificant at the nanoscale but rather lies to one side. In addition, while the nano top is in the lying down position, if we apply the magnetic force which is of the same magnitude but in the opposite direction to the previously applied retarding magnetic force, then the nano top will return to its original standing up position. Hence, the "standing up" and "lying down" configurations of the nano top might be considered for a future memory device. We next examine three two-body nanoscale problems, namely an atom–carbon nanotube system, a fullerene–carbon nanotube system and a fullerene–fullerene system. The circular orbiting radii of all the proposed nano systems are estimated by seeking the minimum energy configuration of their effective potential energies. Since the loci for these nano systems cannot be determined in terms of well-known analytical functions, a numerical method has been employed to obtain the various loci of the orbiting paths. In addition, a perturbation method has been utilized in order to gain some insight into possible analytical formulations of the loci. Finally, the circular orbiting frequencies of all three proposed nano systems are shown to reach the gigahertz range.

In Chapter 3, we have determined a new solution for the nano-electromechanical system of a buckled nanotube by incorporating the full expression for curvature into the elastic energy of the buckled nanotube. We find that while the approximate solution underestimates the maximum displacement of the buckled nanotube in the weak bending regime, our numerical solution predicts an entirely different bending behavior in comparison to the approximate solution in the strong bending regime. Next, we investigate the buckling of the (10,10), (10,10)@(16,16), the C_{60}@(10,10), and the C_{60}@ (10,10)@(16,16) nanostructures by incorporating the van der Waals molecular potential energies between the various components of the carbon nanotubes. We find that the critical forces reduce as a result of the molecular interactions between layers of carbon nanotubes and the interactions between fullerenes. The Euler-Bernoulli

beam equation is also utilized to obtain the buckling displacement of the (10,10) nanotube and C_{60}@(10,10) nanopeapod. The influence of the molecular interactions between fullerenes and nanotubes decreases in the strong force regime. This suggests that the enclosure of fullerenes inside nanotubes might be the sole means of the buckling, which may lead to the development of potential nano devices, such as biological sensing, measuring devices for small forces, electric charges or Casimir forces.

In Chapter 4, we derive a new analytical force-extension formula for the worm-like chain model, which is determined by minimizing the effective energy of a stretched molecule by incorporating all possible orientations of the monomers under thermal equilibrium. We have utilized our new formula to predict additional physical parameters such as the expressions for the free energy and the cut-off force for the stretched molecule. In addition, the new force-extension formula predicts the phase changes of the stretched molecule and anticipates that all molecules must undergo one phase change when they are stretched into their total contour lengths and two phase changes when they are stretched beyond their total contour lengths. The new force-extension formula is then utilized to fit some recent experimental data. However, in the future we may be able to incorporate the Boltzmann energy distribution into the model to account for the effect of entropy. Next, we utilize simple applied mathematical modeling techniques to describe the structure of a collagen pair in the extracellular matrix. We find that the maximum number of oligomers that can exist in a given collagen pair depends on the maximum length of the GAGs and the effectiveness of the GAGs in transferring forces between fibrils. That is, collagen can grow longer when the GAGs increase in length and increase their effectiveness in transferring forces between fibrils. This concept can be extended to consider the toughness and the breaking point of a collagen pair, which are also found to be intimately related to the microscopic characteristics of the GAGs.

Chapter 6

Appendix

6.1 Equations of motion

We briefly state explicit forms of equations of motion obtained from Eq. (2.29). From Eq. $(2.29)_1$, the three rotational equations are given by

$$\begin{aligned} A\ddot{\theta} &= -\Omega(C\omega - A\Omega\cos\theta)\sin\theta - aN\sin\theta - h(\theta)F_x, \\ A\sin\theta\dot{\Omega} &= (C\omega - 2A\Omega\cos\theta)\dot{\theta} + (a - R\cos\theta)F_y, \\ C\dot{\omega} &= R\sin\theta F_y, \end{aligned} \tag{6.1}$$

where $h(\theta) = R - a\cos\theta$. From Eq. $(2.29)_2$ the three translational equations are of the form

$$\begin{aligned} m\dot{u}_x &= m\Omega u_y + F_x, \\ m\dot{u}_y &= -m\Omega u_x + F_y, \\ m\dot{u}_z &= N - mg, \end{aligned} \tag{6.2}$$

where

$$\begin{aligned} F_x &= \frac{-\mu N\left\{u_x - h(\theta)\dot{\theta}\right\}}{\sqrt{\left\{u_x - h(\theta)\dot{\theta}\right\}^2 + \left\{u_y + [R(\omega - \Omega\cos\theta) + a\Omega]\sin\theta\right\}^2}} \\ &\quad -H_x, \\ F_y &= \frac{-\mu N\left\{u_y + [R(\omega - \Omega\cos\theta) + a\Omega]\sin\theta\right\}}{\sqrt{\left\{u_x - h(\theta)\dot{\theta}\right\}^2 + \left\{u_y + [R(\omega - \Omega\cos\theta) + a\Omega]\sin\theta\right\}^2}} \\ &\quad -H_y, \end{aligned} \tag{6.3}$$

and H_x and H_y denote the strength of the retarding magnetic force in the x- and y-directions respectively. By multiplying $\sin\theta$ both sides of Eq. $(6.1)_2$ we obtain

$$A\sin^2\theta\dot{\Omega} = (C\omega - 2A\Omega\cos\theta)\sin\theta\dot{\theta} + (a - R\cos\theta)F_y\sin\theta. \tag{6.4}$$

From Eq. $(6.1)_3$ we have $F_y\sin\theta = C\dot{\omega}/R$, which upon substituting into Eq. (6.4) we have

$$A\sin^2\theta\dot{\Omega} + 2A\Omega\cos\theta\sin\theta\dot{\theta} = C\omega\sin\theta\dot{\theta} - C\dot{\omega}\cos\theta + aC\dot{\omega}/R,$$

which can be written as

$$A\frac{d(\Omega\sin^2\theta)}{dt} = \frac{aC}{R}\frac{d\omega}{dt} - C\frac{d(\omega\cos\theta)}{dt}. \tag{6.5}$$

Thus, from Eq. (6.5) we obtain

$$A\Omega\sin^2\theta = aC\omega/R - C\omega\cos\theta + J^*, \tag{6.6}$$

where J^* is a constant of integration. By multiplying R both sides of Eq. (6.6) we have

$$J = A\Omega R\sin^2\theta + C\omega(R\cos\theta - a), \tag{6.7}$$

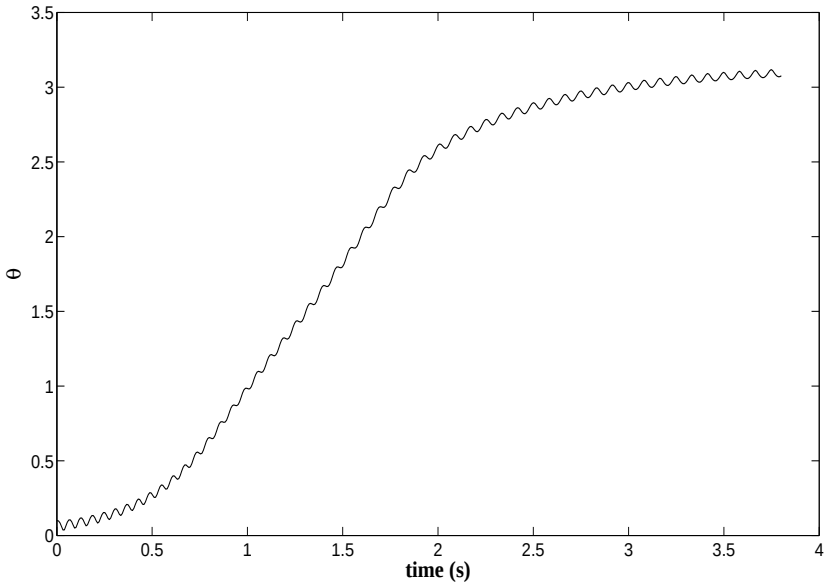

Figure 6.1: Nutation angle θ for classical macro scale tippe top.

where the constant J is referred to as the Jellett's constant [157] and our numerical result indicates that this constant is zero throughout the precession process. Since J is an invariant constant, if we let $J = 0$ and $a \ll R$, for a large t and $\Omega = 0$, we obtain the asymptotic nutation angle as $\theta = \pi/2$.

As a benchmark, we utilize our numerical scheme to show the behaviour of the classical macro scale tippe top with zero magnetic force. Here, the values of parameters are taken to be $R = 0.015$ m, $a = 0.1R$ m, $M = 0.015$ kg, $A = C = (2/5)MR^2$ and $\mu = 0.1$, with initial conditions: $\theta = 0.1$, $\omega = 100$, $\Omega = 0$ and $\dot{\boldsymbol{X}} = (0, 0, 0)$. Thus, from Eqs. (6.2) and (6.3) we obtain numerical results for nutation angle $\theta(t)$ as illustrated graphically in Fig. 6.1. From this figure, we can see that θ approaches π implying that the top flips over, which is consistent with Ueda et al. [157].

6.2 Stability analysis

We utilize a simple stability argument to investigate the stability of the nano top for $\theta = 0$, $\pi/2$ and π. Without the external magnetic retarding force, i.e. $H_x = H_y = 0$, we consider a small perturbation around the standing up axis, namely $\theta = \epsilon$ for

small $\epsilon > 0$. Eq. $(6.1)_1$ becomes

$$\ddot{\epsilon} = -aN\epsilon/A, \tag{6.8}$$

which implies that the spinning nano top is always stable. If we incorporate the external magnetic retarding force, i.e. $H_x = H_y = H$, which is a constant. For $\theta = \epsilon$, Eq. $(6.1)_1$ becomes

$$\ddot{\epsilon} = -aN\epsilon/A + (R-a)H/A, \tag{6.9}$$

which also implies that the nano top is stable. We note that for the case $\theta = \epsilon$, we assume $\Omega = 0$.

Next, we check the stability of the nano top at $\theta = \pi$. Upon substituting $\theta = \pi - \epsilon$, Eq. $(6.1)_1$ becomes

$$\ddot{\epsilon} = \frac{(C+A)\Omega^2 + aN}{A}\epsilon - \frac{(R+a)H}{A}, \tag{6.10}$$

noting that $\omega = \Omega$ when θ tends to π. Eq. (6.10) implies that the nano top is always unstable, and therefore it does not flip over.

For the lying down position, i.e. $\theta = \pi/2 - \epsilon$, Eq. $(6.1)_1$ becomes

$$\ddot{\epsilon} = -\frac{A\Omega^2 - aH}{A}\epsilon - \frac{HR - C\omega\Omega - aN}{A}, \tag{6.11}$$

which is stable if $A\Omega^2 - aH > 0$ or $\Omega^2 > aH/A$.

6.3 Asymptotic expansion for $\theta = \pi/2$

We check the compatibility between our numerical results and the asymptotic expansions for the governing ordinary differential equations given in Eq. (2.29) or Eq. (6.1) when the nano top is lying down and the time t is sufficiently large. Upon

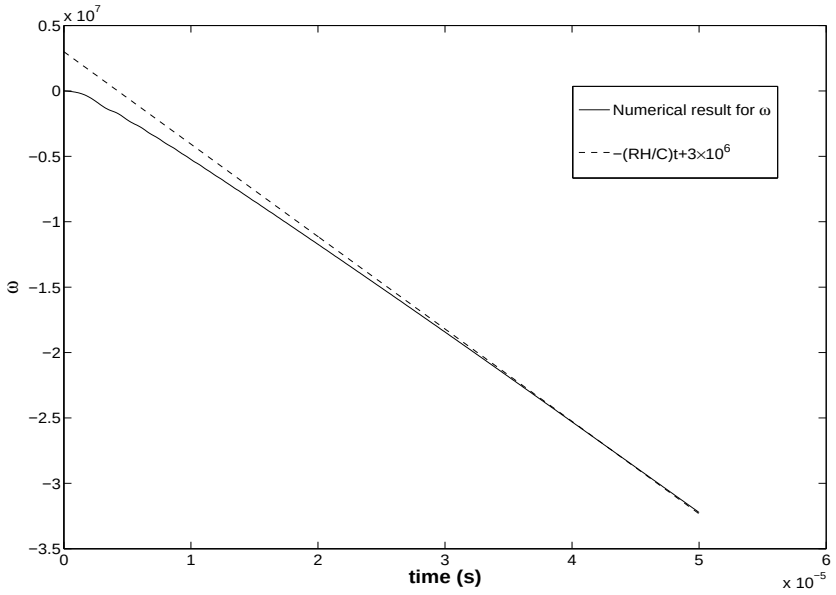

Figure 6.2: Asymptotic expansion for ω.

substituting $\theta = \pi/2$ into Eqs. $(6.1)_1$, $(6.1)_3$, $(6.2)_1$ and $(6.2)_2$, we obtain

$$\Omega = RH/(C\omega), \quad \dot{\omega} = -RH/C,$$
$$m\dot{u}_x = m\Omega u_y - H, \quad m\dot{u}_y = -m\Omega u_x - H, \tag{6.12}$$

respectively. Noting here that we assume $H_x = H_y = H$. From Eq. $(6.12)_2$, upon integrating both sides by t, we have

$$\omega = -RHt/C + c_1. \tag{6.13}$$

This asymptotic expansion and its corresponding numerical result for ω are plotted together in Fig. 6.2. We note that the constants utilized here are given by $R = 3.55$ Å, $C = 0.5A$, $A = (2/3)mR^2$, $m = 1.196 \times 10^{-24}$ kg and $H = 0.1$ zN. We fit Eq. (6.13) with the numerical solution for ω and obtain $c_1 = 3 \times 10^6$. Upon knowing ω, we can determine Ω by utilizing Eq. $(6.12)_1$ as

$$\Omega = \frac{RH}{c_1 C - RHt}, \tag{6.14}$$

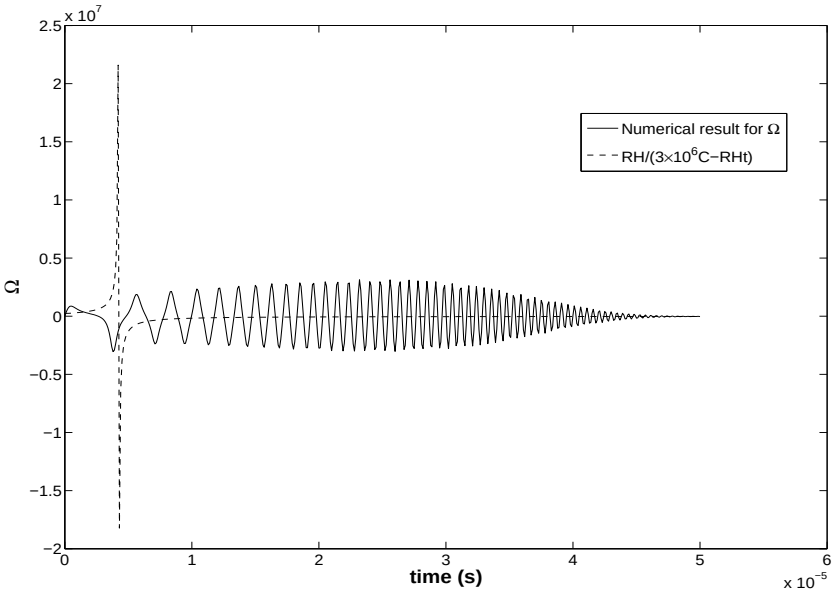

Figure 6.3: Asymptotic expansion for Ω.

where this asymptotic equation decays to zero for a sufficiently large t and the corresponding result with its numerical solution are plotted in Fig. 6.3. Given the asymptotic expansions for Ω, we can determine the asymptotic expansions for both u_x and u_y, which are given by

$$\begin{aligned} m\dot{u_x} &= \frac{mRH}{(c_1C - RHt)}u_y - H, \\ m\dot{u_y} &= -\frac{mRH}{(c_1C - RHt)}u_x - H. \end{aligned} \tag{6.15}$$

We can solve Eq. (6.15) analytically by introducing $v = u_x + iu_y$, where $i = \sqrt{-1}$. By multiplying i both sides of Eq. $(6.15)_2$ and combining with Eq. $(6.15)_1$ we have

$$\dot{v} + \frac{RHi}{(c_1C - RHt)}v = -\frac{H}{m}(1+i). \tag{6.16}$$

By multiplying both sides of Eq. (6.16) by an integrating factor $\exp\left(-i\log\left(c_1C - RHt\right)\right) = 1/(c_1C - RHt)^i$ we obtain

$$\frac{d}{dt}\left(\frac{v}{(c_1C - RHt)^i}\right) = -\frac{H}{m}\frac{(1+i)}{(c_1C - RHt)^i},$$

which on integrating we deduce

$$\frac{v}{(c_1C - RHt)^i} = \frac{(1+i)}{(1-i)}\frac{1}{Rm}(c_1C - RHt)^{1-i} + c_2,$$

where c_2 denotes a constant. Thus, the solution of Eq. (6.16) is given in the form

$$v(t) = \frac{(1+i)}{(1-i)}\frac{(c_1C - RHt)}{Rm} + c_2 e^{i\log(c_1C - RHt)}. \tag{6.17}$$

To determine the complex constant c_2 to fit our numerical data, we assign at $t = t^*$, $u_x(t^*) = u_1$ and $u_y(t^*) = u_2$, where u_1 and u_2 are constants. Thus, c_2 is given by

$$c_2 = e^{-i\log\lambda}\left\{u_1 + iu_2 - \frac{i\lambda}{Rm}\right\},$$

where $\lambda = c_1C - RHt^*$. Upon substituting into Eq. (6.17) and simplifying we have

$$v(t) = \frac{i(c_1C - RHt)}{Rm} + e^{i\beta(t)}\left\{u_1 + iu_2 - \frac{i\lambda}{Rm}\right\},$$

where $\beta(t) = \log\left([c_1C - RHt]/\lambda\right)$. Next, we expand the above equation utilizing Euler's formula, $e^{i\beta} = \cos\beta + i\sin\beta$, to obtain

$$\begin{aligned} v(t) &= u_1\cos\beta(t) + \left\{\frac{\lambda}{Rm} - u_2\right\}\sin\beta(t) + \frac{i(c_1C - RHt)}{Rm} \\ &\quad + iu_1\sin\beta(t) - i\left\{\frac{\lambda}{Rm} - u_2\right\}\cos\beta(t). \end{aligned} \tag{6.18}$$

Since $v = u_x + iu_y$, Eq. (6.18) gives rise to analytical solutions for u_x and u_y, namely

$$\begin{aligned} u_x &= u_1\cos\beta(t) + \left\{\frac{\lambda}{Rm} - u_2\right\}\sin\beta(t), \\ u_y &= \frac{(c_1C - RHt)}{Rm} + u_1\sin\beta(t) - \left\{\frac{\lambda}{Rm} - u_2\right\}\cos\beta(t). \end{aligned} \tag{6.19}$$

The solutions (6.19) for u_x and u_y are plotted together with their corresponding numerical results in Figs. 6.4 and 6.5, respectively. We note that the values of

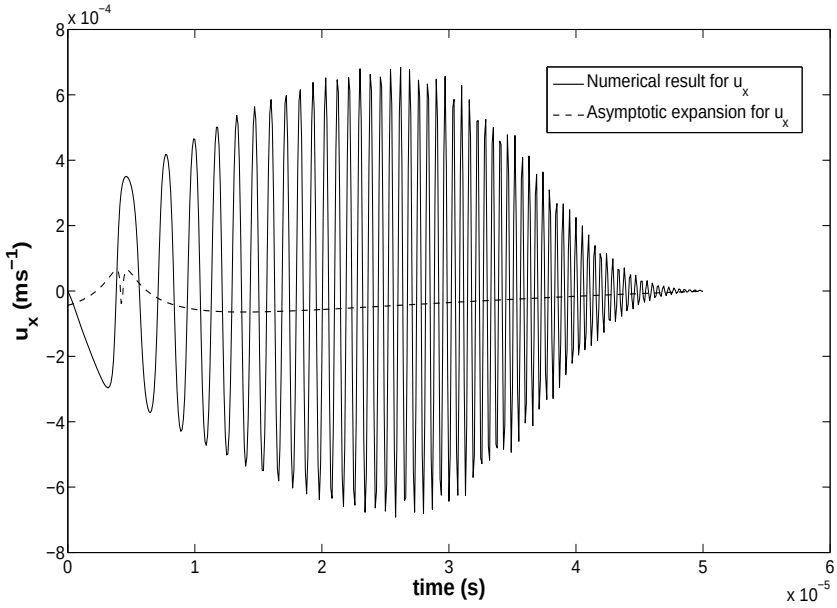

Figure 6.4: Asymptotic expansion for u_x $(6.19)_1$ in comparison with numerical result.

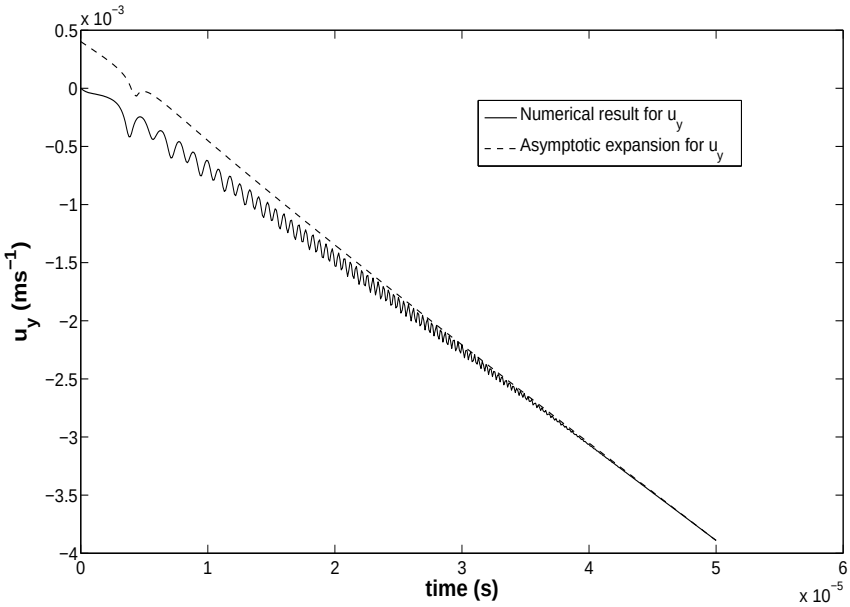

Figure 6.5: Asymptotic expansion for u_y $(6.19)_2$ in comparison with numerical result.

constants utilized here are taken to be $t^* = 5 \times 10^{-5}$ s, $u_1 = -6 \times 10^{-7}$ ms^{-1} and $u_2 = -4 \times 10^{-3}$ ms^{-1}. As can be seen from these figures, the solutions (6.19) agree with the numerical results for sufficiently large t.

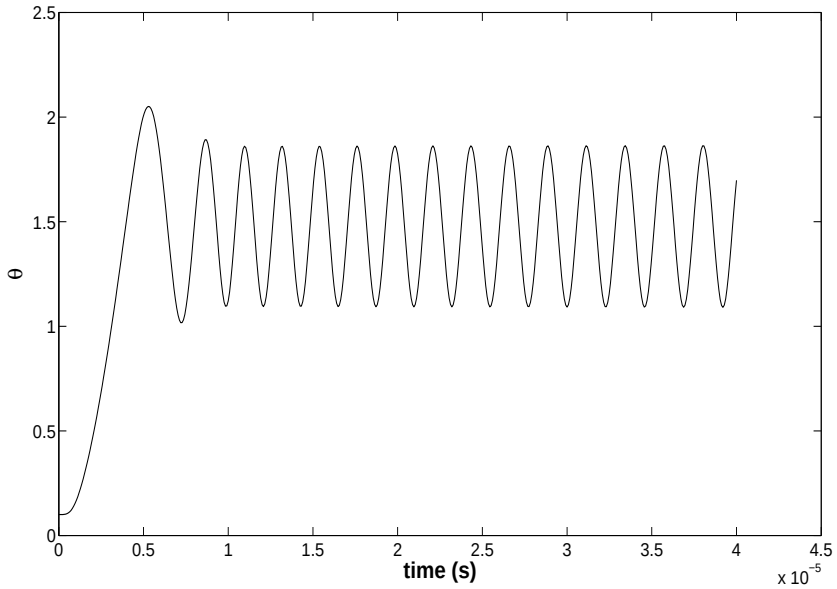

Figure 6.6: Nutation angle θ for nano top when $H_x = 0$ and $H_y = H\mathrm{H}(t_0 - t)$ where $t_0 = 0.8 \times 10^{-5}$ s.

6.4 Retarding magnetic force as step function

We investigate the precession of the nano top subject to a magnetic force which is applied only in the y-direction and only for a finite time t_0. In particular, we consider $H_y = H\mathrm{H}(t_0 - t)$, where H is a constant representing the strength of the magnetic force, $\mathrm{H}(t)$ is the Heaviside unit step function and t_0 denotes the time when the magnetic force is switched off. Two cases are examined, namely $t_0 = 0.8 \times 10^{-5}$ and 10^{-6} seconds. We observe that in the former case the nano top precesses from its initial standing up position to $\theta = 2.1$ soon after the retarding magnetic field is switched off and then it oscillates about $\theta = \pi/2$, as demonstrated in Fig. 6.6.

The effect of the Heaviside function can be seen from the behaviour of ω, which is shown in Fig. 6.7. From this figure, before the switch off time $t_0 = 0.8 \times 10^{-5}$, the magnitude of ω increases but in the opposite direction with respect to the direction of the initial spin due mainly to the retarding magnetic force. After $t = 0.8 \times 10^{-5}$, since the retarding force is switched off, the magnitude of ω starts to decrease by the effect of the frictional force only. For the latter case, we find from Fig. 6.8 that the application of H_y for 10^{-6} s does not provide sufficient angular momentum for the

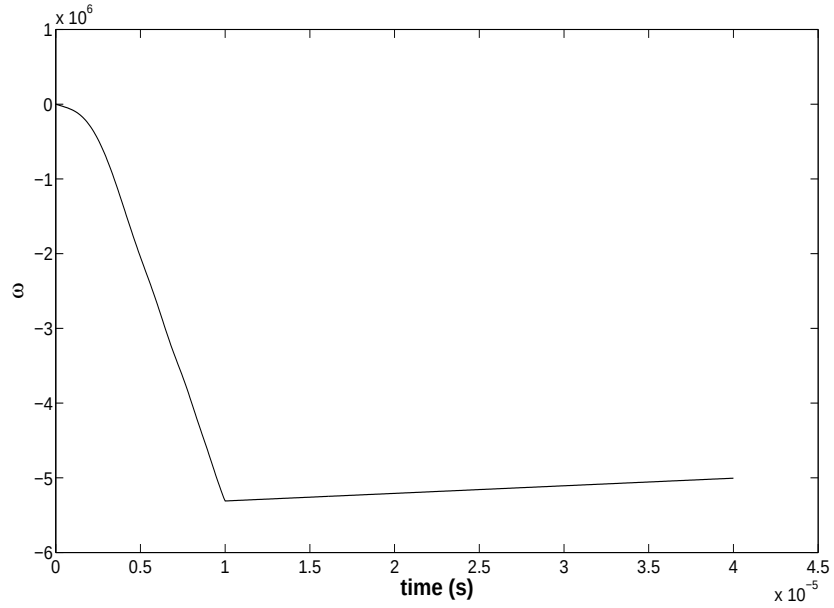

Figure 6.7: Angular frequency ω for nano top when $H_x = 0$ and $H_y = H\mathrm{H}(t_0 - t)$ where $t_0 = 0.8 \times 10^{-5}$ s.

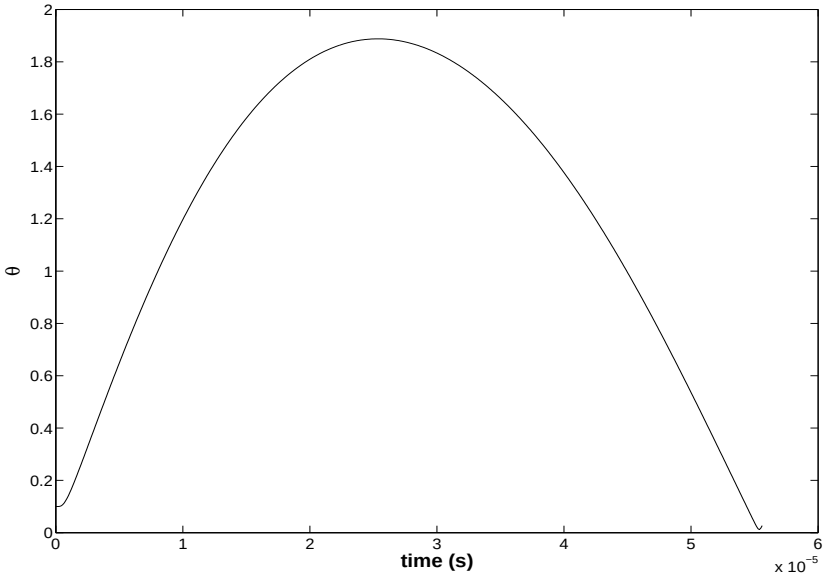

Figure 6.8: Nutation angle θ for nano top when $H_x = 0$ and $H_y = H\mathrm{H}(t_0 - t)$ where $t_0 = 10^{-6}$ s.

nano top to lie down in a stable configuration. The variation of the corresponding ω for this case is presented in Fig. 6.9.

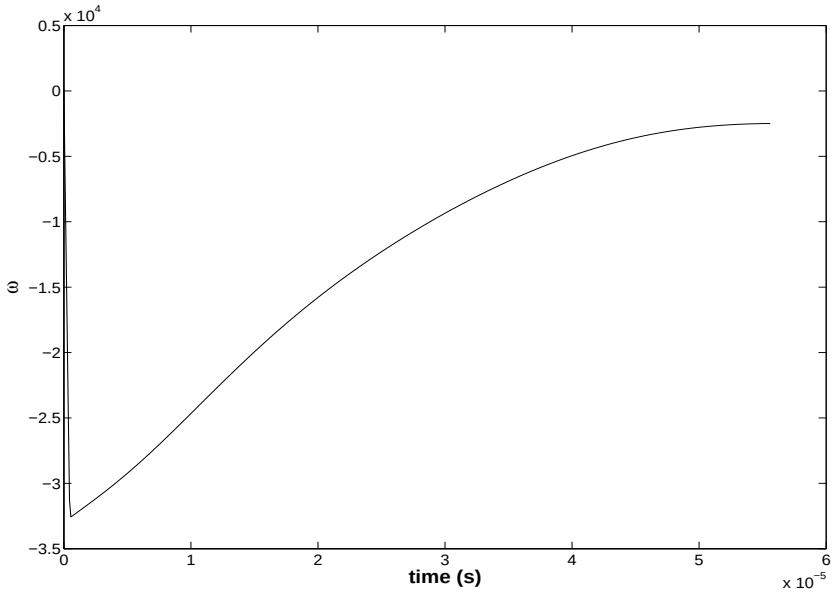

Figure 6.9: Angular frequency ω for nano top when $H_x = 0$ and $H_y = H\mathrm{H}(t_0 - t)$ where $t_0 = 10^{-6}$ s.

6.5 Elastic energy

We derive the internal energy of the buckled beam but with the incorporation of the curvature, which is usually ignored when the buckling is infinitesimal. A useful reference can be like [88]. The strain in a Cartesian coordinate system x_i (i =1,2,3) is defined as usual by

$$e_{ij} = \frac{1}{2}\left(\frac{\partial \eta_i}{\partial x_j} + \frac{\partial \eta_j}{\partial x_i}\right), \tag{6.20}$$

where e_{ij} and η_i denote respectively the second rank strain tensor and the displacement in the i direction. For a linearly elastic material, the stress tensor σ_{ij} is then related to the strain by the stress-strain equation

$$\sigma_{ij} = C_{ijkl} e_{kl}, \tag{6.21}$$

where C_{ijkl} denotes stress-strain tensor. In particular, for an isotropic material, the most general form of C_{ijkl} can be written as

$$C_{ijkl} = \lambda\delta_{ij}\delta_{kl} + \mu(\delta_{ik}\delta_{jl} + \delta_{il}\delta_{jk}), \tag{6.22}$$

where λ and μ denote the Lamé constants. Eq. (6.22) leads Eq. (6.21) to

$$\sigma_{ij} = \lambda\delta_{ij}\delta_{kl} + \mu(\delta_{ik}\delta_{jl} + \delta_{il}\delta jk)e_{kl} = \lambda\delta_{ij}e_{kk} + 2\mu e_{ij}. \tag{6.23}$$

In the usual manner, we can determine the explicit form of the Young's modulus E and the Poisson's ratio σ^* in terms of the two Lamé constants λ and μ as follows

$$E = \frac{\mu(3\lambda + 2\mu)}{\lambda + \mu}, \qquad \sigma^* = \frac{\lambda}{2(\lambda + \mu)}. \tag{6.24}$$

We can now derive the internal energy of the buckled beam. The deformations of the buckled beam are defined as

$$\begin{aligned} \eta_x &= -\sigma^*\kappa xy, \\ \eta_y &= \kappa[\sigma^*(x^2 - y^2) - z^2]/2, \\ \eta_z &= \kappa yz, \end{aligned} \tag{6.25}$$

where κ denotes the curvature of the buckled beam, and from which we may deduce the principal strains

$$\begin{aligned} e_{xx} &= -\sigma^*\kappa y, \\ e_{yy} &= -\sigma^*\kappa y, \\ e_{zz} &= \kappa y, \end{aligned} \tag{6.26}$$

and the principal stresses become

$$\begin{aligned}\sigma_{xx} &= \sigma_{yy} = 0,\\ \sigma_{zz} &= \lambda e_{xx} + \lambda e_{yy} + \lambda e_{zz} + 2\mu e_{zz},\\ &= \kappa\left(-2\sigma^*\lambda + 2\mu + \lambda\right) y = \kappa E y. \end{aligned} \tag{6.27}$$

We note that from our choice of σ^*, σ_{xx} and σ_{yy} vanish automatically and therefore the internal energy of the buckled beam is given by

$$\begin{aligned} W_{int} &= \int_{beam}\left\{\frac{1}{2}e_{ij}C_{ijkl}e_{kl}\right\}d^3x = \int_{beam}\left\{\frac{1}{2}e_{zz}\sigma_{zz}\right\}d^3x,\\ &= \frac{E\kappa^2}{2}\int\left\{\int\int y^2 dxdy\right\}dz = \int\frac{1}{2}EI_z\kappa^2 dz, \end{aligned} \tag{6.28}$$

where I_z denotes the moment of inertia about the z-axis. Further, if we denote $I_z = I$ and adopt $\kappa = y''/(1+y'^2)^{3/2}$, upon making the substitution, $dz^2 = dx^2 + dy^2$, where z is the arc length of the beam, Eq. (6.28) becomes

$$W_{int} = \frac{1}{2}EI\int\frac{y''^2}{(1+y'^2)^{5/2}}dx. \tag{6.29}$$

In addition to the internal energy, the buckled nanotube is also effected by an external energy W_{ext}, which is caused by the gate voltage. In particular, the infinitesimal external energy is given by

$$dW_{ext} = T_{tot}[dz - dx] = T_{tot}[\sqrt{dx^2+dy^2} - dx] = T_{tot}[\sqrt{1+y'^2} - 1]dx, \tag{6.30}$$

where T_{tot} denotes the total force acting on the beam. Since the energy W_{el} is the sum of both the internal elastic energy and the external energy, we have

$$W_{el} = W_{int} + W_{ext} = \int_0^L\left\{\frac{1}{2}EI\frac{y''^2}{(1+y'^2)^{5/2}} + T_{tot}[\sqrt{1+y'^2} - 1]\right\}dx. \tag{6.31}$$

6.6 Capacitance of the system

We determine the capacitance per unit length, $c(y)$, of the nano-electromechanical system. The procedure for finding $c(y)$ is shown as follows: (I) Find the electric field from first principles or the Gauss's Law by exploiting the symmetry of the column, (II) determine the electrostatic potential of the nano-electromechanical system utilizing the method of images determined from the electric field just obtained, (III) determine the capacitance of the system from a knowledge of the electrostatic potential of the system. The electrostatic field $\boldsymbol{E_0}$ between an infinite cylinder and a point, at a distance r away from the cylinder, is given by

$$\boldsymbol{E_0} = \frac{\rho_l}{2\pi\varepsilon_0 r}\boldsymbol{r}, \tag{6.32}$$

where $\boldsymbol{E_0}$, ρ_ℓ, ε_0 and r denote the external electrostatic field, charge density of the cylinder, vacuum permittivity and the distance between the point and the cylinder respectively. Given the electrostatic field, the method of images is now employed to determine the electrostatic potential of the system which is guaranteed by the theorem of uniqueness. The cross section of the tube and its image is illustrated in Fig. 6.10. Before solving this problem, let us first consider a simpler case, i.e. the potential of a line charge and a conducting cylinder, which is shown in Fig. 6.11. The potential of any line charge V is given by

$$V = -\int_{r_0}^{r} E_r dr = -\frac{\rho_l}{2\pi\epsilon_0}\int_{r_0}^{r}\frac{1}{r}dr = \frac{\rho_l}{2\pi\epsilon_0}\ln\frac{r_0}{r}, \tag{6.33}$$

where we have utilized Eq. (6.32) to obtain Eq. (6.33). For the time being we initially ignore the value of the reference position r_0. At the point M on the cylindrical surface, which is shown in Fig. 6.10, the potential at M, V_M, can be expressed as

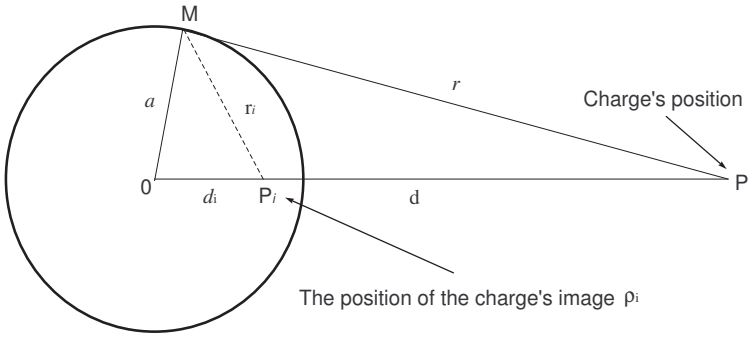

Figure 6.10: A geometric picture of the real charge and its image charge.

$$V_M = \frac{\rho_l}{2\pi\epsilon_0}\ln\frac{r_0}{r} - \frac{\rho_l}{2\pi\epsilon_0}\ln\frac{r_0}{r_i} = \frac{\rho_l}{2\pi\epsilon_0}\ln\frac{r_i}{r}. \tag{6.34}$$

Since V_M is constant on the equipotent surface, i.e. $r_i/r =$ constant, it is easy to observe that OMP_i and MP_iP are two similar triangles, so that

$$\frac{\overline{P_iM}}{\overline{PM}} = \frac{\overline{OP_i}}{\overline{OM}} = \frac{\overline{OM}}{\overline{OP}}. \tag{6.35}$$

Thus, we obtain $d_i = a^2/d$ and from which we can determine the image charge's position d_i in terms of a and d. Now, let us consider the electrostatic potential of two co-axial cylinders again and its geometry can be represented by a pair of line charges ρ_l and $-\rho_l$ (image) separated by the distance $D - 2d_i$ (see again Fig. 6.11 for details). By letting V_1 and V_2 be the potentials at M, caused by the line charges $-\rho_l$ and ρ_l respectively, then

$$V_1 = \frac{-\rho_l}{2\pi\epsilon_0}\ln\left(\frac{a}{d}\right), \qquad V_2 = \frac{\rho_l}{2\pi\epsilon_0}\ln\left(\frac{a}{d}\right), \tag{6.36}$$

where the expression of the electrostatic potential originates from Eq. (6.34). Next, the capacitance per unit length c is then given by

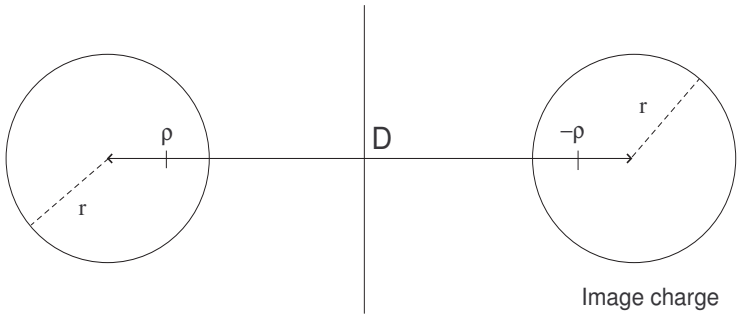

Figure 6.11: Method of images.

$$c = \left| \frac{\rho_l}{V_1 - V_2} \right| = \frac{\rho_l}{(\rho_l/\pi\epsilon_0)\ln(a/d)} = \frac{\pi\epsilon_0}{\ln(d/a)}, \tag{6.37}$$

so that upon rewriting d in terms of D and a, we find

$$d = D - d_i = D - \frac{a^2}{d} \quad \Rightarrow \quad d = \frac{1}{2}[D + \sqrt{D^2 - 4a^2}]. \tag{6.38}$$

Eq. (6.38) is then substituted back into Eq. (6.37) to obtain

$$c = \frac{\pi\epsilon_0}{\ln[(D/2a) + \sqrt{(D/2a)^2 - 1}]}.$$

Since $D \gg 2a$, it is legitimate to approximate c by $c = (\pi\epsilon_0)/\ln(D/a)$ and further, given $D = 2R - 2y$ and Gauss's unit ($4\pi\epsilon_0 = 1$) is utilized, $c(y)$ becomes

$$c(y) = \frac{1}{2\ln[2(R-y)/a]}. \tag{6.39}$$

6.7 Derivation of first integral for $F(y, y', y'')$

We determine the first integral for $F(y, y', y'')$. From the variational principle, the action can be defined as

$$S[y] = \int_0^{2L} F(x, y, y', y'')dx, \tag{6.40}$$

$\delta S[y]$ becomes

$$\delta S = \int_0^{2L} \left\{ \frac{\partial F}{\partial x}\delta x + \frac{\partial F}{\partial y}\delta y + \frac{\partial F}{\partial y'}\delta y' + \frac{\partial F}{\partial y''}\delta y'' \right\} dx. \tag{6.41}$$

Upon assuming $\delta y = \epsilon y'$ and utilizing the integration by parts, Eq. (6.41) becomes

$$\begin{aligned}\delta S = &\left[\left(y'\frac{\partial F}{\partial y''} + y'\frac{\partial F}{\partial y'} + y''\frac{\partial F}{\partial y''} - y'\frac{d}{dx}\frac{\partial F}{\partial y''} \right)\epsilon \right]_0^{2L} \\ &+ \int_0^{2L} \left\{ \frac{dF}{dx} - y'\frac{d}{dx}\frac{\partial F}{\partial y'} - y''\frac{\partial F}{\partial y'} - y'''\frac{\partial F}{\partial y''} + y'\frac{d^2}{dx^2}\frac{\partial F}{\partial y''} \right. \\ &\left. + y''\frac{d}{dx}\frac{\partial F}{\partial y''} - y''\frac{d}{dx}\frac{\partial F}{\partial y''} \right\}\delta y dx. \end{aligned} \tag{6.42}$$

which gives rise to the so-called natural boundary conditions and the Euler-Lagrange equation becomes

$$F_y - \frac{d}{dx}F_{y'} + \frac{d^2}{dx^2}F_{y''} = 0. \tag{6.43}$$

Eq. (6.42) is an identity for an arbitrary δy and the integrated-out terms give rise to the natural boundary conditions, which in the context of the appendix, give rise to the bending moment and the shear force of the buckled beam respectively. Assuming that the integrated-out terms are zero, upon collecting terms, we have

$$\delta S = \int_0^{2L} \delta y \frac{d}{dx}\left\{ F - y' \frac{\partial F}{\partial y'} - y'' \frac{\partial F}{\partial y''} + y' \frac{d}{dx}\frac{\partial F}{\partial y''} \right\} dx. \tag{6.44}$$

Since $\delta S = 0$ for the stationary point y and $\epsilon \neq 0$, we end up with the first integral

$$F - y' \frac{\partial F}{\partial y'} - y'' \frac{\partial F}{\partial y''} + y' \frac{d}{dx}\frac{\partial F}{\partial y''} = C_1, \tag{6.45}$$

where C_1 is an arbitrary constant.

6.8 Compatibility between the numerical and approximate solutions

We show how to reduce Eq. (3.21) into the approximate solution (3.16) by letting $y' \approx 0$ and neglecting the first derivative term of y, i.e. $y'^2 = 0$. Upon assuming this, we write

$$y''^2 - 2\xi^2 + F_0(y - xy') = c. \tag{6.46}$$

We note that although Eq. (6.46) is non-linear but not elementary. We can reduce it into a linear ordinary equation by differentiating equation (6.46) and again set $y' = 0$ to obtain

$$y''' = \frac{F_0}{2}. \tag{6.47}$$

Then y admits the following simple solution form

$$y = \frac{F_0}{48}x^4 + ax^2 + bx^2 + c, \tag{6.48}$$

where a, b and c denote integration constants. Upon substituting the Cauchy boundary conditions into Eq. (6.48), we obtain

$$y = \frac{F_0}{48}(x^2 - L^2)^2. \tag{6.49}$$

It is then easy to infer that y_{max} is equal to

$$y_{max} = y(0) = \frac{F_0}{48}L^4 = 0.013\frac{(neL)^2}{ERr^4}, \tag{6.50}$$

which is approximately equal to the Eq. (3.21).

6.9 Derivation of the constant c from molecular interactions

We analytically determine the value of c from the interactions between an atom on the inner nanotube and all the atoms on the outer nanotube. We follow the same approach as that adopted by He et al. [56] but we express c in terms of a hypergeometric function. In a cylindrical coordinate system, the location of the atom is assumed given by $(R_i, 0, 0)$ and the location of an atom on the outer tube is taken to be $(R_j\cos\theta, R_j\sin\theta, Z)$ (see Fig. 6.12), such that the distance between the atom on the inner tube and the atom on the outer tube d_0 can then be written as

$$\rho_0 = \sqrt{(R_j\cos\theta - R_i)^2 + R_j^2\sin^2\theta + Z^2} = \sqrt{\lambda^2 + Z^2}, \tag{6.51}$$

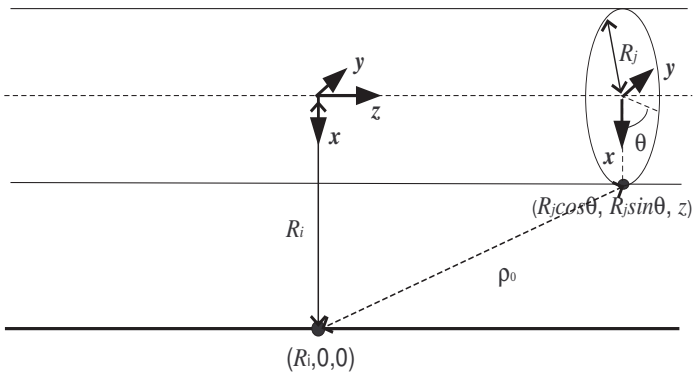

Figure 6.12: Schematic of tube layers.

where $\lambda^2 = (R_j - R_i)^2 + 4R_iR_j \sin^2\psi$, and $\psi = \theta/2$. We now utilize the Lennard-Jones potential in the following form

$$V(d) = 4\varepsilon \left[\left(\frac{\sigma}{\rho}\right)^{12} - \left(\frac{\sigma}{\rho}\right)^{6} \right], \tag{6.52}$$

where ρ, ε and σ denote the distance between the interacting atoms, the well depth and the van der Waals diameter. The van der Waals forces $F(\rho)$ can then be obtained from the derivative of Eq. (6.52), namely

$$F(\rho) = -\frac{dV(\rho)}{d\rho} = \frac{24\varepsilon}{\sigma} \left[2\left(\frac{\sigma}{\rho}\right)^{13} - \left(\frac{\sigma}{\rho}\right)^{7} \right]. \tag{6.53}$$

The initial pressure contribution p_{ij}, caused by the van der Waals interaction, can then be written by

$$p_{ij} = \left(\frac{4\sqrt{3}}{9d_{cc}^2}\right) \frac{24\varepsilon}{\sigma} \int_{-\pi}^{\pi} \int_{-L/2}^{L/2} \left[2\left(\frac{\sigma}{\rho_0}\right)^{13} - \left(\frac{\sigma}{\rho_0}\right)^{7} \right] R_j dz d\theta, \tag{6.54}$$

where d_{cc} and $9d_{cc}^2/(4\sqrt{3})$ denote the carbon-carbon bond length and the effective surface area of the carbon atom, respectively. Now we only consider infinitesimal buckling of the nanopeapods around an equilibrium configuration so that the Taylor expansion of the Lennard-Jones potential around the equilibrium position ρ_0 can be obtained as $V(\rho) = V(\rho_0) + (1/2)(d^2V(\rho_0)/d\rho^2)(\rho - \rho_0)^2 + O(\rho - \rho_0)^3$. Hence,

$\Delta V(\rho) = (1/2)(d^2V(\rho_0)/d\rho^2)(\rho - \rho_0)^2$. Upon knowing $F = -dV/d\rho$ and utilizing Eq. (6.54), the pressure increment Δp_{ij} due to this buckling deflection can be written by

$$\begin{aligned}\Delta p_{ij} &= \frac{dp_{ij}}{d\rho}(\rho_0)(\rho - \rho_0) \approx \frac{dp_{ij}}{d\rho}(\rho_0)(\omega_i - \omega_j), \\ &= -\left(\frac{4\sqrt{3}}{9d_{cc}^2}\right)\left(\frac{24\varepsilon}{\sigma^2}\right)\int_{-\pi}^{\pi}\int_{-L/2}^{L/2}\left[26\left(\frac{\sigma}{\rho_0}\right)^{14} - 7\left(\frac{\sigma}{\rho_0}\right)^{8}\right](\omega_i - \omega_j)R_j dz d\theta.\end{aligned} \tag{6.55}$$

In order to evaluate Eq. (6.55) analytically, we need to evaluate the following integrals for $n = 4$ and 7,

$$I_n = \int_{-\pi}^{\pi}\int_{-L/2}^{L/2}\frac{dz d\theta}{\rho_0^{2n}} = \int_{-\pi}^{\pi}\int_{-L/2}^{L/2}\frac{1}{(\lambda^2 + Z^2)^n}dz d\theta, \tag{6.56}$$

where we have utilized Eq. (6.51) and $\lambda^2 = (R_i + R_j)^4 - 4R_iR_j\cos(\theta/2)$. After substituting $Z = \lambda\tan\xi$ and letting the L goes to infinity, we obtain

$$I_n = \frac{2\pi}{(R_i + R_j)^{2n-1}}F\left(\frac{2n-1}{2}, \frac{1}{2}, 1; 1 - \left(\frac{R_i - R_j}{R_i + R_j}\right)^2\right)\int_0^{\pi/2}\cos^{2(n-1)}\xi d\xi, \tag{6.57}$$

where $F(a, b; c; z)$ denotes the usual hypergeometric function. Upon comparing Eq. (6.55) with Eq. (3.27), we may deduce that

$$c_i = 24\varepsilon\sigma^6\left(\frac{4\sqrt{3}}{9d_{cc}^2}\right)\left(26\sigma^6 I_7 - 7I_4\right)R_i. \tag{6.58}$$

On substituting all the parameters into Eq. (6.58), we obtain $c = c_1 = 0.23 \times 10^{18}$ Nm^{-3} and $c_2 = 0.37 \times 10^{18}$ Nm^{-3}.

6.10 Obtaining ϵ from minimization

From Eq. (4.44), if N_{max} is sufficiently large, then we can approximate the summation by integration. Upon utilizing equation Eq. (4.42), we obtain

$$
\begin{aligned}
E_{max} &= \frac{1}{2}k_c\left(\frac{\Phi-s}{\epsilon}\right)\left\{\left(\delta-\frac{\ell_c}{\Phi-s}\epsilon\right)^2+\left[\delta+\left(1-\frac{\ell_c}{\Phi-s}\right)\epsilon\right]^2\right\} \\
&+ \int_0^{\frac{\Phi-s}{\epsilon}}\frac{1}{2}k_g\left\{\sqrt{(s+\epsilon x)^2+\ell_g^2}-\ell_g\right\}^2 dx \\
&+ \int_0^{\frac{\Phi-s}{\epsilon}}\frac{L^2}{4}k_g\left\{1-\frac{\sqrt{(s+\epsilon x)^2+\ell_g^2}-\ell_g}{L}\right\}^{-1} dx \\
&- \int_0^{\frac{\Phi-s}{\epsilon}}\frac{L}{4}k_g\left\{\sqrt{(s+\epsilon x)^2+\ell_g^2}-\ell_g\right\} dx, \qquad (6.59)
\end{aligned}
$$

where $\Phi=\sqrt{K^2-\ell_g^2}$. If we substitute $s+\epsilon x=\ell_g\tan\theta$ and perform the integration, we obtain

$$
E_{max}=\frac{1}{2}k_c\left(\frac{\Phi-s}{\epsilon}\right)\left\{\left(\delta-\frac{\ell_c}{\Phi-s}\epsilon\right)^2\left[\delta+\left(1-\frac{\ell_c}{\Phi-s}\right)\epsilon\right]^2\right\}+\frac{H(s)}{\epsilon}, \quad (6.60)
$$

where $H(s)=(1/2)k_g\ell_g^3a(s)+(L^2/4)k_g\ell_g b(s)-(L/4)k_g\ell_g^2c(s)$ and

$$
\begin{aligned}
a(s) &= 2\tan\theta+\frac{1}{3}\tan^3\theta-\tan\theta\sec\theta-\ln(\sec\theta+\tan\theta)\Big|_{\arctan(s/\ell_g)}^{\arctan(\Phi/\ell_g)}, \\
b(s) &= \frac{L}{\ell_g}\ln\left(\frac{\tan\frac{\theta}{2}-1}{\tan\frac{\theta}{2}+1}\right)+2L\left(1+\frac{L}{\ell_g}\right)\frac{\arctan\left[\frac{(L+2\ell_g)\tan\frac{\theta}{2}}{\sqrt{L(L+2\ell_g)}}\right]}{\sqrt{L(L+2\ell_g)}}\Big|_{\arctan(s/\ell_g)}^{\arctan(\Phi/\ell_g)}, \\
c(s) &= \frac{1}{2}\tan\theta+\frac{1}{2}\ln(\tan\theta+\sec\theta)-\tan\theta\Big|_{\arctan(s/\ell_g)}^{\arctan(\Phi/\ell_g)}.
\end{aligned} \qquad (6.61)
$$

We note that the energy form given in Eq. (6.60) might be utilized to carry out computer simulations or mathematical modelings for CTs in a more accurate way. To find the minimum value of E_{max} with respect to ϵ, we require $\partial E_{max}/\partial\epsilon=0$. Given that, we have

$$\epsilon = \sqrt{\frac{2\left[\delta^2 + \frac{H}{k_c(\Phi - s)}\right]}{\left[\left(\frac{\ell_c}{\Phi - s}\right)^2 + \left(1 - \frac{\ell_c}{\Phi - s}\right)^2\right]}}. \tag{6.62}$$

Upon knowing s, ϵ can be easily solved from the above equation.

Bibliography

[1] S. Akita, Y. Nakayama, S. Mizooka, Y. Takano, T. Okawa, Y. Miyatake, S. Yamanaka, M. Tsuji, and T. Nosaka. Nanotweezers consisting of carbon nanotubes operating in an atomic force microscope. *Appl. Phys. Lett.*, 79:1691–1693, 2001.

[2] O. Akkus. Elastic deformation of mineralized collagen fibrils: An equivalent inclusion based composite model. *J. Biomech. Eng.*, 127:383–390, 2005.

[3] H. G. Allen and P. S. Bulson. *Background to buckling.* McGraw-Hill, UK, 1980.

[4] M. Ya. Amusia and A. S. Baltenkov. On the possibility of considering the fullerene shell C_{60} as a conducting sphere. *Phys. Lett. A*, 360:294–298, 2006.

[5] A. J. Bailey, S. F. Wotton, T. J. Sims, and P. W. Thompson. Post-translational modifications in the collagen of human osteoporotic femoral head. *Biochem. Biophys. Res. Commun.*, 185:801–805, 1992.

[6] X. Banse, T. J. Sims, and A. J. Bailey. Mechanical properties of adult vertebral cancellous bone: Correlation with collagen intermolecular corss-links. *J. Bone Miner. Res.*, 17:1621–1628, 2002.

[7] D. Baowan and J. M. Hill. Accurate expressions for the force distribution for double-walled carbon nanotubes. *Z. Angew. Math. Phys.*, 58:857, 2007.

[8] D. Baowan, N. Thamwattana, and J. M. Hill. Zigzag and spiral configurations

for fullerenes in carbon nanotubes. *J. Phys. A: Math. Theor.*, 40:7543–7556, 2007.

[9] S. E. Barrows, F. J. Dulles, C. J. Cramer, A. D. French, and D. G. Truhlar. Relative stability of alternative chair forms and hydroxymethyl conformations of β-$_D$-glucopyranose. *Carbohydr. Res.*, 276:219–251, 1995.

[10] R. H. Baughman, C. X. Cui, A. A. Zakhidov, Z. Iqbal, J. N. Barisci, G. M. Spinks, G. G. Wallace, A. Mazzoldi, D. De Rossi, A. G. Rinzler, O. Jaschinski, S. Roth, and M. Kertesz. Carbon nanotube actuators. *Science*, 284:1340–1344, 1999.

[11] C. G. Baumann, V. A. Bloomfield, S. B. Smith, C. Bustamante, M. D. Wang, and S. M. Block. Stretching of single collapsed DNA molecules. *Biophys. J.*, 78:1965–1978, 2000.

[12] K. Behfar and R. Naghdabadi. Nanoscale vibration analysis of a multi-layered graphene sheet embedded in an elastic medium. *Compos. Sci. Technol.*, 65:1159–64, 2005.

[13] S. Berber, Y. K. Kwon, and D. Tomanek. Microscopic formation mechanism of nanotube peapods. *Phys. Rev. Lett.*, 88:185502–1, 2002.

[14] G. Binning, H. Rohrer, and Ch. Gerber. Atomic force microscope. *Phys. Rev. Lett.*, 56:930, 1986.

[15] G. Binning, H. Rohrer, Ch. Gerber, and E. Weibel. Surface studies by scanning tunneling microscopy. *Phys. Rev. Lett.*, 49:57, 1982.

[16] N. M. Bou-Rabee, J. E. Marsden, and L. A. Romero. Tippe top inversion as a dissipation-induced instability. *SIAM J. Appl. Dyn. Syst.*, 3:352–377, 2004.

[17] F. Bowman. *Introduction to elliptic functions: With applications*. Dover Publications, 1st edition, 1961.

[18] C. M. Braams. On the influence of friction on the motion of a top. *Physica*, 18:503–514, 1952.

[19] M. J. Buehler. Nature designs tough collagen: Explaining the nanostructure of collagen fibrils. *PNAS*, 103:12285–12290, 2006.

[20] R. L. Burden and J. D. Faires. *Numerical Analysis*. Thomson, 1st edition, 2005.

[21] D. B. Burr. The contribution of the organic matrix to bone's materials properties. *Bone*, 31:8–11, 2002.

[22] H. J. Butt, B. Cappella, and M. Kappl. Force measurements with the atomic force microscope: Technique, interpretation and applications. *Surf. Sci. Rep.*, 59:1–152, 2005.

[23] S. N. Cha, J. E. Jang, Y. Choi, G. A. J. Amaratunga, D. J. Kang, D. G. Hasko, J. E. Jung, and J. M. Kim. Fabrication of a nanoelectromechanical switch using a suspended carbon nanotube. *Appl. Phys. Lett.*, 86:083105, 2005.

[24] A. N. Cleland. *Foundations of nanomechanics*. Springer-Verlag, 1st edition, 2003.

[25] R. J. Cohen. The tippe top revisited. *Amer. J. Phys.*, 45:12, 1977.

[26] F. D. Colavecchia, G. Gasaneo, and J. E. Miraglia. Numerical evaluation of Appell's F_1 hypergeometric function. *Comput. Phys. Commun.*, 138:29–43, 2001.

[27] B. J. Cox, N. Thamwattana, and J. M. Hill. Mechanics of atoms and fullerenes in single-walled carbon nanotubes. I. Acceptance and suction energies. *Proc. R. Soc. A*, 463:461, 2007.

[28] B. J. Cox, N. Thamwattana, and J. M. Hill. Mechanics of atoms and fullerenes in single-walled carbon nanotubes. II. Oscillatory behaviour. *Proc. R. Soc. A*, 463:477, 2007.

[29] B. J. Cox, N. Thamwattana, and J. M. Hill. Mechanics of fullerenes oscillating in carbon nanotube bundles. *J. Phys. A: Math. Theor.*, 40:13197, 2007.

[30] B. J. Cox, N. Thamwattana, and J. M. Hill. Mechanics of nanotubes oscillating in carbon nanotube bundles. *Proc. Roy. Soc. London A*, 646:691, 2008.

[31] J. Cumings and A. Zettl. Low-friction nanoscale linear bearing realized from multiwall carbon nanotubes. *Science*, 289:602, 2000.

[32] G. V. Dedkov. Friction on the nanoscale: New physical mechanisms. *Mater. Lett.*, 38:360–366, 1999.

[33] G. V. Dedkov and A. A. Kyasov. Electromagnetic friction forces on the scanning proble asperity moving near surface. *Phys. Lett. A*, 259:38–42, 1999.

[34] M. Dequesnes, S. V. Rotkin, and N. R. Aluru. Calculation of pull-in voltages for carbon-nanotube-based nanoelectromechanical switches. *Nanotechnology*, 13:120–131, 2002.

[35] M. K. Dowd, A. D. French, and P. J. Reilly. Modeling of aldopyranosyl ring puckering with MM3. *Carbohydr. Res.*, 264:1–19, 1994.

[36] M. S. Dresselhaus, G. Dresselhaus, and P. Avouris. *Carbon nanotubes*. Springer, 1st edition, 2001.

[37] M. S. Dresselhaus, G. Dresselhaus, and P. C. Eklund. *Science of fullerenes and carbon nanotubes*. Academic Press, San Diego, 1st edition, 1996.

[38] S. Ebenfeld and F. Scheck. A new analysis of the tippe top: Asymptotic states and liapunov stability. *Ann. Phys.*, 243:195–217, 1995.

[39] A. Erbe, C. Weiss, W. Zwerger, and R. H. Blick. Nanomechanical resonator shuttling single electrons at radio frequencies. *Phys. Rev. Lett.*, 87:096106, 2001.

[40] B. Fain, J. Rudnick, and S. Ostlund. Conformations of linear dna. *Phys. Rev. E*, 55:7364–7368, 1997.

[41] M. R. Falvo, R. M. Taylor, A. Helser, V. Chi, F. P. Brooks, S. Washburn, and R. Superfine. Nanometre-scale rolling and sliding of carbon nanotubes. *Nature*, 397:236, 1999.

[42] F. Family, H. G. E. Hentschel, and Y. Braiman. Friction at the nanoscale. *J. Phys. Chem. B*, 104:3984–3987, 2000.

[43] M. Fixman and J. Kovac. Polymer conformational statistics. III. Modified gaussian models of stiff chains. *J. Chem. Phys.*, 58:1564–1568, 1973.

[44] N. R. Franklin, Q. Wang, T. W. Tombler, A. Javey, M. Shim, and H. Dai. Integration of suspended carbon nanotube arrays into electronic devices and electromechanical systems. *Appl. Phys. Lett.*, 81:913–915, 2002.

[45] A. Fritsch and C. Hellmich. 'Universal' microstructural patterns in cortical and trabecular, extracellular bone materials, micromechanics-based prediction of anisotropic elasticity. *J. Theor. Biol.*, 244:597–620, 2007.

[46] Y. Gan, J. Kotakoski, A. V. Krasheninnikov, K. Nordlund, and F. Banhart. The diffusion of carbon atoms inside carbon nanotubes. *New J. Phys.*, 10:023022, 2008.

[47] D. Garcia-Sanchez, A. S. Paulo, M. J. Esplandiu, F. Perez-Murano, L. Forro, A. Aguasca, and A. Bachtold. Mechanical detection of carbon nanotube resonator vibrations. *Phys. Rev. Lett.*, 99:085501, 2007.

[48] M. Goldberg. A class of multi-symmetric polyhedra. *Tohoku Mathematical Journal*, 43:104–108, 1937.

[49] H. Goldstein, C. Poole, and J. Safko. *Classical Mechanics*. Addison Wesley, 3rd edition, 2002.

[50] S. Govindjee and J. L. Sackman. On the use of continuum mechanics to estimate the properties of nanotubes. *Solid State Commun.*, 110:227–230, 1999.

[51] C. G. Gray and B. G. Nickel. Constants of the motion for nonslipping tippe tops and other tops with round pegs. *Amer. J. Phys.*, 68:821–828, 2000.

[52] S. Haibin, A. G. III. William, and Z. Yang. Dynamic friction force in a carbon peapod oscillator. *Nanotechnology*, 17:5691–5695, 2006.

[53] Q. Han and G. Lu. Torsional buckling of a double-walled carbon nanotube embedded in an elastic medium. *Eur. J. Mech. A/Solids*, 22:875–83, 2003.

[54] R. G. Haverkamp, A. T. Marshall, and M. A. K. Williams. Model for stretching elastic biopolymers which exhibit conformational transformations. *Phys. Rev. E*, 75:021907, 2007.

[55] R. G. Haverkamp, M. A. K. Williams, and J. E. Scott. Stretching single molecules of connective tissue glycans to characterize their shape-maintaining elasticity. *Biomacromolecules*, 6:1816–1818, 2005.

[56] X. Q. He, S. Kitipornchai, and K. M. Liew. Buckling analysis of multi-walled carbon nanotubes: A continuum model accounting for van der waals interactions. *J. Mech. Phys. Solids*, 53:303–26, 2005.

[57] C. Hellmich, J. F. Barthelemy, and L. Dormieux. Mineral-collagen interactions in elasticity of bone ultrastructure-a continuum micromechanics approach. *Eur. J. Mech. A. Solids*, 23:783–810, 2004.

[58] S. J. Heo and S. B. Sinnott. Effect of molecular interactions on carbon nanotube friction. *J. Appl. Phys.*, 102:064307, 2007.

[59] C. J. Hernandez, S. Y. Tang, B. M. Baumbach, P. B. Hwu, A. N. Sakkee, F. van der Ham, J. DeGroot, R. A. Bank, and T. M. Keaveny. Trabecular

microfracture and the influence of pyridinium and non-enzymatic glycation-mediated collagen cross-links. *Bone*, 37:825–832, 2005.

[60] C. Hierold. From micro to nano systems: Mechanical sensors go nano. *J. Micromech. Microeng.*, 14:1–11, 2004.

[61] C. Hierold, C. Stampfer, T. Helbling, A. Jungen, M. Tripp, and D. Sarangi. The 8th symposium on micro- and nano-mechatronics for information-based society, the 21st century coe program, nagoya university, nagoya municipial industrial research institute, nagoya, japan. *In proceedings of the IEEE 2005 International symposium on micro-nano mechatronics and human science, MHS2005*, 8-9 Nov:1–4, 2005.

[62] T. A. Hilder and J. M. Hill. Orbiting atoms and C_{60} fullerenes inside carbon nanotori. *J. Appl. Phys.*, 101:064319, 2007.

[63] T. A. Hilder and J. M. Hill. Orbiting nanosectors inside carbon nanotori. *Micro & Nano Lett.*, 2:50, 2007.

[64] J. O. Hirschfelder, C. Curtiss, and R. B. Bird. *Molecular Theory of Gases and Liquids*. Wiley, 1st edition, 1954.

[65] N. M. Hugenholtz. On tops rising by friction. *Physica*, 18:515–527, 1952.

[66] S. Iijima. Helical microtubules of graphitic carbon. *Nature*, 354:56–58, 1991.

[67] A. Janshoff, M. Neitzert, Y. Oberdorfer, and H. Fuchs. Force spectroscopy of molecular systems - single molecule spectroscopy of polymers and biomolecules. *A. Chem. Int. Ed.*, 39:3213–3237, 2000.

[68] I. Jäger and P. Fratzl. Mineralized collagen fibrils: A mechanical model with a staggered arrangement of mineral particle. *Biophys. J.*, 79:1737–1746, 2000.

[69] A. Jeffrey and D. Zwillinger. *Table of Integrals Series and Products*. Academic Press Inc., New York, 6th edition, 1965.

[70] B. Ji and H. Gao. Mechanical properties of nanostructure of biological materials. *J. Mech. Phys. Solids*, 52:1963–1990, 2004.

[71] D. E. H. Jones. Hollow molecules. *New Sci.*, 32:245, 1966.

[72] L. M. Jonsson, L. Y. Gorelik, R. I. Shekhter, and M. Jonson. Electromechanical instability in suspended carbon nanotubes. *Nano Lett.*, 5:1165–1169, 2005.

[73] N. V. Joshi and V. S. R. Rao. Flexibility of the pyranose ring in α and β -glucoses. *Biopolymers*, 18:2993–3004, 1979.

[74] T. M. Keaveny, G. E. Morris, E. K. Wong, M. Yu, A. N. Sakkee, N. Verzijl, and R. A. Bank. Collagen status and brittleness of human cortical bone in the elderly. *J. Bone Miner. Res.*, 18:S307, 2003.

[75] G. T. Kim, G. Gu, U. Waizmann, and S. Roth. Simple method to prepare individual suspended nanofibers. *Appl. Phys. Lett.*, 80:1815–1817, 2002.

[76] P. Kim and C. M. Lieber. Nanotube nanotweezers. *Science*, 286:2148–2150, 1999.

[77] P. Kim, L. Shi, A. Majumdar, and P. L. McEuen. Thermal transport measurements of individual multiwalled nanotubes. *Phys. Rev. Lett.*, 87:215502, 2001.

[78] J. M. Kinaret, T. Nord, and S. Viefers. A carbon-nanotube-based nanorelay. *Appl. Phys. Lett.*, 82:1287–1289, 2003.

[79] E. Klipp, R. Herwig, A. Kowald, C. Wierling, and H. Lehrach. *Systems biology in practice: Concepts, implementation and application.* Wiley-VCH, 1st edition, 2005.

[80] A. N. Kolmogorov and V. H. Crespi. Smoothest bearings: Interlayer sliding in multiwalled carbon nanotubes. *Phys. Rev. Lett.*, 85:4727, 2000.

[81] S. P. Kotha and N. Guzelsu. Effect of bone mineral content on the tensile properties of cortical bone: Experiments and theory. *J. Biomech. Eng.*, 125:785–793, 2003.

[82] J. Kovac and C. C. Crabb. Modified gaussian model for rubber elasticity .2. the wormlike chain. *Macromolecules*, 15:537–541, 1982.

[83] H. W. Kroto. The stability of the fullerenes C_n , with $n = 24, 28, 32, 36, 50, 60$ and 70. *Nature*, 329:529, 1987.

[84] H. W. Kroto, J. R. Heath, S. C. O'Brien, R. F. Curl, and R. E. Smalley. C_{60}: Buckminsterfullerene. *Nature*, 318:162, 1985.

[85] M. Kuttel and K. J. Naidoo. Glycosidic linkage rotations determine amylose stretching mechanism. *J. Am. Chem. Soc.*, 127:12–13, 2005.

[86] A. A. Kyasov and G. V. Dedkov. Electromagnetic fluctuation interactions of moving particles with cylindrical surfaces. *Surf. Sci.*, 491:124–130, 2001.

[87] P. Y. Lai, G. Rowlands, and Z. Zhou. Worm-like chain under external forces: Some analytic results. *Chinese J. Phys.*, 42:410–422, 2004.

[88] L. D. Landau and E. M. Lifshifs. *Theory of Elasticity*. Pergamon, Oxford, 1st edition, 1986.

[89] S. Lees, D. R. Eyre, and S. M. Barnard. BAPN dose dependence of mature crosslinking in bone marix collagen of rabbit compact bone: Corresponding variation of sonic velocity and equatorial diffraction spacing. *Connective Tissue Research*, 24:95–105, 1990.

[90] S. B. Legoas, V. R. Coluci, S. F. Braga, P. Z. Coura, S. O. Dantas, and D. S. Galvao. Molecular-dynamics simulations of carbon nanotubes as gigahertz oscillators. *Phys. Rev. Lett.*, 90:055504, 2003.

[91] H. Leutwyler. Why some tops tip. *Eur. J. Phys.*, 15:59–61, 1994.

[92] C. Li and T. W. Chou. A structural flexibility of carbon nanotubes. *J. Solids and Struct.*, 40:2487–2499, 2003.

[93] K. M. Liew, C. H. Wong, X. Q. Hel, M. J. Tan, and S. A. Meguid. Nanomechanics of single and multiwalled carbon nanotubes. *Phys. Rev. B*, 69:115429, 2004.

[94] P. Liu, Y. W. Zhang, and C. Lu. Oscillatory behavior of C_{60}-nanotube oscillators: A molecular-dynamics study. *J. Appl. Phys.*, 97:094313, 2005.

[95] W. K. Liu, E. G. Karpov, S. Zhang, and H. S. Park. An introduction to computational nanomechanics and materials. *Comput. Methods Appl. Mech. Engrg.*, 193:1529–1578, 2004.

[96] J. Mahanty and B. W. Ninham. *Dispersion forces*. Academic Press, 1st edition, 1976.

[97] J. F. Marko and E. D. Siggia. Stretching dna. *Macromolecules*, 28:8759–8770, 1995.

[98] P. E. Marszalek, H. Li, and J. M. Fernandez. Fingerprinting polysaccharides with single-molecule atomic force microscopy. *Nat. Biotechnol.*, 19:258–262, 2001.

[99] P. E. Marszalek, Y. P. Pang, H. Li, J. E. Yazal, A. F. Oberhauser, and J. M. Fernandez. Atomic levers control pyranose ring conformations. *PNAS*, 96:7894–7898, 1999.

[100] D. V. Massimiliano, E. Stephane, and R. H. James Jr. *Introduction to Nanoscale Science and Technology*. Kluwer Academic Publishers, Boston, MA, 1st edition, 2004.

[101] K. Misof, G. Rapp, and P. Fratzl. A new molecular model for collagen elasticity based on synchrotron scattering evidence. *Biophys. J.*, 72:1376–1381, 1997.

[102] Y. Miyauchi, R. Saito, K. Sato, Y. Ohno, S. Iwasaki, T. Mizutani, J. Jiang, and S. Maruyama. Dependence of exciton transition energy of single-walled carbon nanotubes on surrounding dielectric materials. *Chem. Phys. Lett.*, 442:394, 2007.

[103] H. K. Moffatt and Y. Shimomura. Spinning eggs - a paradox resolved. *Nature*, 416:385–386, 2002.

[104] A. Naik, O. Buu, M. D. LaHaye, A. D. Armour, A. A. Clerk, M. P. Blencowe, and K. C. Schwab. Cooling a nanomechanical resonator with quantum back-action. *Nature*, 443:193–196, 2006.

[105] A. G. Nasibulin, P. V. Pikhitsa, H. Jiang, D. P. Brown, A. V. Krasheninnikov, A. S. Anisimov, P. Queipo, A. Moisala, D. Gonzalez, G. Lientschnig, A. Hassanien, S. D. Shandakov, G. Lolli, D. E. Resasco, M. Choi, D. Tománek, and E. I. Kauppinen. A novel hybrid carbon material. *Nat. Nanotechnol.*, 2:156–161, 2006.

[106] R. M. Neumann. Polymer stretching in an elongational flow. *J. Chem. Phys.*, 110:7513–7515, 1999.

[107] M. Nishio, S. Sawaya, S. Akita, and Y. Nakayama. Carbon nanotube oscillators toward zeptogram detection. *Appl. Phys. Lett.*, 86:133111, 2005.

[108] S. Niyogi, M. A. Hamon, H. Hu, B. Zhao, P. Bhowmik, R. Sen, M. E. Itkis, and R. C. Haddon. Chemistry of single-walled carbon nanotubes. *Acc. Chem. Res.*, 35:1105–1113, 2002.

[109] J. Nygard and D. H. Cobden. Quantum dots in suspended single-wall carbon nanotubes. *Appl. Phys. Lett.*, 79:4216–4218, 2001.

[110] G. M. Odegard, T. S. Gates, L. M. Nicholson, and K. E. Wise. Equivalent-continuum modeling of nano-structured materials. *Composites Sci. Technol.*, 62:1869–1880, 2002.

[111] T. W. Odom, J. L. Huang, P. Kim, and C. M. Lieber. Atomic structure and electronic properties of single-walled carbon nanotubes. *Nature*, 391:62–64, 1998.

[112] F. Oesterhelt, M. Rief, and H. E. Gaub. Single molecule force spectroscopy by AFM indicates helical structure of poly(ethylene-glycol) in water. *New J. Phys.*, 1:6.1–6.11, 1999.

[113] A. C. Or. The dynamics of a tippe top. *SIAM J. Appl. Math.*, 54:597–609, 1994.

[114] H. Oxlund, M. Barckmann, G. Ortoft, and T. T. Ancreassen. Reduced concentrations of collagen cross-links are associated with reduced strength of bone. *Bone*, 17:365S–371S, 1995.

[115] H. Oxlund, Li Mosekilde, and G. Ortoft. Reduced concentration of collagen reducible cross links in human trabecular bone with respect to age and osteoporosis. *Bone*, 19:479–484, 1996.

[116] A. Pantano, D. M. Parks, and M. C. Boyce. Mechanics of deformation of single- and multi-wall carbon nanotubes. *J. Mech. and Phys. Solids*, 52:789–821, 2004.

[117] H. B. Peng, C. W. Chang, S. Aloni, T. D. Yuzvinsky, and A. Zettl. Ultrahigh frequency nanotube resonators. *Phys. Rev. Lett.*, 97:087203, 2006.

[118] V. N. Popov. Curvature effects on the structural, electronic and optical properties of isolated single-walled carbon nanotubes within a symmetry-adapted non-orthogonal tight-binding model. *New J. Phys.*, 6:17, 2004.

[119] V. N. Popov and L. Henrard. Comparative study of the optical properties of single-walled carbon nanotubes within orthogonal and non-orthogonal tight-binding models. *Phys. Rev. B*, 70:115407, 2004.

[120] D. Qian, W. K. Liu, and R. S. Ruoff. Mechanics of C_{60} in nanotubes. *J. Phys. Chem. B*, 105:10753, 2001.

[121] A. Redaelli, S. Vesentini, M. Soncini, P. Vena, S. Mantero, and F. M. Montevecchi. Possible role of decorin glycosaminoglycans in fibril to fibril force transfer in relative mature tendons-a computational study from molecular to microstructural level. *J. Biomech.*, 36:1555–1569, 2003.

[122] B. Reulet, A. Y. Kasumov, M. Kociak, R. Deblock, II. Khodos, Y. B. Gorbatov, V. T. Volkov, C. Journet, and H. Bouchiat. Acoustoelectric effects in carbon nanotubes. *Phys. Rev. Lett.*, 85:2829–2832, 2000.

[123] M. Rief, J. M. Fernandez, and H. E. Gaub. Elastically coupled two-level systems as a model for biopolymer extensibility. *Phys. Rev. Lett.*, 81:21, 1998.

[124] M. Rief, F. Oesterhelt, B. Heymann, and H. E. Gaub. Single molecule force spectroscopy on polysaccharides by atomic force microscopy. *Science*, 275:1295–1297, 1997.

[125] J. L. Rivera, C. McCabe, and P. T. Cumming. Oscillatory behavior of double nanotubes under extension: A simple nanoscale damped spring. *Nano Lett.*, 3:1001, 2003.

[126] J. L. Rivera, C. McCabe, and P. T. Cumming. The oscillatory damped behaviour of incommensurate double-walled carbon nanotubes. *Nanotechnology*, 16:186, 2005.

[127] A. Rosa, T. Hoang, and D. Marenduzzo. A new interpolation formula for semiflexible polymers. *Biophys. Chem.*, 115:251–254, 2005.

[128] C. Q. Ru. Axially compressed buckling of a doublewalled carbon nanotube embedded in an elastic medium. *J. Mech. Phys. Solids*, 49:1265–79, 2001.

[129] T. Rueckes, K. Kim, E. Joselevich, G. Y. Tseng andC. L. Cheung, and C. M.

Lieber. Carbon nanotube-based nonvolatile random access memory for molecular computing. *Science*, 289:94–97, 2000.

[130] D. Rugar, R. Budakian, H. J. Mamin, and B. W. Chui. Single spin detection by magnetic resonance force microscopy. *Nature*, 430:329, 2004.

[131] R. S. Ruoff and D. C. Lorentz. Mechanical and thermal properties of carbon nanotubes. *Carbon*, 33:925–930, 1995.

[132] R. Saito, G. Dresselhous, and M. S. Dresselhous. *Physical properties of carbon nanotubes*. Imperial College Press, London, 1st edition, 1998.

[133] J. P. Salvetat, J. M. Bonard, N. H. Thomson, and A. J. Kulik. Mechanical properties of carbon nanotubes. *Appl. Phys. A*, 69:255–260, 1999.

[134] S. Sapmaz, Y. M. Blanter, L. Gurevich, and H. S. J. van der Zhant. Carbon nanotubes as nanoelectromechanical systems. *Phys. Rev. B*, 67:235414, 2003.

[135] V. Sazonova, Y. Yaish, H. Ustunel, D. Roundy, T. A. Arias, and P. L. McEuen. A tunable carbon nanotube electromechanical oscillator. *Nature*, 431:284–287, 2004.

[136] T. G. Schmalz, W. A. Seitz, D. J. Klein, and G. E. Hite. Elemental carbon cages. *J. Am. Chem. Soc.*, 110:1113, 1988.

[137] A. V. Schneidemesser, G. Thummes, and C. Heiden. Generation of liquid helium temperatures using a lead regenerator in a GM precooled pulse tube stage. *Cryogenics*, 40:67, 2000.

[138] K. C. Schwab and M. L. Roukes. Putting mechanics into quantum mechanics. *Phys. Today*, July:36, 2005.

[139] J. E. Scott. Composition and structure of the pericellular environment: Physiological function and chemical composition of pericellular proteoglycan (an evolutionary view). *Philos. Trans. R. Soc. Lond. B. Biol. Sci.*, 271:235–242, 1975.

[140] J. E. Scott. Proteoglycan-fibrillar collagen interactions. *Biochem. J.*, 252:313–323, 1988.

[141] J. E. Scott. Proteoglycan: Collagen interactions and corneal ultrastructure. *Biochem. Soc. Trans.*, 19:877–881, 1991.

[142] J. Servantie and P. Gaspard. Translational dynamics and friction in double-walled carbon nanotubes. *Phys. Rev. B*, 73:125428, 2006.

[143] H. Shen. Compressive and tensile properties of air filled carbon nano-peapods. *Mater. Lett.*, 61:527, 2007.

[144] I. L. Singer and H. M. Pollock. *Fundamentals of friction.* Dordrecht, Boston, 1st edition, 1992.

[145] B. W. Smith, M. Monthioux, and D. E. Luzzi. Encapsulated C_{60} in carbon nanotubes. *Nature*, 396:232–234, 1998.

[146] W. B. Smith and E. D. Luzzi. Formation mechanism of fullerene peapods and coaxial tube: A path to large scale synthesis. *Chem. Phys. Lett.*, 321:169–174, 2000.

[147] A. N. Sohi and R. Naghdabadi. Torsional buckling of carbon nanopeapods. *Carbon*, 45:952–957, 2007.

[148] A. N. Sohi and R. Naghdabadi. Stability of single-walled carbon nanopeapods under combined axial compressive load and external pressure. *Physica E*, 41:513–517, 2009.

[149] M. R. Spiegel and J. Liu. *Mathematical Handbook of Formulas and Tables.* McGraw-Hill, international edition, 1999.

[150] C. Stampfer, T. Helbling, D. Obergfell, B. Schoberle, M. K. Tripp, A. Jungen, S. Roth, V. M. Bright, and C. Hierold. Fabrication of single-walled-carbon-nanotube-based pressure sensors. *Nano Lett.*, 6:233–237, 2006.

[151] C. Stampfer, A. Jungen, R. Linderman, D. Obergfell, S. Roth, and C. Hierold. Nano-electromechanical displacement sensing based on single-walled carbon nanotubes. *Nano Lett.*, 6:1449–1453, 2006.

[152] C. Storm and P. C. Nelson. Theory of high-force dna stretching and overstretching. *Phys. Rev. E*, 67:051906, 2003.

[153] K. Svoboda, F. Schmidt, S. M. Block, and B. J. Schnapp. Direct observation of kinesin stepping by optical trapping interferometry. *Nature*, 365:721–727, 1993.

[154] S. P. Timoshenko and J. M. Gere. *Theory of elastic stability.* McGraw-Hill, New York, 1961.

[155] T. W. Tombler, C. Zhou, L. Alexseyev, J. Kong, H. Dai, L. Liu, C. S. Jayanthi, M. Tang, and S. Y. Wu. Reversible electromechanical characteristics of carbon nanotubes under local-probe manipulation. *Nature*, 405:769–772, 2000.

[156] R. E. Tuzun, D. W. Noid, B. G. Sumpter, and R. C. Merkle. Dynamics of He/C_{60} flow inside carbon nanotubes. *Nanotechnology*, 8:112–118, 1997.

[157] T. Ueda, K. Sasaki, and S. Watanabe. Motion of the tippe top: Gyroscopic balance condition and stability. *SIAM J. Appl. Dyn. Syst.*, 4:1159–1194, 2005.

[158] H. Ulbricht and T. Hertel. Dynamics of C_{60} encapsulation into single-wall carbon nanotubes. *J. Phys. Chem. B*, 107:14185–90, 2003.

[159] H. Ulbricht, G. Moos, and T. Hertel. Interaction of C_{60} with carbon nanotubes and graphite. *Phys. Rev. Lett.*, 90:095501, 2003.

[160] M. D. Wang, H. Yin, R. Landick, J. Gelles, and S. M. Block. Stretching dna with optical tweezers. *Biophys. J.*, 72:1335–1346, 1997.

[161] Q. Wang. Torsional instability of carbon nanotubes encapsulating C_{60} fullerenes. *Carbon*, 47:507–512, 2009.

[162] X. Wang and C. Qian. Prediction of microdamage formation using a mineral-collagen composite model. *J. Biomech.*, 39:595–602, 2006.

[163] X. Wang, X. Shen, X. Li, and C. M. Agrawal. Age-related changes in the collagen network and toughness of bone. *Bone*, 31:1–7, 2002.

[164] X. Wang and H. K. Yang. Bending stability of multiwalled carbon nanotubes. *Phys. Rev. B*, 73:085409, 2006.

[165] Y. Wang, G. T. Hager, and P. C. Eklund. Interband dielectric function of C_{60} and M_6C_{60} (M=K, Rb, Cs). *Phys. Rev. B*, 45:24, 1992.

[166] M. Wautelet. Scaling laws in the macro-, micro- and nanoworlds. *Eur. J. Phys.*, 22:601–611, 2001.

[167] E. T. Whittaker and G. N. Watson. *A course of modern analysis*. Cambridge University Press, 1st edition, 1990.

[168] P. A. Williams, S. J. Papadakis, M. R. Falvo, A. M. Patel, M. Sinclair, A. Seeger, A. Helser, R. M. Taylor, S. Washburn, and R. Superfine. Controlled placement of an individual carbon nanotube onto a microelectromechanical structure. *Appl. Phys. Lett.*, 80:2574–2576, 2002.

[169] B. Witkamp, M. Poot, and H. S. J. van der Zant. Bending-mode vibration of a suspended nanotube resonator. *Nano Lett.*, 6:2904, 2006.

[170] R. A. Wood, M. H. Lewis, M. R. Lees, S. M. Bennington, M. G. Cain, and N. Kitamura. Ferromagnetic fullerene. *J. Phys.: Condens. Matter*, 14:385–391, 2002.

[171] B. I. Yakobson, C. J. Brabec, and J. Bernholc. Nanomechanics of carbon tubes: Instabilities beyond linear response. *Phys. Rev. Lett.*, 76:2511–2514, 1996.

[172] H. Yamakawa. Statistical mechanics of wormlike chains. *Pure Appl. Chem.*, 46:135–141, 1976.

[173] H. K. Yang and X. Wang. Torsional buckling of multi-walled carbon nanotubes embedded in an elastic medium. *Compos. Struct.*, 77:182–92, 2007.

[174] Z. Yao, H. W. C. Postma, L. Balents, and C. Dekker. Carbon nanotube intramolecular junctions. *Nature*, 402:273–276, 1999.

[175] J. Yoon, C. Q. Ru, and A. Mioduchowski. Vibration of an embedded multiwall carbon nanotube. *Composite Sci. Technol.*, 63:1533–1545, 2003.

[176] M. Yoshida and E. Osawa. Molecular mechanics calculations of giant- and hyperfullerenes with eicosahedral symmetry. *Fullerene Science & Technology*, 1:55–74, 1993.

[177] M. F. Yu, B. I. Yakobson, and R. S. Ruoff. Controlled sliding and pullout of nested shells in individual multiwalled carbon nanotubes. *J. Phys. Chem. B*, 104:8764, 2000.

[178] H. W. Zhang, L. Wang, and J. B. Wang. Computer simulation of buckling behavior of double-walled carbon nanotubes with abnormal interlayer distances. *Comput. Mater. Sci.*, 39:664, 2007.

[179] Q. Zheng and Q. Jiang. Multiwalled carbon nanotubes as gigahertz oscillators. *Phys. Rev. Lett.*, 88:045503, 2002.

[180] P. Zioupos, J. D. Currey, and A. J. Hamer. The role of collagen in the declining mechanical properties of aging human cortical bone. *J. Biomed. Mater. Res.*, 45:108–116, 1999.

List of the author's publications

Journal articles

1. Y. Chan, R. G. Haverkamp and J. M. Hill. Force-extension formula for the worm-like chain model from a variational principle. *Journal of Theoretical Biology*, 262:498-504, 2010.

2. Y. Chan, N. Thamwattana and J. M. Hill. Spiral motion of carbon atoms and C_{60} fullerenes inside single-walled carbon nanotubes. *International Journal of Theoretical and Applied Multiscale Mechanics*, 1:176-193, 2009.

3. Y. Chan, N. Thamwattana and J. M. Hill. Restricted three body problems at the nanoscale. *Few-Body Systems*, 46:1271-1291, 2009.

4. Y. Chan, G. M. Cox, R. G. Haverkamp and J. M. Hill. Mechanical model for a collagen fibril pair in extracellular matrix. *European Biophysics Journal with Biophysics Letters*, 38:487-493, 2009.

5. Y. Chan, N. Thamwattana, G. M. Cox and J. M. Hill. Mechanics of nanoscale orbiting systems. *Journal of Mathematical Chemistry*, 46:1271-1291, 2009.

6. Y. Chan, N. Thamwattana and J. M. Hill. Magnetic field driven nano tippe top. *Journal of Computational and Theoretical Nanoscience*, 6:1013-1020, 2009.

Conference papers

1. Y. Chan, G. M. Cox and J. M. Hill. A carbon atom orbiting around the outside of a carbon nanotube. *In Proceedings of International Conference on Nanoscience and Nanotechnology, 152-155 Feb 2008, ICONN 2008, Melbourne*, 2008.

Submitted manuscripts

1. Y. Chan, N. Thamwattana and J. M. Hill. Carbon nanotubes as a nonlinear buckled beam for nanoelectromechanical systems, 2009 (Submitted to *International Journal of Nanotechnology*).

2. Y. Chan, N. Thamwattana and J. M. Hill. Axial buckling of multi-walled carbon nanotubes and multi-walled nanopeapods, 2009 (Submitted to *International Journal of Solids and Structures*).

3. Y. Chan and J. M. Hill. Some novel plane trajectories for carbon atoms and fullerenes captured by two fixed parallel carbon nanotubes, 2010 (Submitted to *European Physical Journal D*)

Manuscript in preparation

1. Y. Chan and J. M. Hill. Benzene in metal-organic frameworks as molecular gyroscope and turnstile, 2010.